SIMULATION OF ULTRASOUND IMAGES OF BIOLOGICAL TISSUES

A DISSERTATION

Submitted in partial fulfillment of the requirements for the award of the degree of

MASTER OF TECHNOLOGY

in

ELECTRICAL ENGINEERING

(With Specialization in Measurement & Instrumentation)

By

TARUN JAIN

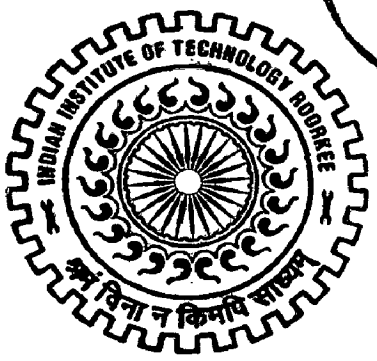

DEPARTMENT OF ELECTRICAL ENGINEERING
INDIAN INSTITUTE OF TECHNOLOGY ROORKEE
ROORKEE-247 667 (INDIA)

JUNE, 2006

ID No: MT-356/2006/51/TJ-RSA

INDIAN INSTITUTE OF TECHNOLOGY ROORKEE-247667

CANDIDATE'S DECLARATION

I hereby declare that the work, which is being presented in this dissertation entitled **"Simulation of Ultrasound Images of Biological Tissues"** in the partial fulfillment of the requirement for the award of the degree of **Master of Technology in Electrical Engineering** with specialization in **Measurement and Instrumentation,** submitted in the **Department of Electrical Engineering, Indian Institute of Technology Roorkee,** Roorkee, is an authentic record of my own work carried out during July 2005 to June 2006 under the supervision of **Dr. R.S.Anand,** Associate Professor, Department of Electrical Engineering, Indian Institute of Technology Roorkee, Roorkee.

I have not submitted the matter embodied in this dissertation for award of any other degree.

Date: 30th June 2006 **(TARUN JAIN)**

Place: Roorkee

CERTIFICATE

This is to certify that the above statement made by the candidate is true to the best of my knowledge.

Dr.R.S.Anand
Associate Professor,
Department of Electrical Engineering,
Indian Institute of Technology
Roorkee,
Roorkee – 247667.
India

Date: 30th June' 2006

Place: Roorkee

ACKNOWLEDGEMENTS

I express my foremost and deepest gratitude to **Dr.R.S.Anand**, Associate Professor, Department of Electrical Engineering, Indian Institute of Technology Roorkee, for his valuable guidance, support and motivation throughout this work. The valuable hours of discussion and suggestions that I had with him have undoubtedly helped in supplementing my thoughts in the right direction for attaining the desired objective. I consider myself extremely fortunate for having got the opportunity to learn and work under his able supervision over the entire period of my association with him.

My sincere thanks to all faculty members for their constant encouragement, caring words, constructive criticism and suggestions towards the successful completion of this work.

I do acknowledge with immense gratitude the timely help and support, which I received from my classmates and the Research Scholars in the "Biomedical Instrumentation Laboratory". I am also thankful to the staff of this Lab for their kind cooperation.

Last but not least, I'm highly indebted to my parents and friends, whose sincere prayers, best wishes, moral support and encouragement have a constant source of assurance, guidance, strength, and inspiration to me.

(TARUN JAIN)

ABSTRACT

The simulation of ultrasound imaging using linear acoustics has been extensively used for studying focusing, image formation, and flow estimation, and it has become a standard tool in ultrasound research. It is possible to simulate the whole imaging process with time varying focusing and apodization. This has paved the way for doing realistic simulated imaging with multiple focal zones for transmission and reception and for using dynamic apodization. It is hereby possible to simulate ultrasound imaging for all image types including flow images, and the purpose of this dissertation work is to present some standard simulation phantoms that can be used in designing and evaluating ultrasound transducers, beamformers and systems.

Artificial human phantoms of a fetus in the third month of development and an artificial kidney are shown. The simulation of flow and the associated phantoms is also discussed. All the phantoms can be used with any arbitrary transducer configuration like single element, linear, convex, or phased array transducers, with any apodization and focusing scheme. A fast program for the simulation of ultrasound imaging has been made. It can realistically simulate all kinds of ultrasound systems including color flow mapping.

Contents

LIST OF FIGURES

CHAPTER-1

INRODUCTION

I see... (an) important application of vision by ultrasound in medical diagnostics where it could not only replace X rays, but score above them by making visible fetuses, clogged veins and arteries, and incipient tumors. **Dennis Gabor, 1970**

1.1 What is Ultrasonics?

Ultrasound is a sound wave having frequency greater than 20 kHz which is the upper limit for human audible range. The potential of ultrasound as an imaging modality was realized in the late 1940s. From early 1970s, it established itself as a useful diagnostic tool when gray-scale ultrasound was introduced. Now it is one of the most utilized diagnostic modality in medicine. The development of the medical ultrasound imaging techniques is described in many literatures.

The diagnostic use of ultrasound in medicine is also based on the pulse-echo technique, much like sonar. A high-frequency sound pulse is directed into the body, and its reflections from boundaries or interfaces between organs and other structures and lesions in the body are then detected. By using this technique, tumours and other abnormal growths, or pockets of fluid, can be distinguished, the action of heart valves and the development of a foetus can be examined, and information about various organs of the body, such as the brain, heart, liver and kidneys, can be obtained. Although ultrasound does not replace X-rays, for certain kinds of diagnosis it is more helpful. Some kinds of tissue or fluid are not detected in X-ray photographs, but ultrasound waves are reflected from their boundaries

1.2 Ultrasound Imaging

Ultrasound is used with great success in the diagnosis of abnormalities in soft tissue structures in the human body. A pulse is emitted into the body and is scattered and reflected by density and propagation velocity perturbations. Cross-sectional pictures are made in real

time with the B-mode scan technique by current scanners. A high picture quality is obtained by employing linear and phased array transducers, and by post-processing the envelope detected signal from the transducer. But the ultrasound pictures still lack contrast and resolution compared to X-ray and NMR (nuclear magnetic resonance) pictures. It does not seem possible to cure this deficiency with the current techniques based on analog electronics, and it therefore seems plausible that future scanners will use high-frequency sampling of the transducer signal in order to employ digital signal processing. Developing algorithms that take advantage of this sampling necessitates quantitative knowledge of the received pulse-echo pressure field. The object of this dissertation work is to simulate such a model for the received pressure field.

The received field can be found by solving an appropriate wave equation. No restrictions are enforced on the transducer geometry or its excitation, and analytic expressions for a number of geometries can be incorporated into the model. The B-mode images can be generated by specifying a number of independent scatterers in a file that defines their position and amplitude. Adjusting the number of scatterers and their relative amplitude yields the proper image. Transducer designs can be optimized, to generate realistic simulated ultrasound images.

One of the first steps in designing an ultrasound system is selecting the appropriate number of elements for the array transducers and the number of channels for the beamformer. The focusing strategy in terms of number of focal zones and apodization must also be determined. These choices are often not easy, since it is difficult to determine the effect in the resulting images. It would therefore be beneficial to have programs that can quantify the image quality. So there is need to make simulation programs that can calculate the ultrasound fields and the point spread function for the imaging system.

The anatomic phantoms are attempts to generate images as they will be seen from real human subjects. The B-mode images are generated by specifying a number of independent scatterers in a file that defines their position and amplitude. Adjusting the number of scatterers and their relative amplitude yields the proper image. This is done by drawing a

bitmap image of scattering strength of the region of interest. This map then determines the factor multiplied onto the scattering amplitude generated from the Gaussian distribution, and models the difference in the density and speed of sound perturbations in the tissue. A single RF line in an image can be calculated by summing the response from a collection of scatterers. Homogeneous tissue can thus be made from a collection of randomly placed scatterers with a scattering strength with a Gaussian distribution. The phantoms typically consist of 100,000 or more scatterers, and simulating 50 to 128 RF lines can take several hours depending on the computer used. It is therefore beneficial to split the simulation into concurrently run sessions. This can easily be done by first generating the scatterer's position and amplitude and then storing them in a file.

1.3 Literature Review

This dissertation work presents a new fast simulation method based on the Field II program. Field II program runs entirely under the Matlab program [33]. It consist of a Mex file for performing the operations and a set of M-files for calling the different parts of the program. Hereby it is possible to simulate ultrasound systems with advanced dynamic focusing and apodization, *e.g.* phased and linear array imaging and flow imaging. The program has advanced features for dynamic focusing and apodization. The program is fairly new (developed in 2002), and new features are continuously added. It can currently handle round piston, concave, linear and phased arrays, and two-dimensional arrays.

The Field program system uses the concept of spatial impulse responses as developed by Tupholme and Stepanishen in a series of papers [26, 27, 29]. The approach relies on linear systems theory to find the ultrasound field for both the pulsed and continuous wave case. This is done through the spatial impulse response. This response gives the emitted ultrasound field at a specific point in space as function of time, when the transducer is excited by a Dirac delta function. The field for any kind of excitation can then be found by just convolving the spatial impulse response with the excitation function. The impulse response will vary as a function of position relative to the transducer, hence the name spatial impulse response.

The received response from a small oscillating sphere can be found by acoustic reciprocity. The spatial impulse response equals the received response for a spherical wave emitted by a point. The total received response in pulse-echo can, thus, be found by convolving the transducer excitation function with the spatial impulse response of the emitting aperture, with the spatial impulse response of the receiving aperture.

The received signal can be found by solving an appropriate wave equation. This has been done in a number of papers (e.g. [22], [23]). Gore and Leeman [22] considered a wave equation where the scattering term was a function of the adiabatic compressibility and the density. The transducer was modeled by axial and lateral pulses that were separable. Fatemi and Kak [23] used a wave equation where scattering originated only from velocity fluctuations. The scattering term for the wave equation used here is a function of density and propagation velocity perturbations, and the wave equation is equivalent to the one used by Gore and Leeman [22]. No restrictions are enforced on the transducer geometry or its excitation, and analytic expressions for a number of geometries can be incorporated into the model.

In imaging, the spatial impulse response is calculated for each of the image lines, and making 128 lines, thus, gives 128 calculations of the same impulse response delayed differently for the different lines. Doing the focusing after this point in the simulation can make the calculation faster. This corresponds to full synthetic aperture imaging. The received response from each element is calculated, when emitting with each of the elements in the aperture, and then the responses are subsequently focused. The program simulates the signals received by all 128 transducer elements, and a matrix with signals results for each pulse-echo simulation. The separation of the received signal from each of the virtual sources is done by applying a matched filter for each band on all the received signals. The result is the received signal on a specific element for one of the bands. The matched filter also equalizes the phase of the signals, so they all become zero phase signals. The signals are then focused by adding them for all elements, all bands and both emissions with a compensation for the travel time from the virtual source to the receiving element. The flow is simulated for a random collection of point scatterers in a tube with a laminar,

parabolic flow. This is the approach taken in this dissertation work using a modified version of the Field II program.

1.4. Organization of Thesis

This Thesis is organized in the following way:

In Chapter-2, Ultrasound physics is discussed. Wave propagation, Beam formation, Point Spread Function and the Scattering properties of Ultrasound waves is explained.

Chapter-3 gives a linear description of acoustic fields using spatial impulse responses. It is shown how both the pulsed emitted and scattered fields can be accurately derived using spatial impulse responses. The chapter goes into some detail of deriving the different results and explaining their consequence. Different examples for both simulated and measured fields are given.

Chapter-4 chapter gives a short introduction to modern ultrasound imaging using array transducers. Received response for different kinds of transducers geometry is simulated using Field II software.

In Chapter-5 simulation of ultrasound images of body tissues is presented. Two different phantoms have been made; a *fetus* in the third month of development and a left *kidney* in a longitudinal scan.

Chapter 6 gives a brief description of the main features of flow imaging. The chapter starts by deriving a basic model for ultrasound's interaction with a point scatterer, which shows that the frequency of the received sampled signal is proportional to velocity. Systems for finding the velocity distribution in a vessel are then described and finally a phantom is developed for evaluating color flow.

Finally in Chapter7 conclusions and scope for future work are given.

CHAPTER-2

PHYSICAL FOUNDATIONS

2.1. Wave Propagation

Ultrasound waves are mechanical waves i.e. acoustic energy is transferred between two points in the medium while leaving the intervening medium essentially unchanged after transfer. Mechanical waves are of two fundamental types:

Longitudinal: the oscillating particles of the medium are displaced parallel to the direction of motion (direction of energy transfer).

Transverse: the oscillating particles of the medium are displaced in a direction perpendicular to the motion of the wave.

When the elasticity of the medium causes neighboring particles to display a similar oscillation, a wave is set up, and the oscillation appears to move through the medium with some velocity of propagation. A single oscillation may set up a pulse or a series of oscillations can set up a wave train.

The most general form for a one-dimensional wave, without dispersion, is given by the superposition of two rigid waveforms moving in opposite directions i.e.

$$u(x,t) = f_{+}(x-ct) + f_{-}(x+ct), \tag{2.1}$$

It can be shown that any general function u(x, t) satisfies (in one-dimension) the wave equation

$$\frac{\partial^2 u}{\partial^2 x} = \frac{1}{c^2}\frac{\partial^2 u}{\partial t^2}, \tag{2.2}$$

where u is the particle displacement amplitude, x *is* the position in space along the direction of propagation, t is the time and c is the propagation speed. Such an equation applies generally to all forms of wave motion.

The speed is related to the elasticity K and the density ρ of the medium in which the wave is traveling, according to the equation:

$$c = \left(K/\rho\right)^{1/2}. \tag{2.3}$$

At a plane boundary between two media with speeds $c1$ and $c2$ respectively,

$$\theta_i = \theta_t \tag{2.4}$$

$$\left(\sin\theta_i / \sin\theta_t\right) = c1/c2 \tag{2.5}$$

where θi, θr and θt are respectively the angles of incidence, reflection and refraction. At normal incidence,

$$I_r/I_i = \left[(Z_2 - Z_1)/(Z_2 + Z_1)\right]^2, \tag{2.6}$$

where Ii and Ir are respectively the intensities of the incident and reflected waves and Z_1 and Z_2 are the characteristic impedances of the two media. The characteristic impedance of a medium is given by:

$$Z = \partial c \tag{2.7}$$

The situation to which equation (2.7) applies is called specular reflection (refer section 2.4) and it implies that the reflecting boundary is both smooth and extensive in relation to the wavelength λ. By defining a quantity related to the size of an obstacle, two situations can be distinguished, each with a corresponding value of scattering cross section S

$$S = 1 \qquad \text{when} \quad \psi << \lambda \tag{2.8}$$

$$S = k^4 \psi^6 \qquad \text{when} \quad \psi << \lambda \tag{2.9}$$

where $k=2\pi f$, frequency f =c/λ and ψ is radius of the scatterer. Thus, specular reflection is described by equation (2.8) and Rayleigh scattering, by equation (2.9).With obstacles of intermediate size (or with rough surfaces), directional scattering occurs.

2.2 The Ultrasound Transducer

A transducer is a device capable of changing one form of energy into another. For ultrasound purposes, the transducer is the sender and a receiver of ultrasonic pulses and echoes. This transducer can change electrical impulses into mechanical waves and vice versa. As a transmitter, the transducer employs a piezoelectric crystal to create the ultrasound waves by applying electrical pulse to it; these waves are then direct towards body tissues. As the receiver, the transducer receives the reflected waves from the tissues interface and converts it into electrical signal. At the receiver various functions are also performed including amplification, compensation, demodulation, compression and rejection.

2.2.1 Piezoelectric Effect

Man-made lead zirconate and lead titanate are used as crystals within most modern ultrasound transducers. These crystals are referred to as the piezoelectric (pressure-electric) crystals because they have the properties necessary for conversion of electrical stimulus to vibrations which produce pressure (sound) waves and vice versa. This unique quality enables transmission and receipt of the ultrasound signal by a single transducer.

2.2.2 Pulse Principles

Electricity is applied to the piezoelectric crystals at a specific pulse rate. This allows for transmission of the wave as well as listening for echoes. Generally, the transducer sends pulses of 1 microsecond duration with a repetition period of 999 micro seconds. Therefore, most of the time, the ultrasound scanhead is in "listening" mode. Pulse rate may also be controlled by the rate of oscillation of a mechanical scan head.

2.2.3 Transducer Selection

The correct transducer must be chosen from a wide range of possibilities. Variables specific to each transducer must be carefully examined so as to choose the optimal transducer for the particular task at hand. Variables include frequency, image shape and inherent technology.

2.2.4 Frequency

Most manufacturers offer a variety of transducers with frequencies ranging from 2-10 MHz. Some even possess the ability to vary the frequency within a single transducer. The operating frequency of a transducer is generally determined by the size of the piezoelectric crystals employed within.

As a rule, lower frequencies allow better penetration than those at upper frequencies. For this increase in penetration, there is a decrease in resolution, however. Lower frequency (2-3.5 MHz) should be used for third trimester examinations, and when you need additional penetration ability (as for obese patients). A 3.5 MHz transducer is standard equipment on most commercially available ultrasound systems. Medium frequency transducers (5.0 MHz) are the best compromise between penetration and resolution. They can be used for all GYN and OB scans of patients with normal habitus. High frequency transducers have greater ability to resolve minute structures, but the user is limited by decreased depth of penetration. High frequency transducers (7.5-10 MHz) are employed for examination of small parts such as thyroid, breast and testicles. This may also be quite useful during the examination/localization of a superficial ovary, or for a very thin patient.

2.3. Beam formation, Resolution and the Point Spread Function

The aperture of the ultrasonic transducer used in medical imaging is usually in the form of a circle or a rectangle. As illustrated in figure 2.1, the ultrasonic beam can be considered to consist of a near field and a far field.

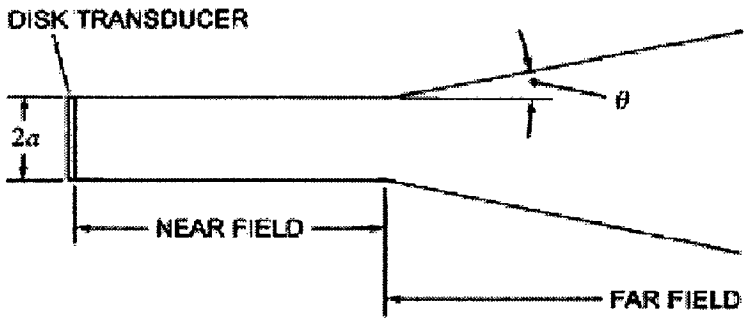

Fig. 2.1: A Simple representation of ultrasonic beam produced by a disc transducer in a homogeneous medium.

With continuous wave excitation of a disc transducer,

$$I_z/I_0 = \sin^2\left\{(\pi/\lambda)\left[(a^2+z^2)^{1/2}-z^2\right]\right\}, \tag{2.10}$$

where I_0 is the intensity at the surface of the transducer, Iz is the intensity at a distance z from the transducer along the central axis of the beam and a is the radius of the transducer. In the far field, beyond the last axial maximum (at $z = a^2/\lambda$, provided that $a^2 >> \lambda^2$, the directivity function is

$$Ds = \frac{2J_1(ka\sin\theta)}{ka\sin\theta}, \tag{2.11}$$

where θ is the angle between Ds and the central axis of the beam and J_1 is the first-order Bessel function. In the near field, the beam is roughly cylindrical with a series of axial maxima and minima of decreasing complexity moving away from the transducer. Also, in the near field, the beam can be focused by a lens or other means. If the transducer is excited to produce a transient disturbance, the ultrasonic pulse has its energy spread over a spectrum of frequency, corresponding to its bandwidth. This means that single values cannot be assigned to λ or k in equations (2.10) and (2.11). Physically, the beam diffraction pattern is smeared to an extent which changes during the passage of the pulse.

A typical transducer uses an array of piezoelectric elements to transmit a sound pulse into the body and to receive the echoes that return from scattering structures within. This array is often referred to as the imaging system's aperture. The transmit signals passing to, and the received signals passing from the array elements can be individually delayed in time, hence the term phased array. This is done to electronically steer and focus each of a sequence of acoustic pulses through the plane or volume to be imaged in the body. This produces a 2- or 3-D map of the scattered echoes. The process of steering and focusing these acoustic pulses is known as beamforming. This process is shown schematically in Figure 2.2.

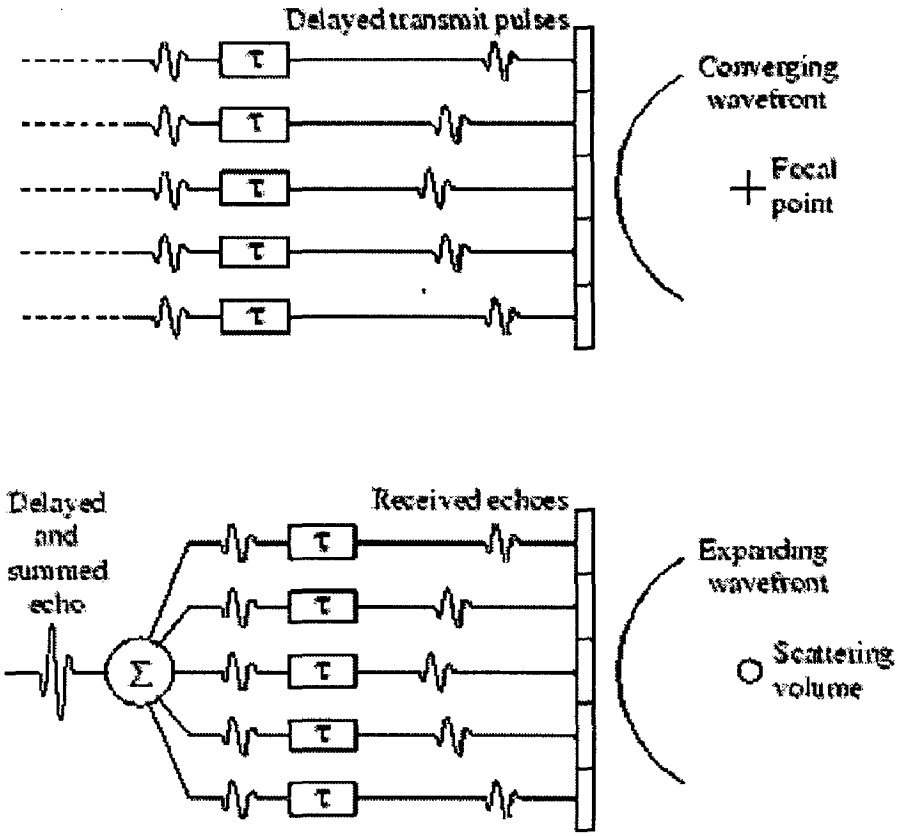

Fig. 2.2 A conceptual diagram of phased array beamforming. (Top) Appropriately delayed pulses are transmitted from an array of piezoelectric elements to achieve steering and focusing at the point of interest. (Bottom) The echoes returning are likewise delayed before they are summed together to form a strong echo signal from the region of interest.

The ability of a particular ultrasound system to discriminate closely spaced scatterers is specified by its spatial resolution, which is typically defined as the minimum scatterer spacing at which this discrimination is possible. The system resolution has three components in Cartesian space, reflecting the spatial extent of the ultrasound pulse at the focus. The coordinates of this space are in the axial, lateral, and elevation dimensions. The axial, or range, dimension indicates the predominant direction of sound propagation, extending from the transducer into the body. The axial and the lateral dimension together define the tomographic plane, or slice, of the displayed image. These dimensions relative to the face of a linear array transducer are shown in Figure 2.3. The elevation dimension contains the slice thickness.

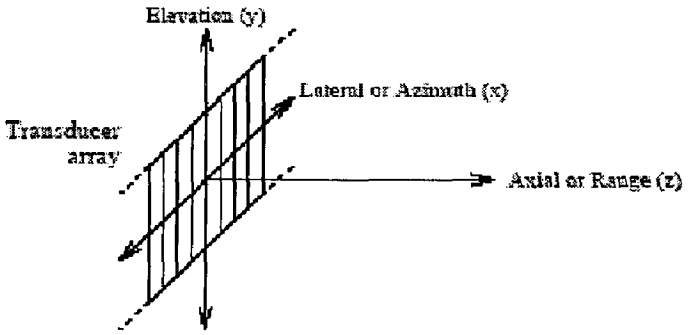

Fig. 2.3: A diagram of the spatial coordinate system used to describe the field and resolution of an ultrasound transducer array. Here the transducer is a 1-D array, subdivided into elements in the lateral dimension. The transmitted sound pulse travels out in the axial dimension.

A modern ultrasound scanner operating in brightness mode, or B-mode (refer section 4.3), presents the viewer with a gray-scale image that represents a map of echo amplitude, or brightness, as a function of position in the region being scanned (refer section 4.3). In B-mode the ultrasound system interrogates the region of interest with wide bandwidth sound pulses. Such a pulse from a typical array is shown in Figure 2.4. The acoustic pulse in Figure 2.4 is shown as a function of acoustic pressure over the lateral and axial dimensions. In fact the pulse is a three-dimensional function, with extent in elevation as well. In the terminology of linear systems theory it is the impulse response of the system, and the response of the ultrasound system at the focus is fully characterized by this function. As it represents the output of the ultrasound system during interrogation of an ideal point target, it is also known as the system's point spread function (PSF). The character of the PSF in the axial dimension is determined predominantly by the center frequency and bandwidth of the acoustic signal generated at each transducer element, while its character in the lateral and elevation dimensions is determined predominantly by the aperture and element geometries and the beamforming applied. The term PSF is often used to refer to two-dimensional representations of the system response in pressure amplitude versus space, such as that shown in Figure 2.4, with the implicit understanding that the actual response has three-dimensional extent.

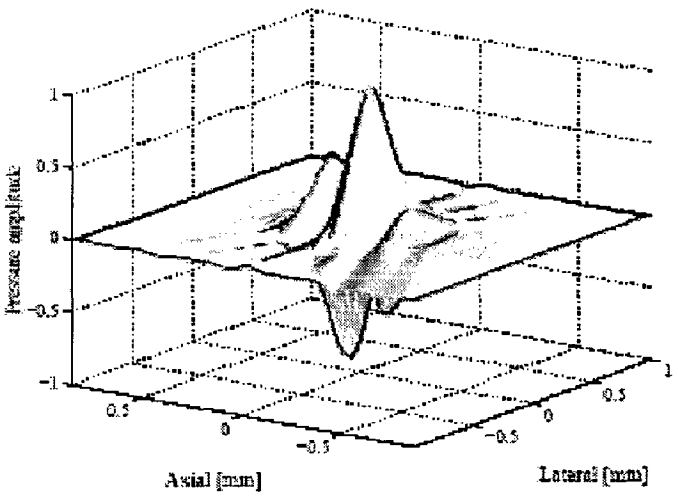

Fig. 2.4: The acoustic pulse from a typical array (7.5 MHz, 60% bandwidth, 128 elements of width equal to the wavelength), shown at the acoustic focus. The pulse is displayed as a map of pressure amplitude and is traveling in the positive direction along axial dimension.

The spatial impulse response is the hypothetical pressure pattern created upon excitation of the array with a perfect impulse. The spatial impulse response is not a physically realizable, but serves as a useful calculation tool in this context. This method can accommodate arbitrary geometries by division of the aperture into smaller, rectangular elements. The spatial impulse response for each element is calculated separately, and then these solutions are combined by superposition to produce that for the entire aperture.

The three components of spatial resolution define what is called the resolution volume. A modern, high frequency ultrasound transducer has a resolution volume at the focus that is on the order of 300 x 300 x 1000 μm axially, laterally, and in elevation, respectively. The evolution of the dimensions of the acoustic pulse from a typical array (7.5 MHz, 60% bandwidth, 128 elements of width equal to the wavelength, or λ-pitch) as it passes through the focal plane with fixed transmit and receive focus is shown in Figure 2.5. This figure plots the -6 dB amplitude contour of the PSF in a sequence of slices. Each slice defines a plane in the lateral-elevational dimensions, and the slices are spaced in the axial dimension. These contours demonstrate how the PSF is most compact at the focus, and also show the

resolution mismatch between the lateral and elevation dimensions that is typical of a 1-D array. The axial dimension of the resolution volume is not displayed in this plot.

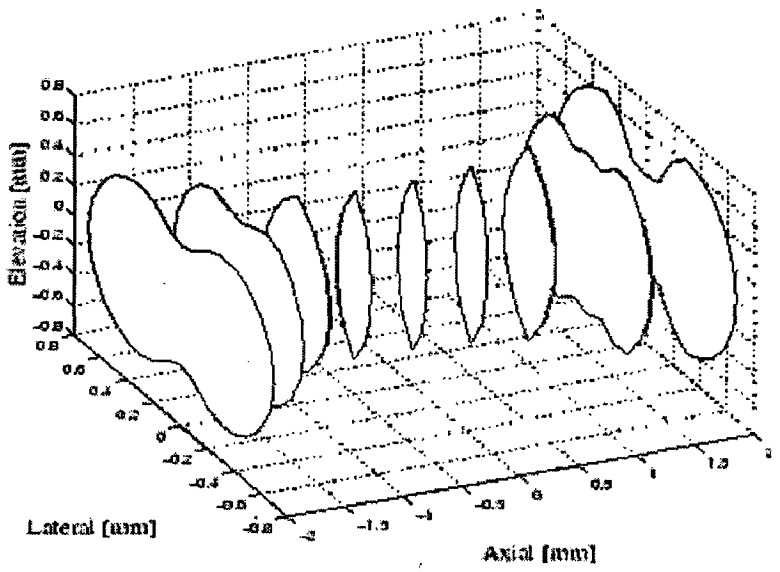

Fig. 2.5: This diagram shows how the spatial resolution of the acoustic pulse in the lateral and elevation dimensions changes as it travels in the axial dimension through the focal plane. These acoustic pressure amplitude contours are -6 dB relative to the peak amplitude within each slice of the point-spread function (PSF) as it propagates. Dimensions are relative to the focal point.

2.4. The Scattering and Reflection of Sound

Medical ultrasound imaging relies utterly on the fact that biological tissues scatter or reflect incident sound. Although the phenomenon are closely related, in this text *scattering* refers to the interaction between sound waves and particles that are much smaller than the sound's wavelength λ, while *reflection* refers to such interaction with particles or objects larger than λ.

The scattering or reflection of acoustic waves arises from inhomogeneities in the medium's density and/or compressibility. Sound is primarily scattered or reflected by a discontinuity in the medium's mechanical properties, to a degree proportional to the discontinuity. (By contrast, continuous changes in a medium's material properties cause the direction of propagation to change gradually.) The elasticity and density of a material are related to its

sound speed, and thus sound is scattered or reflected most strongly by significant discontinuities in the density and/or sound speed of the medium.

Figure 2.6 shows two types of echoes that can result in ultrasound imaging.

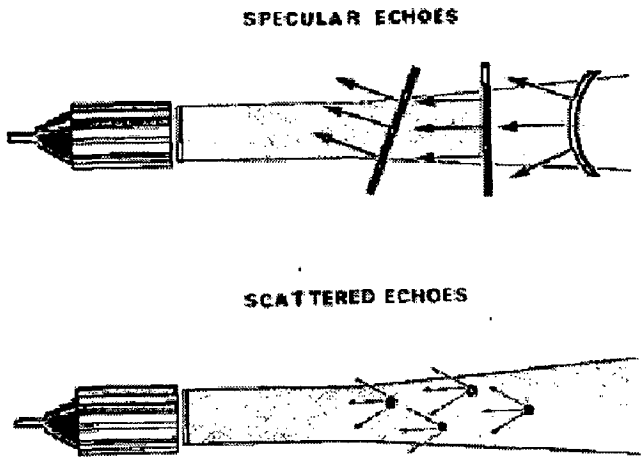

Fig. 2.6: Illustration of specular and scattered echoes

The first, specular echoes, originate from relatively large, strongly reflective, regularly shaped objects with smooth surfaces. These reflections are angle dependent, and are given by equation 2.13. These reflections are called specular reflection.

The second type of echoes are scattered that originate from small, weakly reflective, irregularly shaped objects, and are less angle-dependent and less intense. Unfortunately, the mathematical treatment of non-specular reflection (sometimes called "speckle") is a bit more complicated, and involves the Rayleigh probability density function. This type of reflection, however, sometimes dominates medical image.

2.4.1. Scatterer Sizes Less than and Equal to the Wavelength

Consider a medium subjected to acoustic insonification, and a particle in this medium that is much smaller than the wavelength of the sound. If this particle is of the same density and compressibility as the medium, it scatters no sound at all. If its density is the same but its compressibility is different, it will react to the surrounding pressure variation by radially expanding and contracting differently than the surrounding medium. This type of scatterer

gives off *monopole radiation,* shown in Figure 2.7 If these conditions are reversed, i.e. the particle's compressibility is the same as the surrounding medium but its density is different, the particle's motion in response to the incident wave will not equal that of the medium, and it will move back and forth in relation to the medium. This type of scattering gives off *dipole radiation*, also shown in Figure 2.7. Most real sub-wavelength scatterers emit some combination of monopole and dipole radiation, although one may dominate significantly over the other.

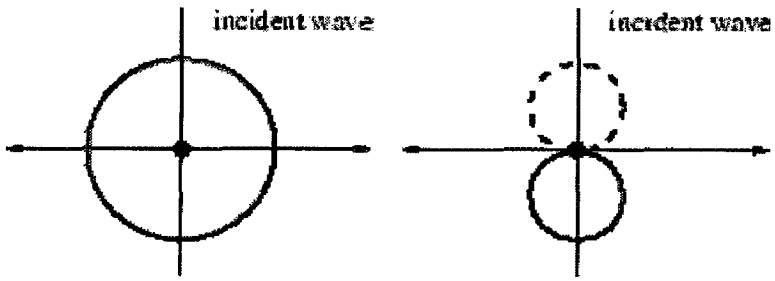

Fig. 2.7: (Left) The pressure amplitude pattern of monopole radiation from a "compressibility" scatterer is isotropic. (Right) The corresponding pattern of a "density" scatterer is highly directional, corresponding to two closely-spaced monopoles operating out of phase. The pattern exhibits a 180^0 phase shift along the axis of sound propagation, and a null surrounding the scatterer and normal to this axis.

The radiation pattern becomes more complex as the scatterer size approaches the wavelength of the incident sound. The analytic solution for the radiation pattern from a spherical elastic scatterer in a fluid was first described by Faran. The radiation pattern of such a scatterer is dependent on the material properties of the sphere and the medium and on the sphere's radius. Also, the result depends on whether one includes the effects of sound penetrating into the sphere and reverberating, which distinguishes the ``elastic" from the ``inelastic" solution. Faran solutions for radiation magnitude vs. scattering angle are shown in Figures 2.8 and 2.9 for a range of sphere radii, parameterized by the sphere radius a and the wavenumber of insonification $k = 2\pi/\lambda$, and using the material properties of crown glass (c = 5100 m/s, ρ= 2.4 gm/cm^3, σ = 0.24) in 20^0 water[9]. Faran defines the scattering angle such that the sound source is at 180^0. These figures show that as the

scatterer radius is increased up to and beyond the wavelength of the sound, the radiation pattern becomes progressively more *directional.*

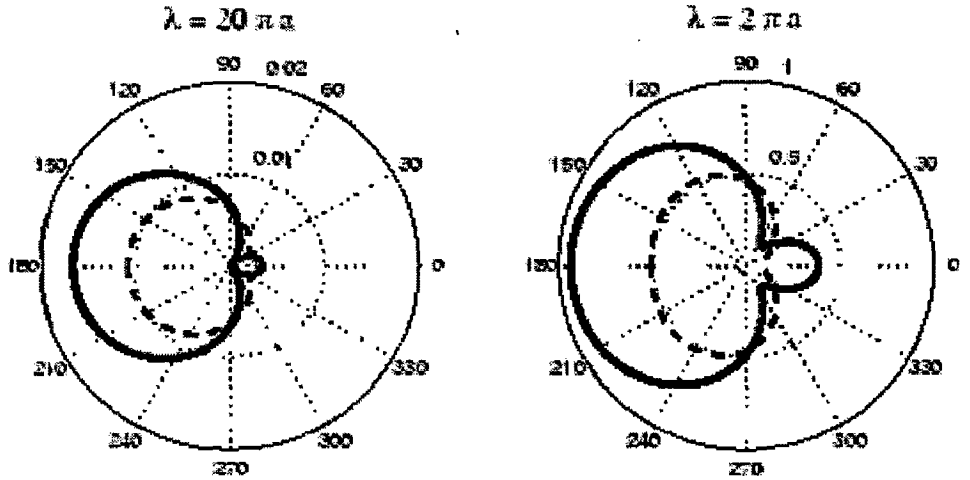

Fig. 2.8: Angular scattering from elastic (solid) and inelastic (dashed) spheres of circumference $\leq \lambda$. The insonification source is located at 180^0.

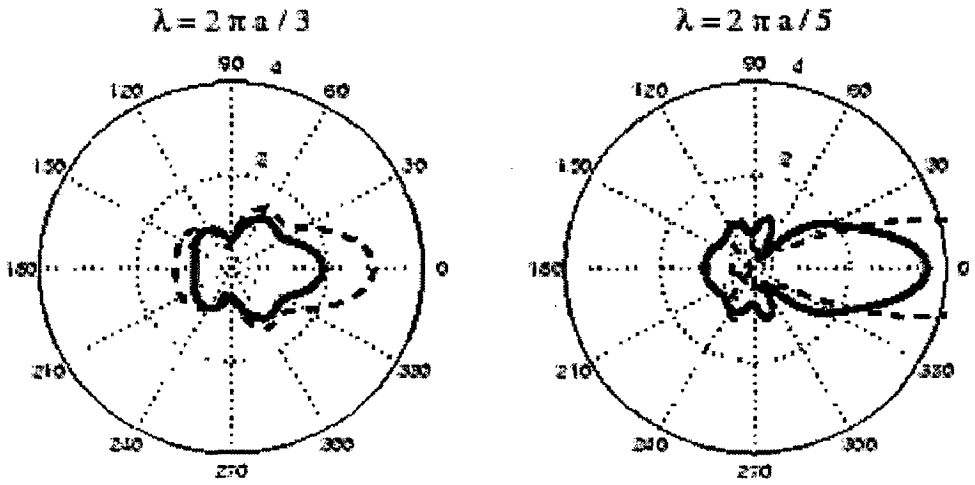

Fig. 2.9: Angular scattering from elastic (solid) and inelastic (dashed) spheres of circumference $> \lambda$. The insonification source is located at 180^0.

We can make several other observations using the Faran model. In Figure 2.10 we consider the magnitude of the sphere's echo back at the source as a function of *ka,* the product of the frequency and the sphere's radius. In the left half of the figure, we consider $ka < 1$, and observe that the echo magnitude for this condition (solid line) is roughly comparable to $(ka)^2$ (dashed line). In other words, the echo magnitude of scatterers significantly smaller

than the wavelength has a f^2 dependence. When echo magnitude $|A|$ is converted to intensity $|A|^2$, this dependence is approximately f^4. Scatterers that are much smaller than the wavelength are known as *Rayleigh scatterers*, and are generally considered to have a f^4 intensity dependence.

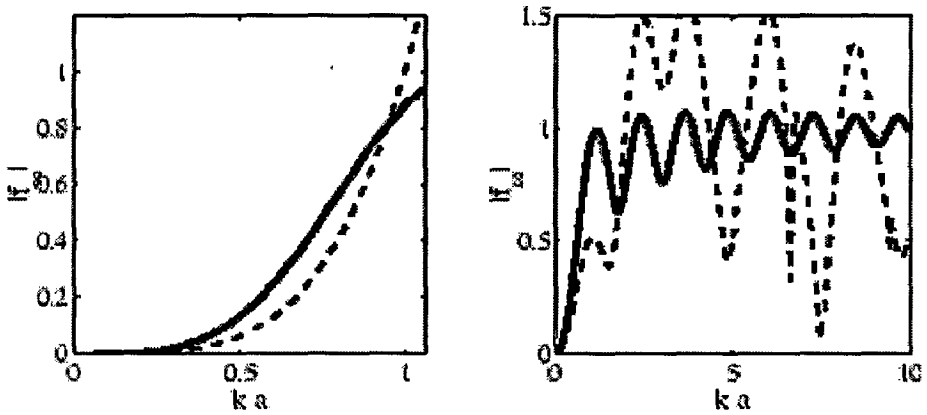

Fig. 2.10: The backscatter amplitude for a sphere as a function of frequency

In Figure 2.10 (Left) The backscatter amplitude for a sphere for ka <1 (solid) is compared to $(ka)^2$ (dashed), showing that for scatterers smaller than the wavelength, echo amplitude as a f^2 dependence, corresponding to an intensity dependence of f^4, a characteristic of Rayleigh scattering. (Right) The backscatter amplitude for a sphere as a function of frequency is compared for the elastic (dashed) and inelastic (solid) cases, showing how internal reverberation of sound within a scatterer can create peaks and nulls in the scattering spectrum

Also shown in Figure 2.10 is a graph of the backscatter echo magnitude (i.e. scattering angle = $180^{0)}$ for 0 < ka < 10. The elastic (solid) and the inelastic (dashed) solutions are contrasted. For a fixed diameter a, this Faran solution corresponds to a scatterer ``frequency response". It is seen that when the solution includes the effects of sound penetrating into the sphere and reverberation within the sphere, this spectrum develops complex nulls and peaks. Thus reverberation of sound within a scatterer results in a echo response that can be highly frequency dependent, and markedly different from the response predicted without accounting for these effects. One the other hand, the inelastic response is adequate for materials with density and/or sound speed *much* greater than those of the surrounding fluid.

2.4.2. Reflecting Structures Larger than the Wavelength

Tissue structures within the body feature boundaries on a scale much larger than the wavelength. Prominent *specular* echoes arise from these boundaries. The acoustic properties of tissues are often characterized using the concept of *acoustic impedance* Z.

$Z = \rho_0 c = \sqrt{\rho_0} c_{elas}$, where ρ_0 is the density of the tissue, c is the sound speed, and c_{elas} is the tissue elasticity. When a wave is directly incident on a boundary between two media with acoustic impedances Z_1 and Z_2, the ratio of incident to reflected pressure is predicted by the reflection coefficient R, defined as:

$$R = \frac{Z_2 - Z_1}{Z_2 + Z_1} \tag{2.12}$$

It is important to note that in ultrasound, as in optics, tissue boundaries can also give rise to refraction that can produce image artifacts, steering errors, and aberration of the beam. A more general form of Equation (2.11) describes reflection and refraction as a function of incident angle, where the incident and transmitted angles θ_i and θ_t, shown in Figure 2.10, are related by Snell's Law:

$$R = \frac{(Z_2 / \cos\theta_t) - (z_1 / \cos\theta_i)}{(Z_2 / \cos\theta_t) + (z_1 / \cos\theta_i)}$$
$$where, \frac{\sin\theta}{\sin\theta_t} = \frac{\lambda_1}{\lambda_2} = \frac{c_1}{c_2} \tag{2.13}$$

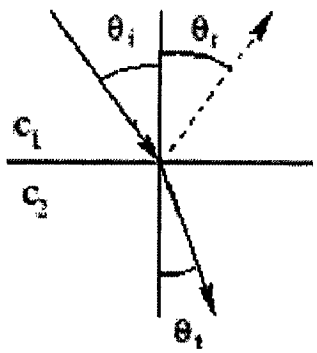

Fig. 2.11: The geometry of reflection and refraction at a boundary between media with different sound speeds.

2.5. The Doppler Effect

When an ultrasonic wave is scattered by a target that has a component of velocity along the direction of beam propagation, the frequency of the scattered ultrasound is shifted by the Doppler effect. If θ is the angle between the direction of target motion and that of the ultrasonic beam,

$$v = -f_D c / (2f \cos\theta), \tag{2.14}$$

where v is the speed of the target and f_D is the difference between the frequencies of the ultrasound transmitted from the transducer and backscattered along the ultrasonic beam, provided that $v << c$. The negative sign means that the frequency is shifted downwards if the target is moving away from the transducer.

CHAPTER-3

DESCRIPTION OF ULTRASOUND FIELDS

This chapter gives a linear description of acoustic fields using spatial impulse responses. It is shown how both the pulsed emitted and scattered fields can be accurately derived using spatial impulse responses. The chapter goes into some detail of deriving the different results and explaining their consequence. Different examples for both simulated and measured fields are given. The chapter is based on the papers [1], [2] and [3] and on the book [4].

3.1 Fields in Linear Acoustic Systems

It is a well known fact in electrical engineering that a linear electrical system is fully characterized by its impulse response as shown in Fig. 3.1. Applying a delta function to the input of the circuit and measuring its output characterizes the system. The output $y(t)$ to any kind of input signal $x(t)$ is then given by

$$y(t) = h(t) * x(t) = \int_{-\infty}^{+\infty} h(\theta)x(t-\theta)d\theta \tag{3.1}$$

where $h(t)$ is the impulse response of the linear system and * denotes time convolution. The transfer function of the system is given by the Fourier transform of the impulse response and characterizes the systems amplification of a time-harmonic input signal.

The same approach can be taken to characterize a linear acoustic system. The basic set-up is shown in Fig. 3.2. The acoustic radiator (transducer) on the left is mounted in a infinite rigid, baffle and its position is denoted by $\vec{r}_2$ It radiates into a homogeneous medium with a constant speed of sound c and density ρ_0 throughout the medium. The point denoted by $\vec{r}_1$ is where the acoustic pressure from the transducer is measured by a small point hydrophone. A voltage excitation of the transducer with a delta function will give rise to a pressure field that is measured by the hydrophone. The measured response is the acoustic impulse response for this particular system with the given set-up. Moving the transducer or

the hydrophone to a new position will give a different response. Moving the hydrophone closer to the transducer surface will often increase the signal, and moving it away from the center axis of the transducer will often diminish it. Thus, the impulse response depends on the relative position of both the transmitter and receiver ($\vec{r}_2 - \vec{r}_1$) and hence it is called a spatial impulse response.

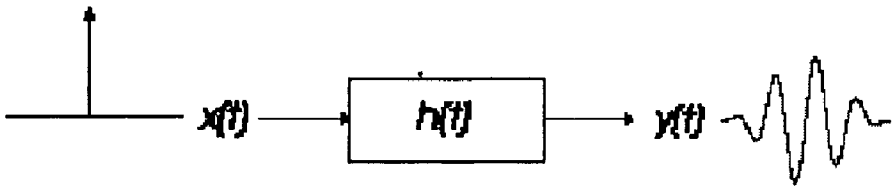

Fig. 3.1: Measurement of impulse response for a linear electric system.

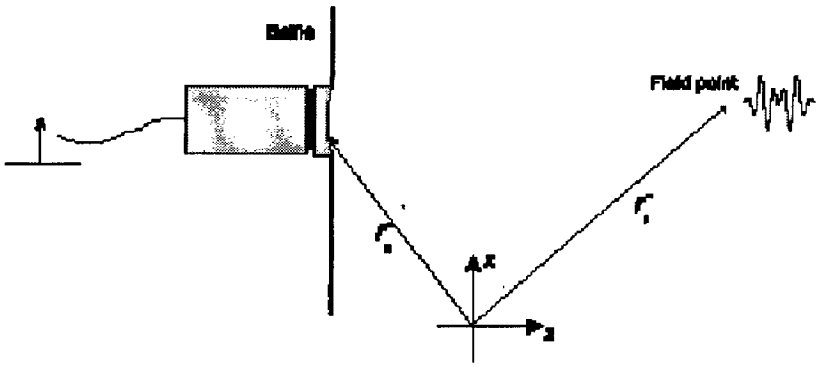

Fig. 3.2: A linear acoustic system.

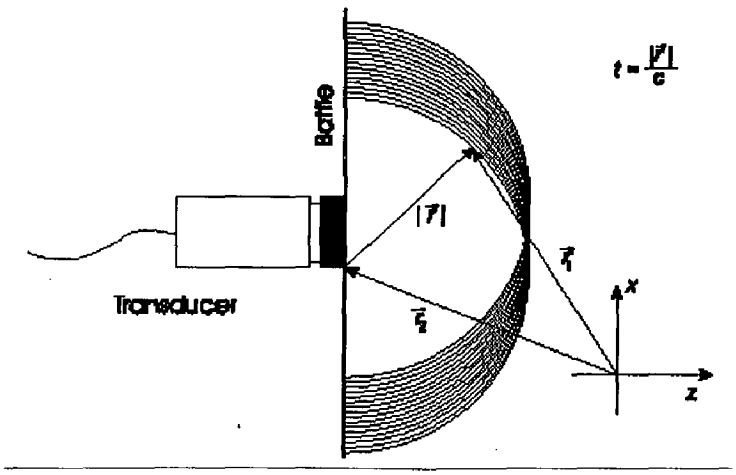

Fig. 3.3: Illustration of Huygens' Principle for a fixed time instance. A spherical wave with a radius of $|\vec{r}| = ct$ is radiated from each point on the aperture.

A perception of the sound field for a fixed time instance can be obtained by employing Huygen's Principle in which every point on the radiating surface is the origin of an outgoing spherical wave. This is illustrated in Fig. 3.3. Each of the outgoing spherical waves are given by:

$$p_s(\vec{r}_1, t) = \delta\left(t - \frac{|\vec{r}_2 - \vec{r}_1|}{c}\right) = \delta\left(t - \frac{|\vec{r}|}{c}\right) \tag{3.2}$$

where $\vec{r}_1$ indicates the point in space, $\vec{r}_2$ is the point on the transducer surface, and t is the time for the snapshot of the spatial distribution of the pressure. The spatial impulse response is then found by observing the pressure waves at a fixed position in space over time by having all the spherical waves pass the point of observation and summing them. Being on the acoustical axis of the transducer gives a short response whereas an off-axis point yields a longer impulse response as shown in Fig. 3.3.

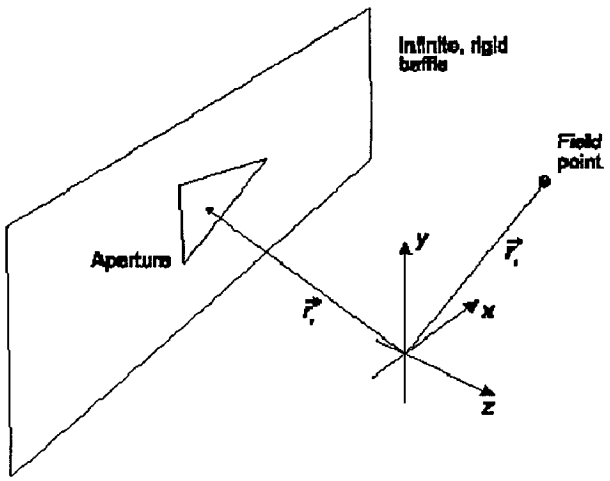

Fig 3.4: Position of transducer, field point, and coordinate system.

3.2 Basic Theory

In this section the exact expression for the spatial impulse response will more formally be derived. The basic setup is shown in Fig. 3.4. The triangularly shaped aperture is placed in an infinite, rigid baffle on which the velocity normal to the plane is zero, except at the aperture. The field point is denoted by $\vec{r}_1$ and the aperture by $\vec{r}_2$. The pressure field generated by the aperture is then found by the Rayleigh integral **[5]**

$$p(\vec{r}_1,t)=\frac{\rho_o}{2\pi}\frac{\int_S \partial v_n(\vec{r}_2,t-\frac{|\vec{r}_1-\vec{r}_2|}{c})}{\frac{\partial t}{|\vec{r}_1-\vec{r}_2|}}dS, \tag{3.3}$$

where V_n is the velocity normal to the transducer surface. The integral is a statement of Huygens' Principle that the field is found by integrating the contributions from all the infinitesimally small area elements that make up the aperture. This integral formulation assumes linearity and propagation in a homogeneous medium without attenuation. Further, the radiating aperture is assumed flat, so no re-radiation from scattering and reflection takes place. Exchanging the integration and the partial derivative, the integral can be written as

$$p(\vec{r}_1,t)=\frac{\rho_o}{2\pi}\frac{\partial\int_S \frac{v_n(\vec{r}_2,t-\frac{|\vec{r}_1-\vec{r}_2|}{c})}{|\vec{r}_1-\vec{r}_2|}dS}{\partial t}\ , \tag{3.4}$$

It is convenient to introduce the velocity potential ψ. that satisfies the equations [6]

$$\vec{v}(\vec{r},t)=-\nabla\Psi(\vec{r},t)$$

$$\vec{p}(\vec{r},t)=\rho_0\frac{\partial\Psi(\vec{r},t)}{\partial t}. \tag{3.5}$$

Then only a scalar quantity needs to be calculated and all field quantities can be derived from it. The surface integral is then equal to the velocity potential:

$$\Psi(\vec{r}_1,t)=\frac{\int_S v_n(\vec{r}_2,t-\frac{|\vec{r}_1-\vec{r}_2|}{c})}{2\pi|\vec{r}_1-\vec{r}_2|}dS \tag{3.6}$$

The excitation pulse can be separated from the transducer geometry by introducing a time convolution with a delta function as

$$\Psi(\vec{r}_1,t)=\int_S\int_T\frac{v_n(\vec{r}_2,t_2)\delta\left(t-t_2-\frac{|\vec{r}_1-\vec{r}_2|}{c}\right)}{2\pi|\vec{r}_1-\vec{r}_2|}dt_2dS, \tag{3.7}$$

where δ is the Dirac delta function.

Assume now that the surface velocity is uniform over the aperture making it independent of $\vec{r}_2$, then

$$\Psi(\vec{r}_1,t)=v_n(t)*\int_S\frac{\delta(t-\frac{|\vec{r}_1-\vec{r}_2|}{c})}{2\pi|\vec{r}_1-\vec{r}_2|}dS \tag{3.8}$$

where * denotes convolution in time. The integral in this equation

$$h(\vec{r}_1,t)=\int_S \frac{\delta(t-\frac{|\vec{r}_1-\vec{r}_2|}{c})}{2\pi|\vec{r}_1-\vec{r}_2|}dS \tag{3.9}$$

is called the spatial impulse response and characterizes the three-dimensional extent of the field for a particular transducer geometry. Note that this is a function of the relative position between the aperture and the field.

Using the spatial impulse response the pressure is written as

$$p(\vec{r}_1,t)=\rho_0\frac{\partial v_n(t)}{\partial t}*h(\vec{r}_1,t) \tag{3.10}$$

which equals the emitted pulsed pressure for any kind of surface vibration $V_n(t)$. The continuous wave field can be found from the Fourier transform of (3.10). The received response for a collection of scatterers can also be found from the spatial impulse response [7], [1]. This is derived in Section 3.6. Thus, the calculation of the spatial impulse response makes it possible to find all ultrasound fields of interest.

3.2.1 Geometric Considerations

The calculation of the spatial impulse response assumes linearity and any complex-shaped transducer can therefore be divided into smaller apertures and the response can be found by adding the responses from the sub-apertures. The integral is, as mentioned before, a statement of Huygens' principle of summing contributions from all areas of the aperture.

An alternative interpretation is found by using the acoustic reciprocity theorem [8]. This states that: "If in an unchanging environment the locations of a small source and a small receiver are interchanged, the received signal will remain the same." Thus, the source and receiver can be interchanged. Emitting a spherical wave from the field point and finding the wave's intersection with the aperture also yields the spatial impulse response. The situation is depicted in Fig. 3.5, where an outgoing spherical wave is emitted from the origin of the

coordinate system. The dashed curves indicate the circles from the projected spherical wave.

The calculation of the impulse response is then facilitated by projecting the field point onto the plane of the aperture. The task is thereby reduced to a two-dimensional problem and the field point is given as a (x,y) coordinate set and a height z above the plane. The three-dimensional spherical waves are then reduced to circles in the x / y plane with the origin at the position of the projected field point as shown in Fig. 3.6.

The spatial impulse response is, thus, determined by the relative length of the part of the arc that intersects the aperture. Thereby it is the crossing of the projected spherical waves with the edges of the aperture that determines the spatial impulse responses. This fact is used for deriving equations for the spatial impulse responses in the next section.

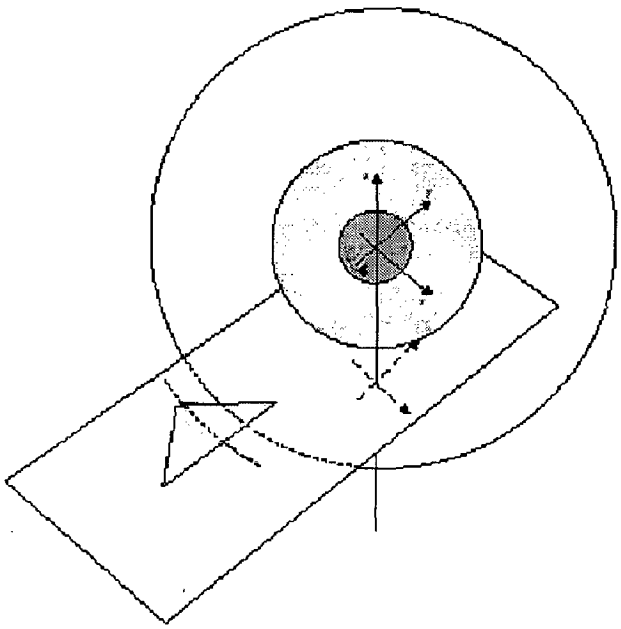

Fig. 3.5: Emission of a spherical wave from the field point and its intersection of the aperture.

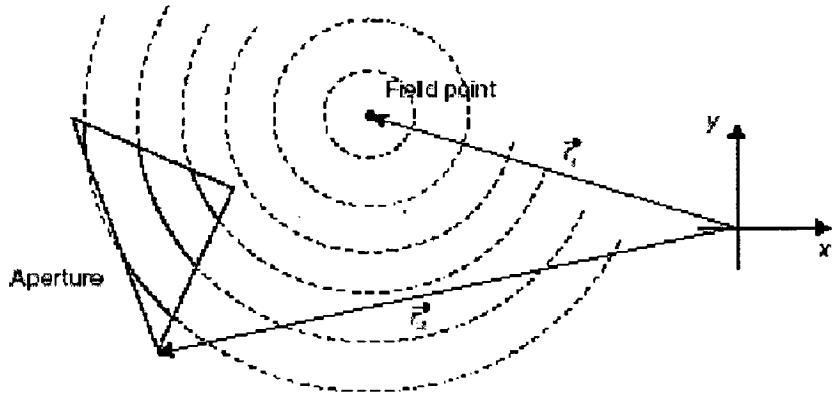

Fig. 3.6: Intersection of spherical waves from the field point by the aperture, when the field point is projected onto the plane of the aperture.

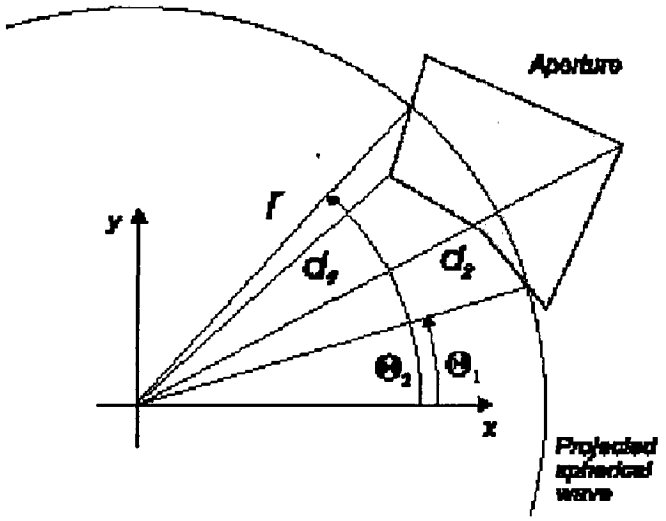

Fig. 3.7: Definition of distances and angles in the aperture plan for evaluating the Rayleigh integral.

3.3 Calculation of Spatial Impulse Responses

The spatial impulse response is found from the Rayleigh integral derived earlier

$$h(\vec{r}_1,t) = \int_S \frac{\delta(t - \frac{|\vec{r}_1 - \vec{r}_2|}{c})}{2\pi|\vec{r}_1 - \vec{r}_2|} dS \tag{3.11}$$

The task is to project the field point onto the plane coinciding with the aperture, and then find the intersection of the projected spherical wave (the circle) with the active aperture as shown in Fig. 3.6.

Rewriting the integral into polar coordinates gives:

$$h(\vec{r}_1,t) = \int_{\Theta_1}^{\Theta_2} \int_{d_1}^{d_2} \frac{\delta\left(t-\frac{R}{c}\right)}{2\pi R} r dr d\Theta \tag{3.12}$$

where r is the radius of the projected circle and R is the distance from the field point to the aperture given by $R^2 = r^2+z_p^2$. Here z_p is the field point height above the x-y plane of the aperture. The projected distances $d1$, $d2$ are determined by the aperture and are the distance closest to and furthest away from the aperture, and $\Theta 1$, $\Theta 2$ are the corresponding angles for a given time (see Fig. 3.7).

Introducing the substitution $2RdR = 2rdr$ gives

$$h(\vec{r}_1,t) = \frac{1}{2\pi} \int_{\Theta_1}^{\Theta_2} \int_{R_1}^{R_2} \delta\left(t-\tfrac{R}{c}\right) dR d\Theta \tag{3.13}$$

The variables R_1 and R_2 denote the edges closest to and furthest away from the field point. Finally using the substitution $t' = R/c$ gives

$$h(\vec{r}_1,t) = \frac{c}{2\pi} \int_{\Theta_1}^{\Theta_2} \int_{t_1}^{t_2} \delta(t-t') dt' d\Theta \tag{3.14}$$

For a given time instance the contribution along the arc is constant and the integral gives

$$h(\vec{r}_1,t) = \frac{\Theta_2-\Theta_1}{2\pi} c \tag{3.15}$$

when assuming the circle arc is only intersected once by the aperture. The angles Θ_1 and Θ_2 are determined by the intersection of the aperture and the projected spherical wave, and the spatial impulse response is, thus, solely determined by these intersections, when no apodization of the aperture is used. The response can therefore be evaluated by keeping track of the intersections as a function of time.

3.4 Examples of Spatial Impulse Responses

The first example shows the spatial impulse responses from a 3×5 mm rectangle for different spatial positions 5 mm from the front face of the transducer. The responses are found from the center of the rectangle (y = 0) and out in steps of 2 mm in the x direction to 6 mm away from the center of the rectangle. A schematic diagram of the situation is shown in Fig. 3.8 For the on-axis response. The impulse response is zero before the first spherical wave reaches the aperture. Then the response stays constant at a value of c. The first edge of the aperture is met, and the response drops of. The decrease with time in increased when the next edge of the aperture is reached and the response becomes zero when the projected spherical waves all are outside the area of the aperture.

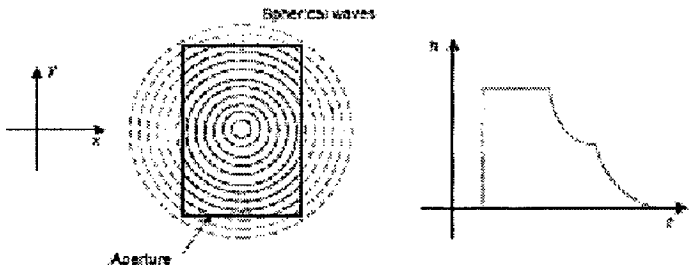

Fig. 3.8: Schematic diagram of field from rectangular element.

A plot of the results for the different lateral field positions is shown in Fig. 3.9. It can be seen how the spatial impulse response changes as a function of relative position to the aperture.

The second example shows the response from a circular, flat transducer. Two different cases are shown in Fig. 3.10. The top graph shows the traditional spatial impulse response

when no apodization is used, so that the aperture vibrates as a piston. The field is calculated 10 mm from the front face of the transducer starting at the center axis of the aperture. Twenty-one responses for lateral distance of 0 to 20 mm off axis are then shown. The same calculation is repeated in the bottom graph, when a Gaussian apodization has been imposed on the aperture.

The vibration amplitude is a factor of 1/exp(4) less at the edges of the aperture than at the center. It is seen how the apodization reduces some of the sharp discontinuities in the spatial impulse response, which can reduce the sidelobes of the field.

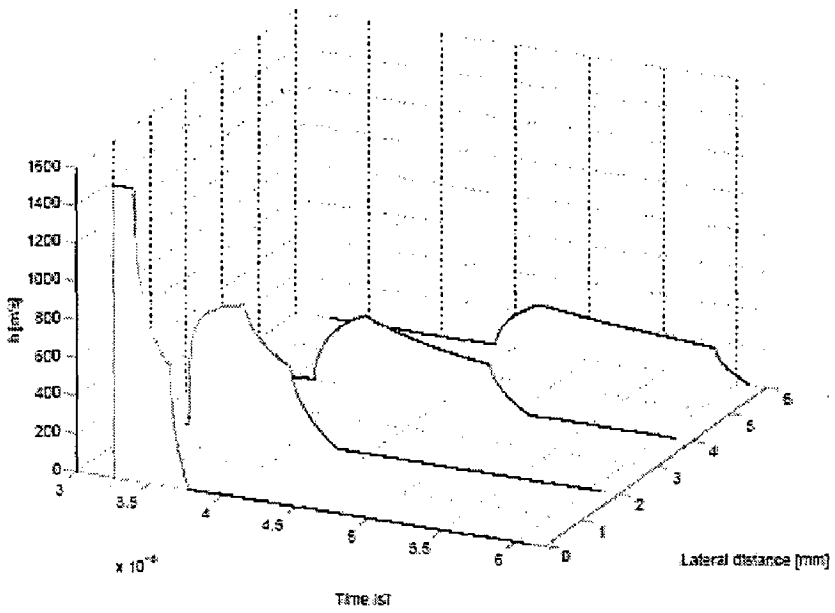

Fig. 3.9: Spatial impulse response from a rectangular aperture of 4X5 mm at for different lateral positions

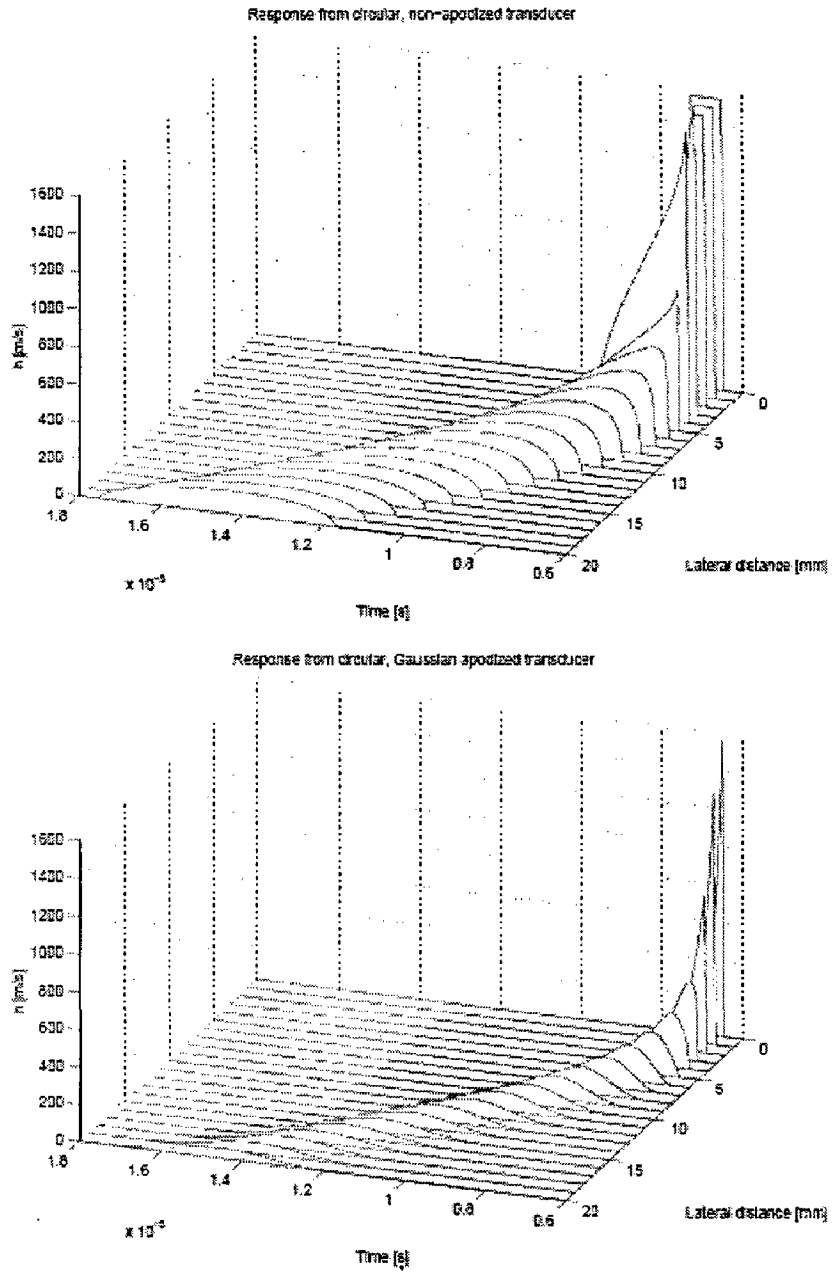

Fig 3.10: Spatial impulse response from a circular aperture. Graphs are shown without apodization of the aperture (top) and with a Gaussian apodization function (bottom). The radius of the aperture is 5 mm and the field is calculated 10 mm from the transducer surface.

3.5 Calculation of the scattered signal

In medical ultrasound, a pulsed field is emitted into the body and is scattered and reflected by density and propagation velocity perturbations. The scattered field then propagates back

through the tissue and is received by the transducer. The field is converted to a voltage signal and used for the display of the ultrasound image. A full description of a typical imaging system, using the concept of spatial impulse response, is the purpose of the section.

The received signal can be found by solving an appropriate wave equation. This has been done in a number of papers (e.g. [22], [23]). Gore and Leeman [22] considered a wave equation where the scattering term was a function of the adiabatic compressibility and the density. The transducer was modeled by axial and lateral pulses that were separable. Fatemi and Kak [23] used a wave equation where scattering originated only from velocity fluctuations, and the transducer was restricted to be circularly symmetric and unfocused (flat).

The scattering term for the wave equation used here is a function of density and propagation velocity perturbations, and the wave equation is equivalent to the one used by Gore and Leeman [22]. No restrictions are enforced on the transducer geometry or its excitation, and analytic expressions for a number of geometries can be incorporated into the model.

The model includes attenuation due to propagation and scattering, but not the dispersive attenuation observed for propagation in tissue.

The derivation is organized as follows. The following section derives the wave equation and describes the different linearity assumptions made. Section 3.5.2 calculates the scattered field and section 3.5.3 introduces the spatial impulse response model for the incident field. Section 3.5.4 combines the wave equation solution and the transducer model to give the final equation for the received pressure field.

3.5.1 Derivation of the Wave Equation

This section derives the wave equation. The section has been included in order to explain in detail the different linearity assumptions and approximations made to obtain a solvable wave equation. The derivation closely follows that developed by Chernov (1960).

The first approximation states that the instantaneous acoustic pressure and density can be written

$$P_{ins}(\vec{r},t) = P + p_1(\vec{r},t) \tag{3.16}$$

$$\rho_{ins}(\vec{r},t) = \rho(\vec{r}) + \rho_1(\vec{r},t) \tag{3.17}$$

in which P is the mean pressure of the medium and p is the density of the undisturbed medium. Here p1 is the pressure variation caused by the ultrasound wave and is considered small compared to P and p1 is the density change caused by the wave. Both p1 and p1 are small quantities of first order.

Our second assumption is that no heat conduction or conversion of ultrasound to thermal energy takes place. Thus, the entropy is constant for the process, so that the acoustic pressure and density satisfy the adiabatic equation [24]:

$$\frac{dP_{ins}}{dt} = c^2 \frac{d\rho_{ins}}{dt} \tag{3.18}$$

The equation contains total derivatives, as the relation is satisfied for a given particle of the tissue rather than at a given point in space. This is the Lagrange description of the motion [6]. For our purpose the Euler description is more appropriate. Here the coordinate system is fixed in space and the equation describes the properties of whatever particle of fluid there is at a given point at a given time. Converting to an Eulerian description results in the following constitutive equation [24], [6]:

$$\frac{1}{c^2}\frac{\partial p_1}{\partial t} = \frac{\partial p_1}{\partial t} + \vec{u}.\nabla\rho \tag{3.19}$$

using that P and p do not depend on time and that p1 is small compared to p. Here u is the particle velocity, V is the gradient operator, and • symbolizes the scalar product.

The pressure, density, and particle velocity must also satisfy the hydrodynamic equations [24]:

$$\rho_{ins}\frac{d\vec{u}}{dt} = -\nabla P_{ins} \tag{3.20}$$

$$\frac{\partial \rho_{ins}}{\partial t} = -\nabla.\left(\rho_{ins}\vec{u}\right) \tag{3.21}$$

which are the dynamic equation and the equation of continuity. Using (3.16) and (3.17) and discarding higher order terms we can write

$$\rho\frac{d\vec{u}}{dt} = -\nabla p_1 \tag{3.22}$$

$$\frac{\partial \rho_1}{\partial t} = -\nabla.\left(\rho\vec{u}\right) \tag{3.23}$$

Differentiating (3.23) with respect to t and inserting (3.22) gives

$$\frac{\partial^2 \rho_1}{\partial^2 t} = -\nabla.\left(\rho\frac{\partial \vec{u}}{\partial t}\right) = -\nabla.\left(-\nabla p_1\right) = \nabla^2 p_1 \tag{3.24}$$

Differentiating (3.19) with respect to t

$$\frac{1}{c^2}\frac{\partial^2 \rho_1}{\partial^2 t} = \frac{\partial^2 \rho_1}{\partial^2 t} + \frac{\partial \vec{u}}{\partial t}.\nabla\rho \tag{3.25}$$

and inserting (3.24) and (3.22) leads to

$$\nabla^2 p_1 - \frac{1}{c^2}\frac{\partial^2 \rho_1}{\partial^2 t} = \frac{1}{\rho}\nabla\rho.\nabla p_1 \tag{3.26}$$

Assuming that the propagation velocity and the density only vary slightly from their mean values yields

$$\rho(\vec{r}) = \rho_0 + \Delta\rho(\vec{r})$$

$$c(\vec{r}) = c_0 + \Delta c(\vec{r}) \tag{3.27}$$

where $\rho_0 >> \Delta\rho$ and $c_0 >> \Delta c$.

$$\nabla^2 p_1 - \frac{1}{(c_0 + \Delta c)^2}\frac{\partial^2 \rho_1}{\partial^2 t} = \frac{1}{(\rho_0 + \Delta\rho)}\nabla(\rho_0 + \Delta\rho).\nabla p_1 \tag{3.28}$$

Ignoring small quantities of second order and using the approximation ($\Delta << 1$):

$$\frac{1}{1+\Delta} \approx 1 - \Delta \tag{3.29}$$

gives

$$\nabla^2 p_1 - \left(\frac{1}{c_0^{\,2}} - \frac{2\Delta c}{c_0^{\,3}}\right)\frac{\partial^2 p_1}{\partial^2 t} = \left(\frac{1}{\rho}\nabla(\Delta\rho) - \frac{\nabla\rho}{\rho_0^{\,2}}\nabla(\Delta\rho)\right).\nabla p_1 \tag{3.30}$$

Neglecting the second order term $\frac{\nabla\rho}{\rho_0^{\,2}}\nabla(\Delta\rho).\nabla p_1$ yields the wave equation:

$$\nabla^2 p_1 - \frac{1}{c_0^{\,2}}\frac{\partial^2 p_1}{\partial t^2} = -\frac{2\Delta c}{c_0^{\,3}}\frac{\partial^2 p_1}{\partial t^2} + \frac{1}{\rho_0}\nabla(\Delta\rho).\nabla p_1 \tag{3.31}$$

The two terms on the right side of the equation are the scattering terms which vanish for a homogeneous medium. The wave equation was derived by Chernov [24]. It has also been considered in Gore & Leeman [22] and Morse & Ingard [6] in a slightly different form, where the scattering terms were a function of the adiabatic compressibility κ and the density.

3.5.2 Calculation of the Scattered Field

Having derived a suitable wave equation, we now calculate the scattered field from a small inhomogeneity embedded in a homogeneous surrounding. The scene is depicted in Fig. 3.11. The inhomogeneity is identified by $\vec{r}_1$ and enclosed in the volume V0. The scattered field is calculated at the point indicated by $\vec{r}_2$ integrating all the spherical waves emanating from the scattering region V' using the time dependent Green's function for unbounded space. Thus, the scattered field is [6], [22]:

$$p_z(\vec{r}_2,t)=\int_{V'}\int_{T}\left[\frac{1}{\rho_0}\nabla\left(\Delta\rho(\vec{r}_1)\right).\nabla p_1(\vec{r}_1,t_1)-\frac{2\Delta c(\vec{r}_1)}{c_0^{\,3}}\frac{\partial^2 p_1(\vec{r}_1,t)}{\partial t^2}\right]G(\vec{r}_1,t_1/\vec{r}_2,t)\,dt_1 d^3\vec{r}_1 \tag{3.32}$$

where G is the free space Green's function:

$$G(\vec{r}_1,t_1/\vec{r}_2,t)=\frac{\delta\left(t-t_1-\frac{|\vec{r}_2-\vec{r}_1|}{c_0}\right)}{4\pi|\vec{r}_2-\vec{r}_1|} \tag{3.33}$$

$d^3\vec{r}_1$ means integrating w.r.t. $\vec{r}_2$ over the volume V_0, and T denotes integration over time.

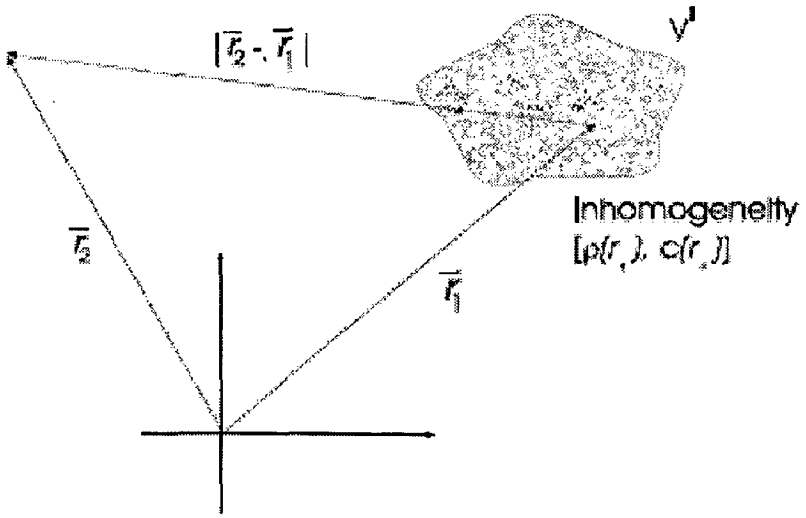

Fig. 3.11: Coordinate system for calculating the scattered field

We denote by

$$F_{op} = \frac{1}{\rho_0}\nabla\left(\Delta\rho(\vec{r}_1)\right).\nabla - \frac{2\Delta c(\vec{r}_1)}{c_0^{\,3}}\frac{\partial^2}{\partial t^2} \tag{3.34}$$

the scattering operator.

The pressure field inside the scattering region is:

$$p_1(\vec{r},t) = p_i(\vec{r},t) + p_2(\vec{r},t) \tag{3.35}$$

where p_i is the incident pressure field. As can be seen, the integral can not be solved directly. To solve it we apply the Born-Neumann expansion [25]. If G_i symbolizes the integral operator representing Green's function and the integration and *Fop* the scattering operator, then the first order Born approximation can be written:

$$p_{z_1}(\vec{r}_2,t) = G_1 F_{op} p_1(\vec{r}_1,t_1) \tag{3.36}$$

Here p_s has been set to zero in (3.35). Inserting p_{s1} in (3.35) and then in (3.32) we arrive at

$$\begin{aligned} p_{z_2}(\vec{r}_2,t) &= G_i F_{op}\left[p_1(\vec{r}_1,t_1) + G_i F_{op} p_i(\vec{r}_1,t_1)\right] \\ &= G_i F_{op} p_i(\vec{r}_1,t_1) + \left[G_i F_{op}\right]^2 p_i(\vec{r}_1,t_1) \end{aligned} \tag{3.37}$$

It is emphasized here that G_i indicates an integral over $\vec{r}_1$ and t_1, and not the pressure at point $\vec{r}_1$ and time t_1 but over the volume of V_0 and time T indicated by $\vec{r}_1$ and t_1.
The general expression for the scattered field then is:

$$
\begin{aligned}
p_{z_2}(\vec{r}_2,t) &= G_i F_{op}\, p_i(\vec{r}_1,t_1) + \\
&\left[G_i F_{op}\right]^2 p_i(\vec{r}_1,t_1) + \\
&\left[G_i F_{op}\right]^3 p_i(\vec{r}_1,t_1) + \\
&\left[G_i F_{op}\right]^4 p_i(\vec{r}_1,t_1) + \ldots\ldots
\end{aligned}
\tag{3.38}
$$

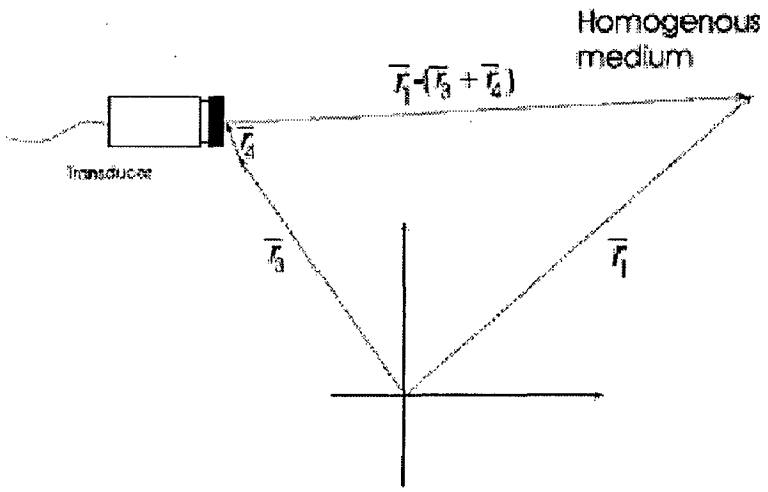

Fig. 3.12: Coordinate system for calculating the incident field.

Terms involving $[G_iF_{op}]^N$ pi($\vec{r}_1$, t_1), where $N > 1$, describe multiple scattering of order N. Usually the scattering from small obstacles is considered weak so higher order terms can be neglected. Thus, a useful approximation is to employ only the first term in the expansion. This corresponds to the first order Born-approximation.

Using this (3.32) can be approximated by (note the replacement of $p_1(\vec{r}_1, t_1)$ with $p_i(\vec{r}_1, t_1)$)

$$
p_z(\vec{r}_2,t) \approx \int_{V'}\int_T \left[\frac{1}{\rho_0}\nabla\left(\Delta\rho(\vec{r}_1)\right).\nabla p_i(\vec{r}_1,t_1) - \frac{2\Delta c(\vec{r}_1)}{c_0^{\,3}}\frac{\partial^2 p_i(\vec{r}_1,t)}{\partial t^2}\right] G(\vec{r}_1,t_1 \mid \vec{r}_2,t)\, dt_1 d^3\vec{r}_1 \tag{3.39}
$$

So in order to calculate the scattered field, the incident field for the homogeneous medium must be calculated.

3.5.3 Calculation of the Incident Field

The incident field is generated by the ultrasound transducer assuming no other sources exist in the tissue. The field is conveniently calculated by employing the velocity potential $\psi(\vec{r}$, t), and enforcing appropriate boundary conditions [26], [27]. The velocity potential satisfies the following wave equation for the homogeneous medium:

$$\nabla^2\Psi - \frac{1}{co^2}\frac{\partial^2\Psi}{\partial t^2} = 0 \tag{3.40}$$

and the pressure is calculated from:

$$p(\vec{r},t) = \rho_o \frac{\partial\Psi(\vec{r},t)}{\partial t} \tag{3.41}$$

The coordinate system shown in Fig. 3.12 is used in the calculation. The particle velocity normal to the transducer surface is denoted by $v(\vec{r}_3+\vec{r}_4$,t), where $\vec{r}_3$ identifies the position of the transducer and $\vec{r}_4$ a point on the transducer surface relative to $\vec{r}_3$.

The solution to the homogeneous wave equation is [27]:

$$\Psi(\vec{r}_1+\vec{r}_3,t) = \int_S\int_T v(\vec{r}_3+\vec{r}_4+t_3)g(\vec{r}_1,,t\,|\,\vec{r}_3+\vec{r}_4,t_3)dt_3d^2\vec{r}_4 \tag{3.42}$$

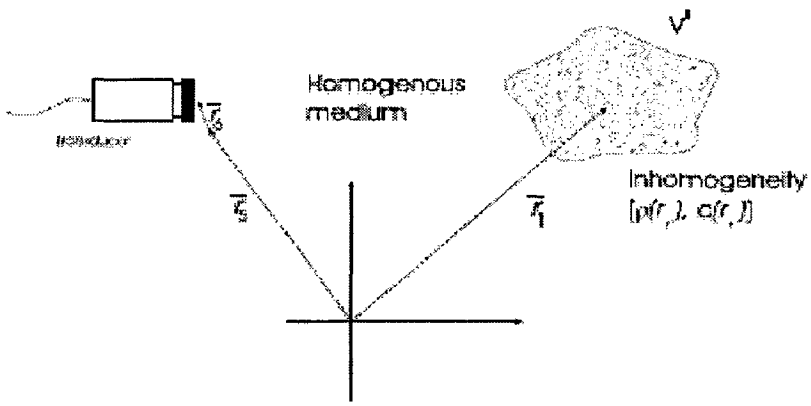

Fig. 3.13: Coordinate system for calculating the received signal.

when the transducer is mounted in a rigid infinite planar baffle. S denotes the transducer surface.

g is the Green's function for a bounded medium and is

$$g(\vec{r}_1,t\,|\,\vec{r}_3,t_3)=\frac{\partial(t-t_3-\frac{|\vec{r}_1-\vec{r}_3-\vec{r}_4|}{c_0})}{2\pi\,|\vec{r}_1-\vec{r}_3-\vec{r}_4|} \tag{3.43}$$

$|\vec{r}_1-\vec{r}_3-\vec{r}_4|$ is the distance from S to the point where the field is calculated and c_0 the mean propagation velocity. The field is calculated under the assumption of radiation into an isotropic, homogeneous, non-dissipative medium.

If a slightly curved transducer is used, an additional term is introduced as shown in Morse & Feshbach [28]. This term is called the second order diffraction term in Penttinen & Luukkala [13]. It can be shown to vanish for a planar transducer, and as long as the transducer is only slightly curved and large compared to the wavelength of the ultrasound, the resulting expression is a good approximation to the pressure field [13].

If the particle velocity is assumed to be uniform over the surface of the transducer, (3.42) can be reduced to [29]:

$$\Psi(\vec{r}_1+\vec{r}_3,t)=\int_T v(t_3)g(\vec{r}_1,t\,|\,\vec{r}_3+\vec{r}_4,t_3)d^2\vec{r}_4dt_3 \tag{3.44}$$

This is the spatial impulse response previously derived, and the sound pressure for the incident field then is:

$$p(\vec{r}_1,\vec{r}_3,t)=\rho_o\frac{\partial\Psi(\vec{r}_1,\vec{r}_3,t)}{\partial t}=\rho_o v(t)\overset{*}{t}\frac{\partial h(\vec{r}_1,\vec{r}_3,t)}{\partial t} \tag{3.45}$$

or

$$p(\vec{r}_1,\vec{r}_3,t)=\rho_o\frac{\partial v(t)}{\partial t}\overset{*}{t}h(\vec{r}_1,\vec{r}_3,t) \tag{3.46}$$

3.5.4 Calculation of the Received Signal

The received signal is the scattered pressure field integrated over the transducer surface, convolved with the electromechanical impulse response, $E_m(t)$, of the transducer. To calculate this we introduce the coordinate system shown in Fig.3.13. $\vec{r}_6+\vec{r}_5$ indicates a receiving element on the surface of the transducer that is located at r5. The received signal is:

$$p_r(\vec{r}_5,t) = E_m(t) \overset{\bullet}{t} \int_S p_s(\vec{r}_6+\vec{r}_5,t) d_2\vec{r}_6 \tag{3.47}$$

The scattered field is:

$$p_s(\vec{r}_6+r_5,t) = \frac{1}{2}\int_{V'}\int_T F_{op}[p_i(\vec{r}_1,t)] \frac{\delta\left(t-t_1-\frac{(|\vec{r}_6+\vec{r}_5-\vec{r}_1|)}{c_0}\right)}{2\pi|\vec{r}_6+\vec{r}_5-\vec{r}_1|} dt_1 d^3\vec{r}_1 \tag{3.48}$$

Combining this with (3.47) and comparing with (3.9) we see that pr includes Green's function for bounded space integrated over the transducer surface, which is equal to the spatial impulse response. Inserting the expression for pi and performing the integration over the transducer surface and over time, results in:

$$p_r(\vec{r}_5,t) = E_m(t) *_t \frac{1}{2}\left[\int_{V'} F_{op}\rho_0 \frac{\partial v}{\partial t} *_t \vec{h}(\vec{r}_1,\vec{r}_5,t)\right] *_t \vec{h}(\vec{r}_5,\vec{r}_1,t) d^3\vec{r}_1 \tag{3.49}$$

If the position of the transmitting and the receiving transducer is the same ($\vec{r}_3 = \vec{r}_5$), then a simple rearrangement of (3.49) yields:

$$p_r(\vec{r}_5,t) = \frac{\rho_0}{2} E_m(t) *_t \frac{\partial v}{\partial t} *_t \int_{V'} F_{op} h_{pe}(\vec{r}_5,\vec{r}_1,t) d^3\vec{r}_1 \tag{3.50}$$

where

$$h_{pe}(\vec{r}_5,\vec{r}_1,t) = h(\vec{r}_5,\vec{r}_1,t) *_t h(\vec{r}_1,\vec{r}_5,t) \tag{3.51}$$

is the pulse-echo spatial impulse response.

The calculated signal is the response measured for one given position of the transducer. For a B-mode scan picture a number of scan-lines is measured and combined to a picture. To analyze this situation, the last factor in (3.50) is explicitly written out

$$\int_{V'}\left[\frac{1}{\rho_0}\nabla\left(\Delta\rho(\vec{r}_1)\right).\nabla h_{pe}(\vec{r}_1,\vec{r}_5,t)-\frac{2\Delta c(\vec{r}_1)}{c_0^{\,3}}\frac{\partial^2 h_{pe}(\vec{r}_1,\vec{r}_5,t)}{\partial t^2}\right]d^3\vec{r}_1 \qquad (3.52)$$

From section 3.5.3 it is know that H_{pe} is a function of the distance between $\vec{r}_1$ and $\vec{r}_5$, while $\Delta\rho$, Δc only are functions of $\vec{r}_1$. So when $\vec{r}_5$ is varied over the volume of interest, the resulting image is a spatial non-stationary convolution between $\Delta\rho$, Δc and a modified form of the pulse-echo spatial impulse response.

If we assume that the pulse-echo spatial impulse is slowly varying so that the spatial frequency content is constant over a finite volume, then (3.52) can be rewritten

$$\int_{V'}\left[\frac{1}{\rho_0}\Delta\rho(\vec{r}_1).\nabla^2 h_{pe}(\vec{r}_1,\vec{r}_5,t)-\frac{2\Delta c(\vec{r}_1)}{c_0^{\,3}}\frac{\partial^2 h_{pe}(\vec{r}_1,\vec{r}_5,t)}{\partial t^2}\right]d^3\vec{r}_1 \qquad (3.53)$$

h_{pe} is a function of the distance between the transducer and the scatterer or equivalently of the corresponding time given by

$$t=\frac{|\vec{r}_1-\vec{r}_5|}{c_0} \qquad (3.54)$$

The Laplace operator is the second derivative w.r.t. the distance, which can be approximated with the second derivative w.r.t. time. So

$$\nabla^2 h_{pe}(\vec{r}_1,\vec{r}_5,t)=\frac{1}{c_0^{\,2}}\frac{\partial^2 h_{pe}(\vec{r}_1,\vec{r}_5,t)}{\partial t^2} \qquad (3.55)$$

assuming only small deviations from the mean propagation velocity.

Using these approximations, (3.50) can be rewritten:

$$p_r(\vec{r}_5,t)=\frac{\rho_0}{2c_0{}^2}E_m(t)*_t\frac{\partial v^3(t)}{\partial t^3}*_t\int_{V'}\left[\frac{\Delta\rho(\vec{r}_1)}{\rho_0}-\frac{2\Delta c(\vec{r}_1)}{c_0}\right]\vec{h}_{pe}(\vec{r}_1,\vec{r}_5,t)d^3\vec{r}_1 \tag{3.56}$$

Symbolically this is written

$$p_r(\vec{r}_5,t)=v_{pe}*_t f_m(\vec{r}_1)*_t h_{pe}(\vec{r}_1,\vec{r}_5,t) \tag{3.57}$$

$*_r$denotes spatial convolution. v_{pe} is the pulse-echo wavelet which includes the transducer excitation and the electro-mechanical impulse response during emission and reception of the pulse. f_m accounts for the inhomogeneities in the tissue due to density and propagation velocity perturbations which give rise to the scattered signal. h_{pe} is the modified pulse-echo spatial impulse response that relates the transducer geometry to the spatial extent of the scattered field. Explicitly written out these terms are:

$$v_{pe}(t)=\frac{p_0}{2c_0{}^2}E_m(t)*_t\frac{\partial v^3 t}{\partial t^3} \tag{3.58}$$

$$f_m(\vec{r}_1)=\frac{\Delta\rho(\vec{r}_1)}{\rho_0}-\frac{2\Delta c(\vec{r}_1)}{c_0} \tag{3.59}$$

$$h_{pe}(\vec{r}_1,\vec{r}_5,t)=h(\vec{r}_1,\vec{r}_5,t)*_t h(\vec{r}_5,\vec{r}_1,t) \tag{3.60}$$

Expression (3.57) consists of three distinct terms. The interesting signal, and the one that should be displayed in medical ultrasound, is $fm(\vec{r}_1)$. We, however, measure a time and spatially smoothed version of this, which obscures the finer details in the picture. The smoothing consists of a convolution in time with a fixed wavelet $v_{pe}(t)$ and a spatial convolution with a spatially varying $h_{pe}(\vec{r}_1,\vec{r}_5,t)$.

CHAPTER 4
ULTRASOUND IMAGING

Modern medical ultrasound scanners are used for imaging nearly all soft tissue structures in the body. The anatomy can be studied from gray-scale B-mode images, where the reflectivity and scattering strength of the tissues are displayed. The imaging is performed in real time with 20 to 100 images per second. The technique is widely used since it does not use ionizing radiation and is safe and painless for the patient.

This chapter gives a short introduction to modern ultrasound imaging using array transducers. Part of the chapter is based on [4] and [32].

4.1 Fourier Relation

This section derives a simple relation between the oscillation of the transducer surface and the ultrasound field. It is shown that field in the far-field can be found by a simple one-dimensional Fourier transform of the one-dimensional aperture pattern. This might seem far from the actual imaging situation in the near field using pulsed excitation, but the approach is very convenient in introducing all the major concepts like main and side lobes, grating lobes, etc. It also very clearly reveals information about the relation between aperture properties and field properties.

4.1.1 Derivation of Fourier Relation

Consider a simple line source as shown in Fig. 4.1 with a harmonic particle speed of $Uo\exp(j\omega t)$. Here Uo is the vibration amplitude and ω is its angular frequency. The line element of length dx generates an increment in pressure of [8]

$$dp = j\frac{\rho_o ck}{4\pi r'}U_o a_p(x)e^{j(\omega t-kr')}dx \tag{4.1}$$

where ρ_o is density, c is speed of sound, $k = \omega/c$ is the wave number, and $a_p(x)$ is an amplitude scaling of the individual parts of the aperture. In the far-field ($r<<L$) the distance from the radiator to the field points is (see Fig. 4.1)

$$r' = r - x \sin\theta \qquad (4.2)$$

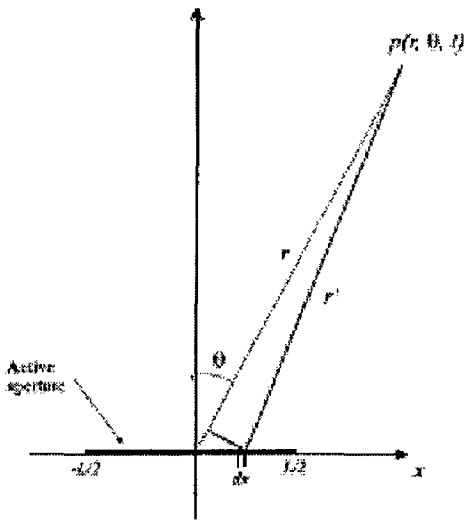

Fig. 4.1: Geometry for line aperture.

The emitted pressure is found by integrating over all the small elements of the aperture

$$p(r,\theta,t) = j\frac{\rho_o c U_o k}{4\pi}\int_{-\infty}^{+\infty} a_p(x)\frac{e^{j(\omega t - r')}}{r'}dx \qquad (4.3)$$

Notice that $ap(x) = 0$ if $|x| > L/2$. Here r' can be replaced with r, if the extent of the array is small compared to the distance to the field point ($r << L$). Using this approximation and inserting (4.2) in (4.3) gives

$$p(r,\theta,t) = j\frac{\rho_o c U_o k}{4\pi}\int_{-\infty}^{+\infty} a_p(x)e^{j(\omega t - kr + kx\sin\theta)}dx = \frac{\rho_o c U_o k}{4\pi r}e^{j(\omega t - kr)}\int_{-\infty}^{+\infty} a_p(x)e^{jkx\sin\theta}dx \qquad (4.4)$$

since ωt and kr are independent of x. Hereby the pressure amplitude of the field for a given frequency can be split into two factors:

$$\begin{aligned} P_{ax}(r) &= \frac{\rho_o c U_o k L}{4\pi r} \\ H(\theta) &= \frac{1}{L}\int_{-\infty}^{+\infty} a_p(x) e^{jkx\sin\theta}\, dx \\ P(r,\theta) &= P_{ax}(r) H(\theta) \end{aligned} \tag{4.5}$$

The first factor $P_{ax}(r)$ characterizes how the field drops off in the axial direction as a factor of distance, and $H(\theta)$ gives the variation of the field as a function of angle. The first term drops off with 1/r as for a simple point source and $H(\theta)$ is found from the aperture function $a_p(x)$. A slight rearrangement gives

$$H(\theta) = \frac{1}{L}\int_{-\infty}^{+\infty} a_p(x) e^{j2\pi f \frac{\sin\theta}{c}}\, dx = \frac{1}{L}\int_{-\infty}^{+\infty} a_p(x) e^{j2\pi f' x}\, dx \tag{4.6}$$

This very closely resembles the standard Fourier integral given by

$$\begin{aligned} G(f) &= \int_{-\infty}^{+\infty} g(t) e^{-j2\pi f t}\, dt \\ g(t) &= \int_{-\infty}^{+\infty} G(f) e^{j2\pi f t}\, dt \end{aligned} \tag{4.7}$$

There is, thus, a Fourier relation between the radial beam pattern and the aperture function, and the normal Fourier relations can be used for understanding the beam patterns for typical apertures.

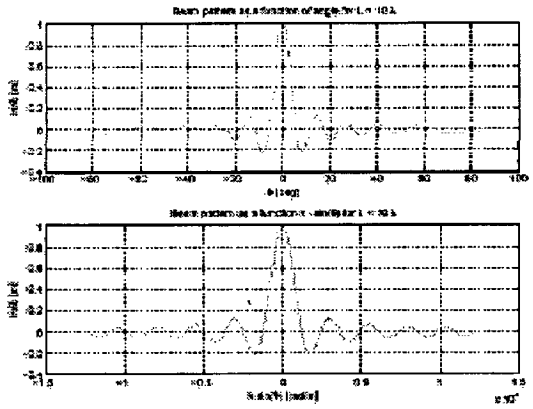

Fig. 4.2: Angular beam pattern for a line aperture with a uniform aperture function as a function of angle (top) and as a function of k sin(θ) (bottom).

4.1.2 Beam Patterns

The first example is for a simple line source, where the aperture function is constant such that

$$a_p(x) = \begin{cases} 1, & |x| \leq L/2 \\ 0, & else \end{cases} \tag{4.8}$$

The angular factor is then

$$H(\theta) = \frac{\sin(\pi L f \frac{\sin\theta}{c})}{\pi L f \frac{\sin\theta}{c}} = \frac{\sin(\frac{k}{2} L \sin\theta)}{\frac{k}{2} L \sin\theta} \tag{4.9}$$

A plot of the sinc function is shown in Fig. 4.2. A single main lobe can be seen with a number of side lobe peaks. The peaks fall off proportionally to k or f. The angle of the first zero in the function is found at

$$\sin\theta = \frac{c}{Lf} = \frac{\lambda}{L} \tag{4.10}$$

The angle is, thus, dependent on the frequency and the size of the array. A large array or a high emitted frequency, therefore, gives a narrow main lobe. The magnitude of the first sidelobe relative to the mainlobe is given by

$$\frac{H(\arcsin(\frac{3c}{2Lf}))}{H(0)} = L\frac{\sin(\frac{3\pi}{2})}{\frac{3\pi}{2}} \tag{4.11}$$

The relative sidelobe level is, thus, independent of the size of the array and of the frequency, and is solely determined by the aperture function $a_p(x)$ through the Fourier relation. The large discontinuities of $a_p(x)$, thus, give rise to the high side lobe level, and they can be reduced by selecting an aperture function that is smoother like a Hanning window or a Gaussian shape.

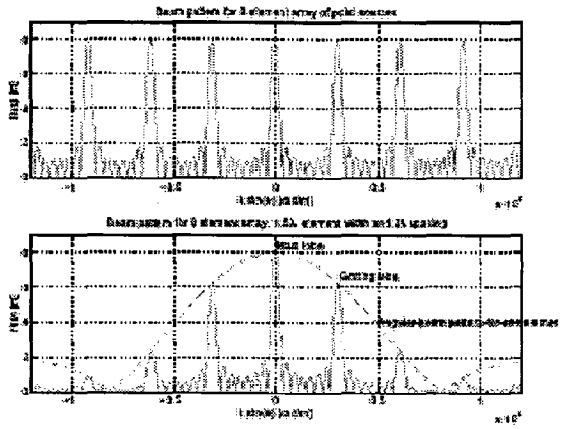

Fig 4.3: Grating lobes for array transducer consisting of 8 point elements (top) and of 8 elements with a size of 1.5 λ (bottom). The pitch (or distance between the elements) is 2 λ

Modern ultrasound transducers consist of a number of elements each radiating ultrasound energy. Neglecting the phasing of the element (see Section 4.2) due to the far-field assumption, the aperture function can be described by

$$a_p(x) = a_{ps}(x) * \sum_{n=-N/2}^{N/2} \partial(x - d_x n) \tag{4.12}$$

where *aps*(*x*) is the aperture function for the individual elements, *dx* is the spacing (pitch) between the centers of the individual elements, and *N* is the number of elements in the array. Using the Fourier relationship the angular beam pattern can be described by

$$H_r(\theta) = H_{ps}(\theta) H_{per}(\theta) \tag{4.13}$$

where

$$\sum_{n=-N/2}^{N/2} \partial(x-d_x n) \leftrightarrow H_{per}(\theta) = \sum_{n=-N/2}^{N/2} e^{-jnd_x k\sin\theta} = \sum_{n=-N/2}^{N/2} e^{-j2\pi\frac{f\sin\theta}{c}nd_x} \tag{4.14}$$

Summing the geometric series gives

$$H_{per}(\theta) = \frac{\sin((N+1)\frac{k}{2}d_x\sin\theta)}{\sin(\frac{k}{2}d_x\sin\theta)} \tag{4.15}$$

is the Fourier transform of series of delta functions. This function repeats itself with a period that is a multiple of

$$\begin{aligned} \pi &= \frac{\pi}{2}d_x\sin\theta \\ \sin\theta &= \frac{\pi}{kd_x} = \frac{\lambda}{d_x} \end{aligned} \tag{4.16}$$

This repetitive function gives rise to the grating lobes in the field. An example is shown in Fig. 4.3. The grating lobes are due to the periodic nature of the array, and correspond to sampling of a continuous time signal. The grating lobes will be outside a ±90 deg. imaging area if

$$\begin{aligned} \frac{\lambda}{d_x} &= 1 \\ d_x &= \lambda \end{aligned} \tag{4.17}$$

Often the beam is steered in a direction and in order to ensure that grating lobes do not appear in the image, the spacing or pitch of the elements is selected to be $d_x = \lambda/2$. This also includes ample margin for the modern transducers that often have a very broad bandwidth. An array beam can be steered in a direction by applying a time delay on the individual elements. The difference in arrival time for a given direction θ_0 is

$$\tau = \frac{d_x\sin\theta_o}{c} \tag{4.18}$$

Steering in a direction θ_0 can, therefore, be accomplished by using

$$\sin\theta_o = \frac{c\tau}{d_x} \tag{4.19}$$

where τ is the delay to apply to the signal on the element closest to the center of the array. A delay of 2τ is then applied on the second element and so forth. The beam pattern for the grating lobe is then replaced by

$$H_{per}(\theta) = \frac{\sin((N+1)\frac{k}{2}d_x \sin\theta - \frac{c\tau}{d_x})}{\sin(\frac{k}{2}d_x \sin\theta - \frac{c\tau}{d_x})} \tag{4.20}$$

Notice that the delay is independent of frequency, since it is essentially only determined by the speed of sound.

4.2 Focusing

The essence of focusing an ultrasound beam is to align the pressure fields from all parts of the aperture to arrive at the field point at the same time. This can be done through a physically curved aperture, through a lens in front of the aperture, or by the use of electronic delays for multi-element arrays. All seek to align the arrival of the waves at a given point through delaying or advancing the fields from the individual elements. The delay (positive or negative) is determined using ray acoustics. The path length from the aperture to the point gives the propagation time and this is adjusted relative to some reference point. The propagation from the center of the aperture element to the field point is

$$t_i = \frac{1}{c}\sqrt{(x_i - x_f)^2 + (y_i - y_f)^2 + (z_i - z_f)^2} \tag{4.21}$$

where (x_f,y_f,z_f) is the position of the focal point, (x_i,y_i,z_i) is the center for the physical element number *i*, *c* is the speed of sound, and *ti* is the calculated propagation time.

A point is selected on the whole aperture as a reference for the imaging process. The propagation time for this is

$$t_c = \frac{1}{c}\sqrt{(x_c - x_f)^2 + (y_c - y_f)^2 + (z_c - z_f)^2} \tag{4.22}$$

where (*xc, yc; zc*) is the reference center point on the aperture. The delay to use on each element of the array is then

$$\Delta t_i = \frac{1}{c}\sqrt{(x_c - x_f)^2 + (y_c - y_f)^2 + (z_c - z_f)^2} - \sqrt{(x_i - x_f)^2 + (y_i - y_f)^2 + (z_i - z_f)^2} \qquad (4.23)$$

Notice that there is no limit on the selection of the different points, and the beam can, thus, be steered in a preferred direction.

The arguments here have been given for emission from an array, but they are equally valid during reception of the ultrasound waves due to acoustic reciprocity. At reception it is also possible to change the focus as a function of time and thereby obtain a dynamic tracking focus. This is used by all modern ultrasound scanners, Beamformers based on analog technology makes it possible to create several receive foci and the newer digital scanners change the focusing continuously for every depth in receive. A single focus is only possible in transmit and composite imaging is therefore often used in modern imaging. Here several pulse emissions with focusing at different depths in the same direction are used and the received signals are combined to form one image focused in both transmit and receive at different depths (composit imaging).

The focusing can, thus, be defined through time lines as:

From time	Focus at
0	x_1, y_1, z_1
t_1	x_1, y_1, z_1
t_2	x_2, y_2, z_2
...	
...	

For each focal zone there is an associated focal point and the time from which this focus is used. The arrival time from the field point to the physical transducer element is used for deciding which focus is used. Another possibility is to set the focusing to be dynamic, so that the focus is changed as a function of time and thereby depth. The focusing is then set as a direction defined by two angles and a starting point on the aperture.

Section 4.1 showed that the side and grating lobes of the array can be reduced by employing apodization of the elements. Again a fixed function can be used in transmit and a dynamic function in receive defined by

From time	Apodize with
0	$a_{1,1}, a_{1,2}, a_{1,3} \ldots a_{1,Ne}$
t1	$a_{1,1}, a_{1,2}, a_{1,3} \ldots a_{1,Ne}$
t2	$a_{2,1}, a_{2,2}, a_{2,3} \ldots a_{2,Ne}$
t3	$a_{3,1}, a_{3,2}, a_{3,3} \ldots a_{3,Ne}$
.	.....
.	.....

Here $a_{1,1}$ is the amplitude scaling value multiplied onto element 1 after time instance $t1$. Typically a Hamming or Gaussian shaped function is used for the apodization. In receive the width of the function is often increased to compensate for attenuation effects and for keeping the point spread function roughly constant. The F-number defined by

$$F = \frac{D}{L} \tag{4.25}$$

where L is the total width of the active aperture and D is the distance to the focus, is often kept constant. More of the aperture is often used for larger depths and a compensation for the attenuation is thereby partly made. An example of the use of dynamic apodization is given in Section 4.6.

4.3 Fields from Array Transducers

Most modern scanners use arrays for generating and receiving the ultrasound fields. These fields are quite simple to calculate, when the spatial impulse response for a single element is known. This is the approach used in the Field II program, and this section will extend the spatial impulse response to multi element transducers and will elaborate on some of the features derived for the fields in Section 4.1.

Since the ultrasound propagation is assumed to be linear, the individual spatial impulse responses can simply be added. If $h_e(\vec{r}_p, t)$ denotes the spatial impulse response for the element at position $\vec{r}_i$ and the field point $\vec{r}_p$, then the spatial impulse response for the array is

$$h_a(\vec{r}_p,t)=\sum_{i=0}^{N-1} he(\vec{r}_i,\vec{r}_p,t) \tag{4.25}$$

assuming all N elements to be identical.

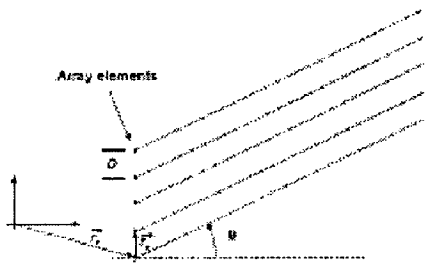

Fig. 4.4: Geometry of linear array

Let us assume that the elements are very small and the field point is far away from the array, so *it is* a Dirac function. Then

$$h_a(\vec{r}_p,t)=\frac{k}{R_p}\sum_{i=0}^{N-1}\partial(t-\frac{|\vec{r}_i-\vec{r}_p|}{c}) \tag{4.26}$$

when $R_p=|\vec{r}_i-\vec{r}_p|$, k is a constant of proportionality, and $\vec{r}_a$ is the position of the array. Thus, h_a is a train of Dirac pulses. If the spacing between the elements is D, then

$$h_a(\vec{r}_p,t)=\frac{k}{R_p}\partial\sum_{i=0}^{N-1}(t-\frac{|\vec{r}_a+iD\vec{r}_e-\vec{r}_p|}{c}) \tag{4.27}$$

where $\vec{r}_e$ is a unit vector pointing in the direction along the elements. The geometry is shown in Fig. 4.4. The difference in arrival time between elements far from the transducer is

$$\Delta t=\frac{D\sin\Theta}{c} \tag{4.28}$$

The spatial impulse response is, thus, a series of Dirac pulses separated by Δt.

$$h_a(\vec{r}_p,t)\approx\frac{k}{R_p}\sum_{i=0}^{N-1}\partial(t-\frac{R_p}{c}-i\Delta t) \tag{4.29}$$

The time between the Dirac pulses and the shape of the excitation determines whether signals from individual elements add or cancel out. If the separation in arrival times corresponds to exactly one or more periods of a sine wave, then they are in phase and add constructively. Thus, peaks in the response are found for

$$n\frac{1}{f} = \frac{D\sin\Theta}{c} \tag{4.30}$$

The main lobe is found for $\Theta = 0$ and the next maximum in the response is found for

$$\Theta = \arcsin(\frac{c}{fD}) = \arcsin(\frac{\lambda}{D}) \tag{4.31}$$

4.4 Imaging with Arrays

Basically there are three different kinds of images acquired by multi-element array transducers, *i.e.* linear, convex, and phased as shown in Figures 4.5, 4.7, and 4.8. The linear array transducer is shown in Fig. 4.5. It selects the region of investigation by firing a set of elements situated over the region. The beam is moved over the imaging region by firing sets of contiguous elements. Focusing in transmit is achieved by delaying the excitation of the individual elements, so an initially concave beam shape is emitted, as shown in Fig. 4.6. The beam can also be focused during reception by delaying and adding responses from the different elements. A continuous focus or several focal zones can be maintained as explained in Section 4.2. Only one focal zone is possible in transmit, but a composite image using a set of foci from several transmissions can be made. Often 4 to 8 zones can be individually placed at selected depths in modern scanners. The frame rate is then lowered by the number of transmit foci.

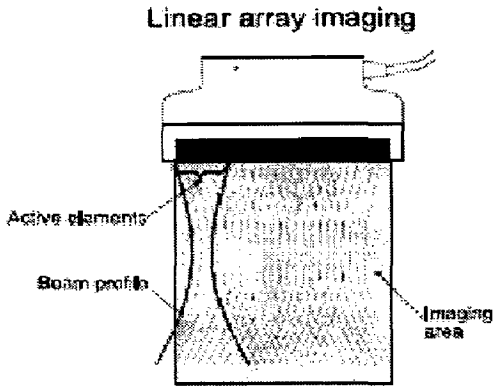

Fig. 4.5: Linear array transducer for obtaining a rectangular cross-sectional image.

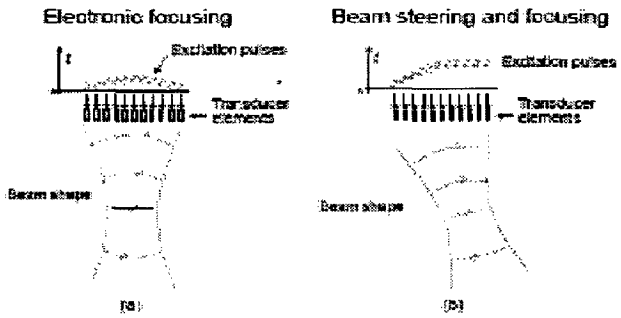

Fig. 4.6: Electronic focusing and steering of an ultrasound beam.

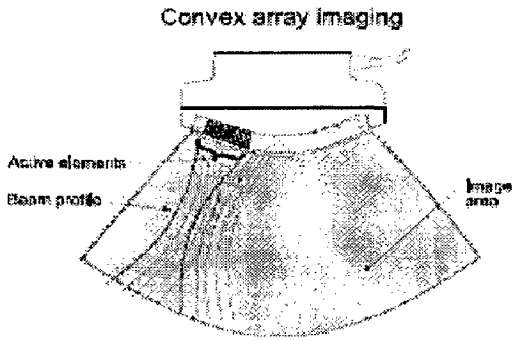

Fig. 4.7: Convex array transducer for obtaining a polar cross-sectional image

The linear arrays acquire a rectangular image, and the arrays can be quite large to cover a sufficient region of interest (ROI). A larger area can be scanned with a smaller array, if the elements are placed on a convex surface as shown in Fig. 4.5. A sector scan is then obtained. The method of focusing and beam sweeping during transmit and receive is the same as for the linear array, and a substantial number of elements (often 128 or 256) is employed.

The convex and linear arrays are often too large to image the heart when probing between the ribs. A small array size can be used and a large field of view attained by using a phased array as shown in Fig. 4.8. All array elements are used here both during transmit and receive. The direction of the beam is steered by electrically delaying the signals to or from the elements, as shown in Fig. 4.6(b). Images can be acquired through a small window and the beam rapidly sweeped over the ROI. The rapid steering of the beam compared to mechanical transducers is of especial importance in flow imaging. This has made the phased array the choice for cardiological investigations through the ribs. More advanced arrays are even being introduced these years with the increase in number of elements and digital beamforming. Especially elevation focusing (out of the imaging plane) is important. A curved surface is used for obtaining the elevation focusing essential for an improved image quality. Electronic beamforming can also be used in the elevation direction by dividing the elements in the elevation direction. The elevation focusing in receive can then be dynamically controlled.

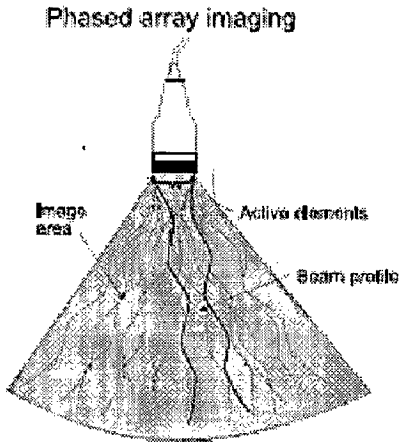

Fig. 4.8. Phased array transducer for obtaining a polar cross-sectional image.

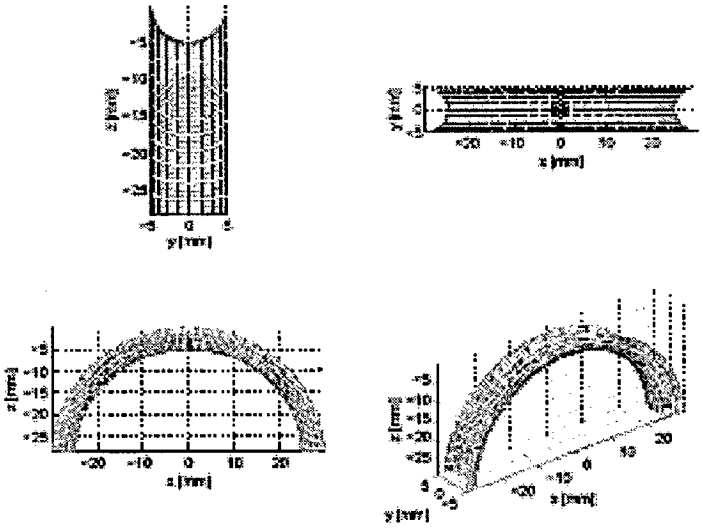

Fig. 4.9: Elevation focused convex array transducer for obtaining a rectangular cross-sectional image, which is focused in the out-of-plane direction. The curvature in the elevation direction is exaggerated in the figure for illustration purposes.

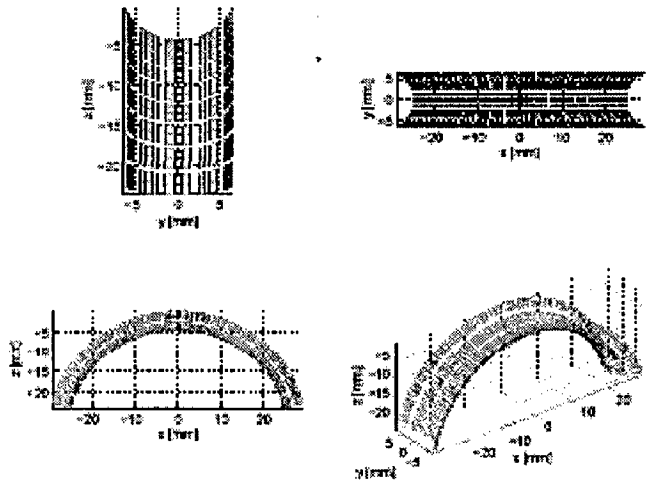

Fig 4.10: Elevation focused convex array transducer with element division in the elevation direction. The curvature in the elevation direction is exaggerated in the figure for illustration purposes

4.5 Simulation of Ultrasound Imaging

One of the first steps in designing an ultrasound system is the selection of the appropriate number of elements for the array transducers and the number of channels for the beamformer. The focusing strategy in terms of number of focal zones and apodization must also be determined. These choices are often not easy, since it is difficult to determine the effect in the resulting images of increasing the number of channels and selecting more or less advanced focusing schemes. It is therefore beneficial to simulate the whole imaging system in order to quantify the image quality.

The simulation is done using Field II program. It runs entirely under the Matlab program. It consist of a Mex file for performing the operations and a set of M-files for calling the different parts of the program. Hereby it is possible to simulate ultrasound systems with advanced dynamic focusing and apodization, *e.g.* phased and linear array imaging and flow imaging. The program has advanced features for dynamic focusing and apodization. The program is fairly new (developed in 2002), and new features are continuously added. It can currently handle round piston, concave, linear and phased arrays, and two-dimensional arrays.

The Field program system uses the concept of spatial impulse responses as developed by Tupholme and Stepanishen in a series of papers [26, 27, 29]. The approach relies on linear systems theory to find the ultrasound field for both the pulsed and continuous wave case. This is done through the spatial impulse response. This response gives the emitted ultrasound field at a specific point in space as function of time, when the transducer is excitated by a Dirac delta function. The field for any kind of excitation can then be found by just convolving the spatial impulse response with the excitation function. The impulse response will vary as a function of position relative to the transducer, hence the name spatial impulse response.

The received response from a small oscillating sphere can be found by acoustic reciprocity. The spatial impulse response equals the received response for a spherical wave emitted by a point. The total received response in pulse-echo can, thus, be found by convolving the

transducer excitation function with the spatial impulse response of the emitting aperture, with the spatial impulse response of the receiving aperture, and then taking into account the electro-mechanical transfer function of the transducer to yield the received voltage trace.

Features of Field II

- Transducer modeled by dividing it into rectangles or triangles.
- C program interfaced to Matlab.
- Matlab used as front-end.
- Can handle any transducer geometry.
- Physical understanding of transducer.
- Pre-defined types: linear and phased arrays, single element concave and flat transducers, and two-dimensional arrays.
- Any focusing, apodization, and excitation pulse.
- Multiple time dependent focusing and apodization.
- Can calculate all types of fields (emitted, received, pulsed, CW)
- Attenuation can be included in the simulation
- Can generate artificial ultrasound images (phased and linear array images with multiple receive and transmit foci).
- Post processing in Matlab

4.5.1 General Algorithm

Step1: The receive and transmit apertures are defined

Transducer parameters are defined to describe the physical dimensions of the transducer. See the figure 4.11 for clarification.

Set initial parameters:

Center frequency (f_o): Center frequency of the transmitted pulse given in MHz.

Sampling frequency (fs): [MHz]

Speed of sound: c=1540 [m/s]

Wavelength: (lambda) =c/f0 [m]

Height: The height of an individual element [mm]

Width: The width of an individual element [mm]

Kerf: The spacing between transducer elements [mm]

N_elements: Number of transducer elements

no_sub_x: Number of sub-divisions in x-direction of elements.

no_sub_y: Number of sub-divisions in y-direction of elements.

Focus: Initial electronic focus, the point in space in front of the transducer face at which the sound field constructively converges. The axes are (lateral, elevation, axial). The center of the transducer face is defined as (0, 0, 0). The axial location is referred to as the *focal depth.*

Transducers are specified by passing it parameters to a subroutine for the particular aperture. The M-function the returns a handle to this particular aperture. Its properties as focusing and apodization is then manipulated through this handle.

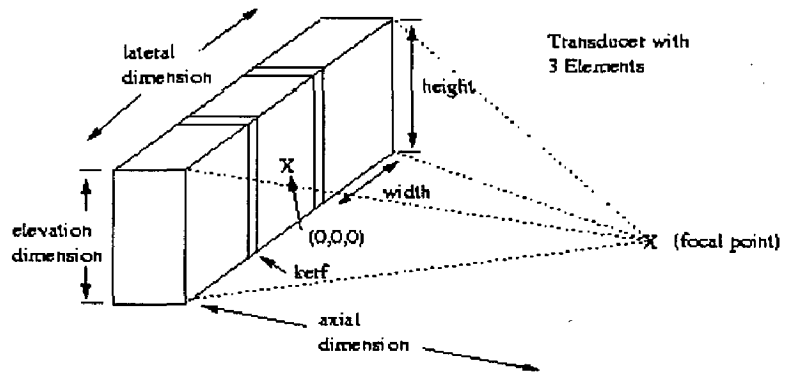

Fig 4.11 Physical dimensions of the transducer

Step2: Setting the excitation waveform

Commands are given for setting the excitation waveform of the transducer and impulse responses are set

Step3: Field calculation

A set of routines is supplied for calculating the different field types. The routines are called with a handle to the apertures involved and the different field points. The spatial impulse responses and their starting times are returned after completion. Thereby different

transducers can be used on the same scatterers and the effect of different choices can readily be evaluated.

Step4: Define a small phantom with scatterers and calculate scattered signal

The computer phantom is generated and a loop is performed for doing the imaging. In this the focus points are set and the apodization is set to use only the elements above the focal point. A linear scan is done by moving the focal point laterally. Then the scattered signal is calculated and stored.

Step5: Plot the Response

Plot the individual element response and summed response of all the transducer elements. Thereby the transducers can be evaluated and images for computer phantoms can be found. A simple target with point scatterers has been defined, and can be used in imaging. A simple example of linear array imaging is shown. Other configurations can easily be defined and it is also possible to simulate flow imaging.

4.5.2. Examples of Transducer Definition

1. A 16 elements linear array, physical elements are divided into 2 by 3 mathematical elements to increase the accuracy of the simulation.

Height of element=5/1000 [m]
Width of element =1/1000 [m]
Distance between transducer elements (kerf)=width/4 [m]
Number of elements=16
Initial electronic focus= [0 0 40]/1000

2. A 16 by 5 elements multirow array, the physical elements are divided into 2 by 3 mathematical elements to increase the accuracy of the simulation.

Height of element = [1 2 3 2 1]/1000 [m]
Width of element = 1.9/1000 [m]

Distance between transducer elements (kerf) = width/5 [m]

Number of elements in x-direction = 16

Number of elements in y-direction = length(heights)

Initial electronic focus = [0 0 70]/1000

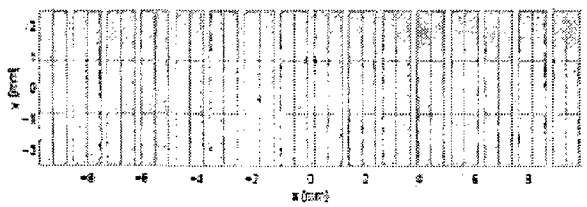

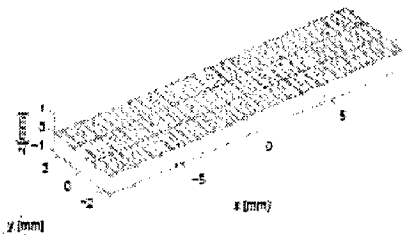

Fig. 4.12(a): Linear array transducer.

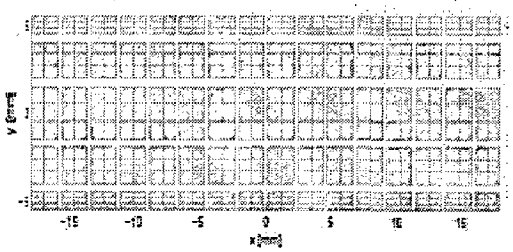

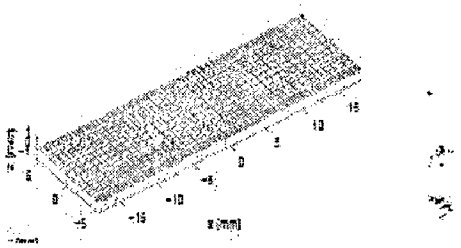

Fig. 4.12(b): Linear array multi-row transducer.

3. A 20 element elevation focused, linear array with an elevation focus at 15 mm:

Height of element = 15/1000 [m]

Width of element = 1.9/1000 [m]

Distance between transducer elements kerf=width/3 [m]

Number of elements = 20

Elevation focus = 15/1000 [m]

Initial electronic focus = [0 0 70]/1000

4. A concave, round transducer with an 8 mm radius and a focal radius of 20 mm and divided into 1 mm mathematical elements.

Radius of transducer = 8/1000

Focal radius of transducer = 20/1000

Size of mathematical elements = 1/1000

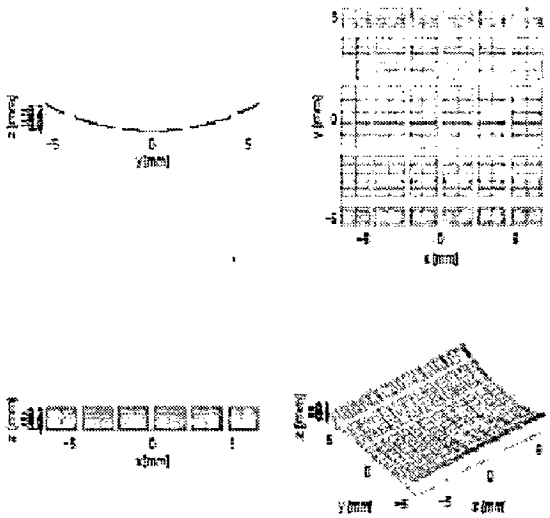

Fig. 4.12(c): Linear array multi-row transducer for elevation focused.

5. A 16 element convex array with a convex radius of 20 mm:

Height of element =5/1000; [m]

Width of element = 1/1000 [m]

Distance between transducer elements kerf=width/4 [m]

Number of elements = 16

Convex radius = 20/1000 [m]

Initial electronic focus = [0 0 40]/1000

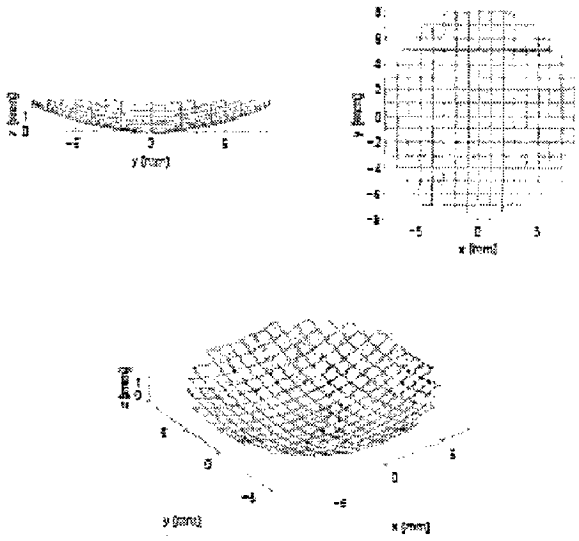

Fig 4.12(d) Concave, round transducer

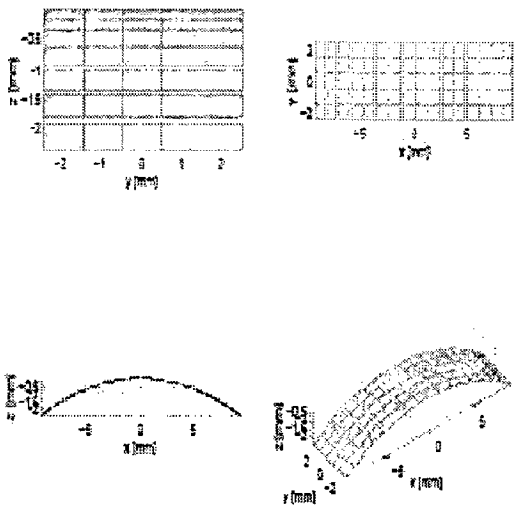

Fig 4.12(e) Rectangles for a convex array

6. A 20 element elevation focused, convex array with 5 rows. The elevation focus is at 10 mm and the convex radius is 30 mm:

Height of element = [1 2 3 2 1]/1000 [m]
Width of element = 3/1000 [m]
Distance between transducer elements = width/3 [m]
Distance between transducer elements = 1/1000 [m]
Number of elements in x-direction = 20
Convex radius = 30/1000 [m]
Elevation focus = 7/1000 [m]
Initial electronic focus = [0 0 70]/1000 [m]

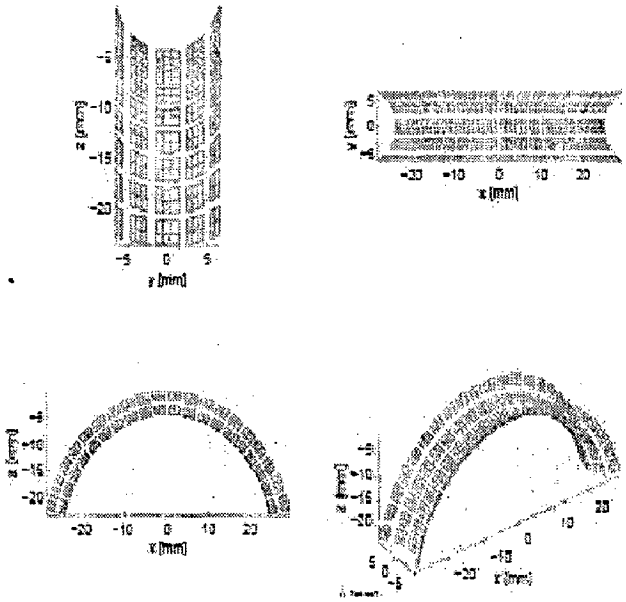

Fig 4.12(f) Rectangles for an elevation focused multi row convex array

7. A fully populated two-dimensional array with 11 by 13 elements:

Height of element = 1.5/1000 [m]
Width of element = 1/1000 [m]
Distance between transducer elements = width/5 [m]
Distance between transducer elements = height/2 [m]

Number of elements in x-direction = 11

Number of elements in y-direction = 13

Initial electronic focus [m] = [0 0 60]/1000

8. A sparsely populated two-dimensional array arranged in the form of a cross:

Find which elements to use

enabled(:,7)=ones(no_ele_x,1);

enabled(6,:)=ones(1,no_ele_y);

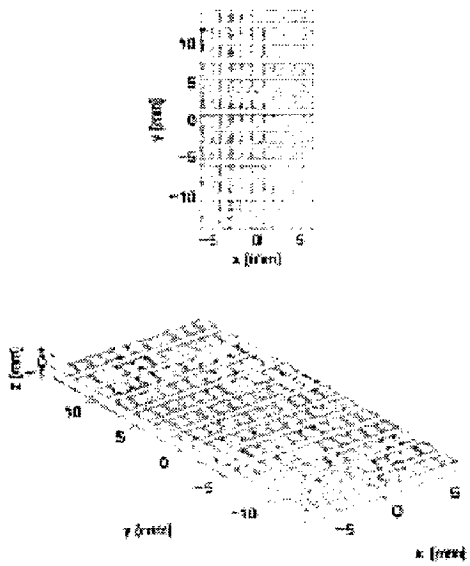

Fig 4.12(g) Fully populated 2D array

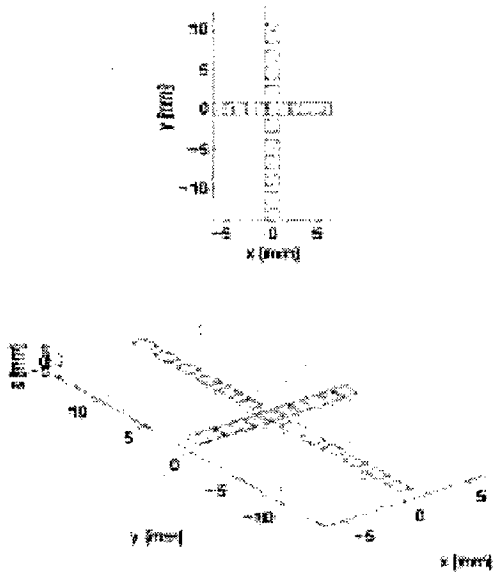

Fig 4.12(h)) Partially populated 2D array

4.5.3 Simulated Results for the Received Response

Fig. 4.13 (a): Received response from the 16 elements transducer defined in **Fig. 4.12 (a):** with target scatterers placed at [0,0,40]

Fig. 4.13 (b): Received response from the 32 elements transducer defined in **Fig. 4.12 (a):** with target scatterers placed at [0,0,20]

Fig. 4.13 (c): Received response from the 16 elements transducer defined in **Fig. 4.12 (c):** with target scatterers placed at [0,0,40]

Fig. 4.13 (d): Received response from the 32 elements transducer similar to 16 element transducer defined in **Fig. 4.12 (c):** with target scatterers placed at [0,0,20]

Fig. 4.13 (e): Received response from the 16 elements transducer defined in **Fig. 4.12 (f):** with target scatterers placed at [0,0,40]

Fig. 4.13 (f): Received response from the transducer defined in **Fig. 4.12 (h):** with target scatterers placed at [0,0,20]

Results

Received voltage traces from the individual elements of array transducer

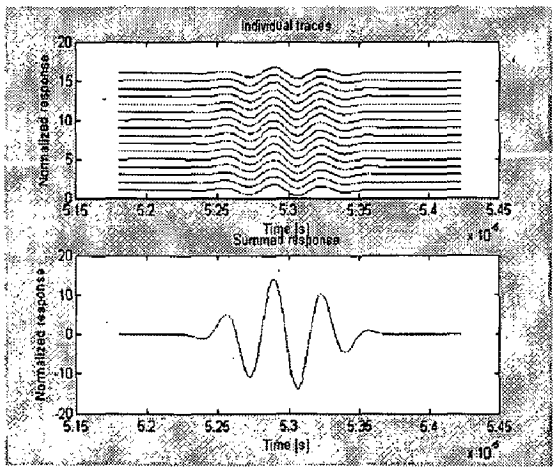

Fig. 4.13 (a)

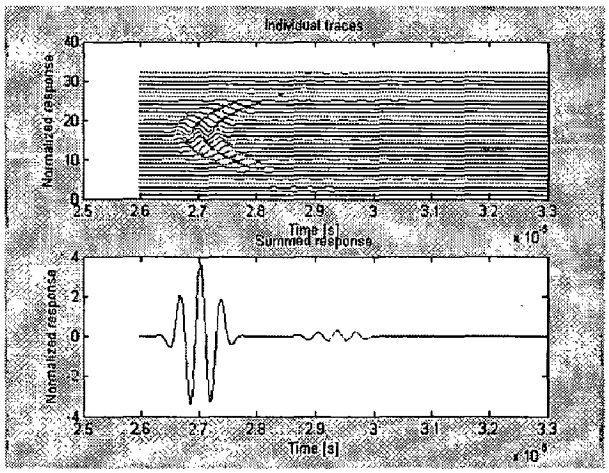

Fig. 4.13 (b)

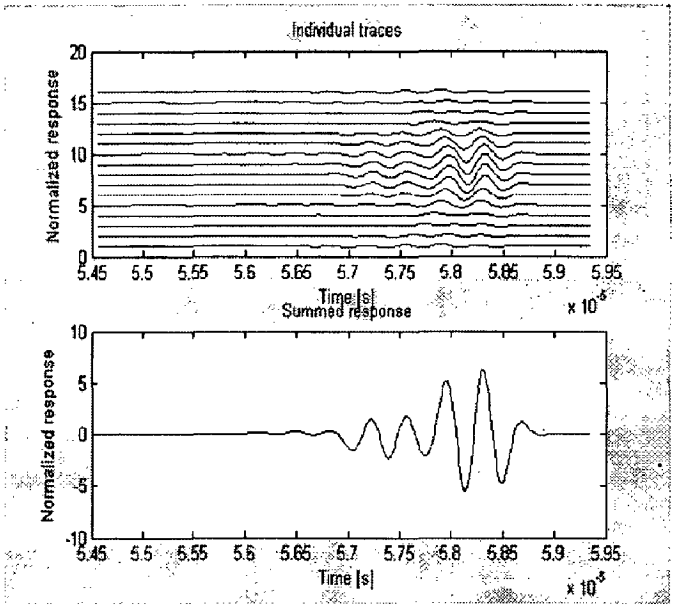

Fig. 4.13 (c)

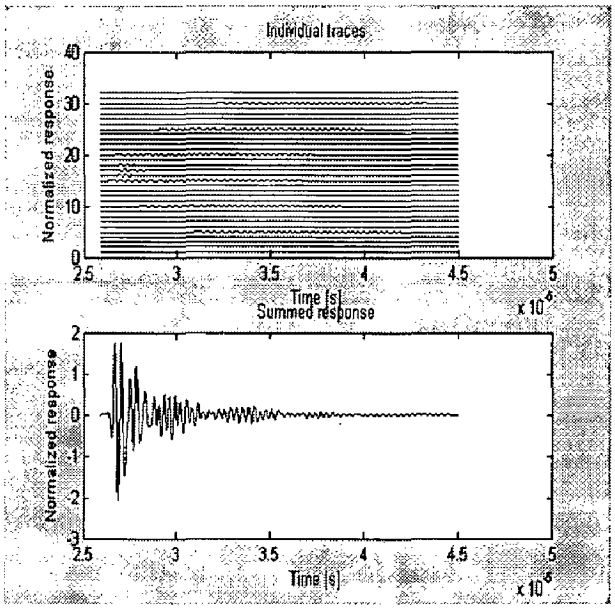

Figure 4.13 (d)

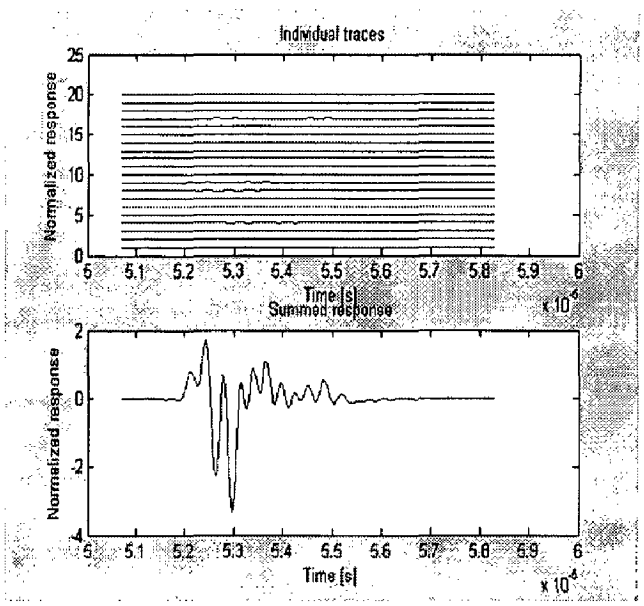

Fig. 4.13 (e)

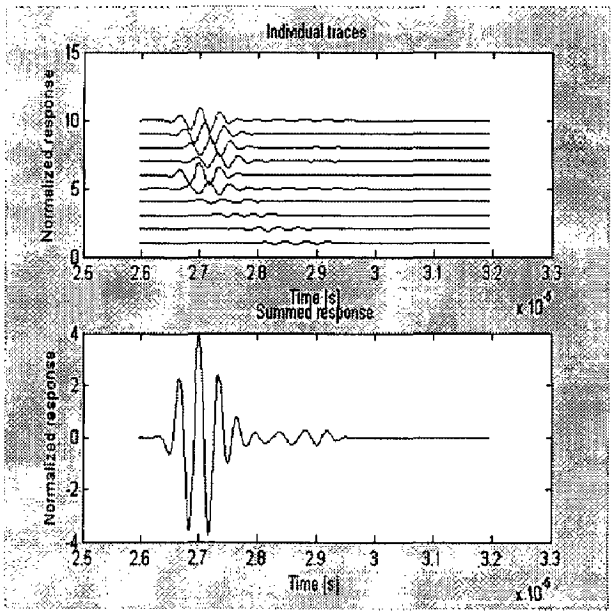

Fig. 4.13 (f)

Fig 4.13(g) Simulated results for received response from all elements of a linear array with 3 transmitting and 16 receiving elements and plot the responses and the summed response

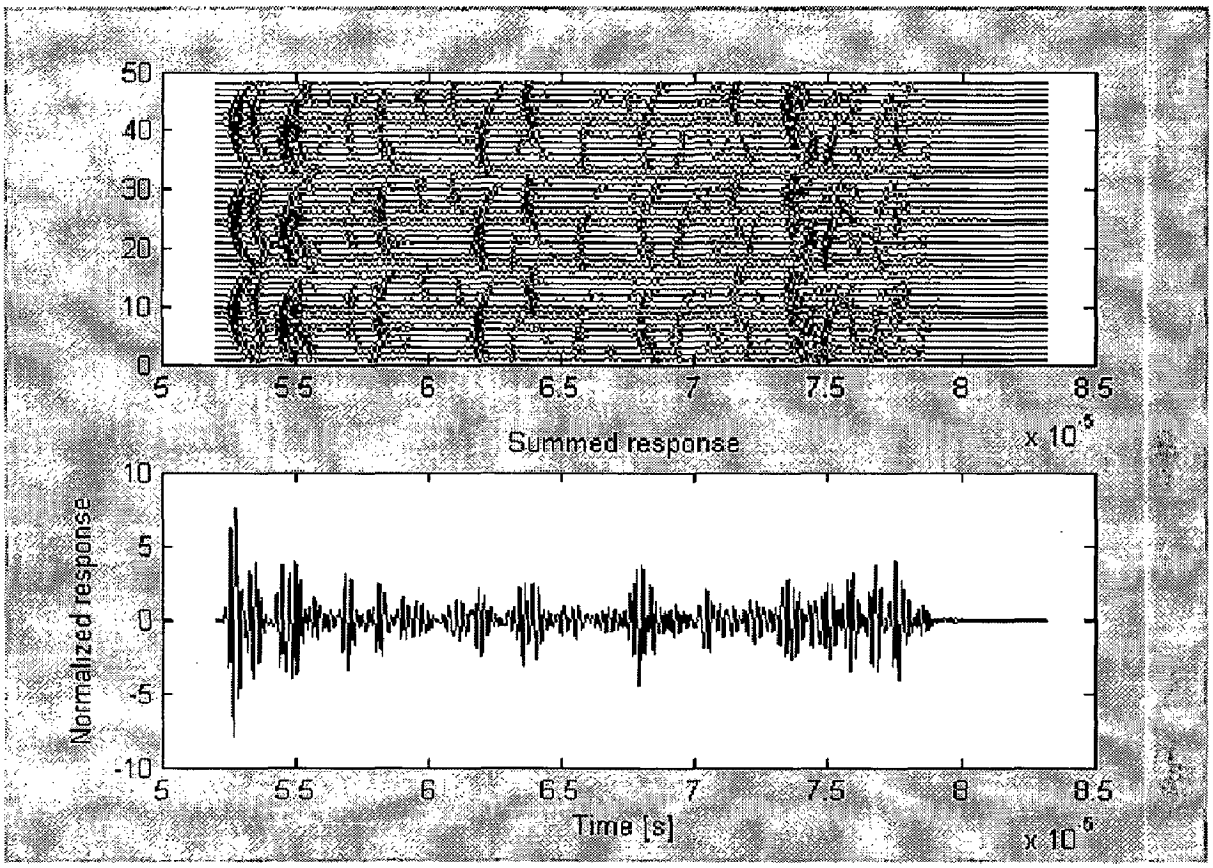

Fig. 4.13 (g) Received voltage traces from the individual elements of a 16 elements linear array transducer, when transmitting with three different elements.

The program Field II makes it possible to simulate the whole imaging process with time varying focusing and apodization as described in [33] and [16]. This has paved the way for doing realistic simulated imaging with multiple focal zones for transmission and reception and for using dynamic apodization. It is hereby possible to simulate ultrasound imaging for all image types including flow images.

CHAPTER 5

SIMULATION OF ULTRASOUND IMAGES OF BIOLOGICAL TISSUES

5.1 Simulation Model

The first simple treatment of ultrasound is often based on the reflection and transmission of plane waves. It is assumed that the propagating wave impinges on plane boundaries between tissues with different mean acoustic properties. Such boundaries are rarely found in the human body, and seldom show on ultrasound images. This is demonstrated by the image shown in Fig. 5.1. Here the skull of the fetus is not clearly marked. It is quite obvious that there is a clear boundary between the fetus and the surrounding amniotic fluid. The skull boundary is not visible in the image, because the angle between the beam and the boundary has a value such that the sound bounces off in another direction, and, therefore, does not reach the transducer. Despite this, the extent of the head can still be seen. This is due to the scattering of the ultrasound wave. Small changes in density, compressibility, and absorption give rise to a scattered wave radiating in all directions. The backscattered field is received by the transducer and displayed on the screen. One might well argue that scattering is what makes ultrasound images useful for diagnostic purposes, and it is, as will be seen later, the physical phenomena that makes detection of blood velocities possible. Ultrasound scanners are, in fact, optimized to show the backscattered signal, which is considerably weaker than that found from reflecting boundaries. Such reflections will usually be displayed as bright white on the screen, and can potentially saturate the receiving circuits in the scanner. An example can be seen at the neck of the fetus, where a structure is perpendicular to the beam. This strong reflection saturates the input amplifier of this scanner. Typical boundary reflections are encountered from the diaphragm, blood vessel walls, and organ boundaries.

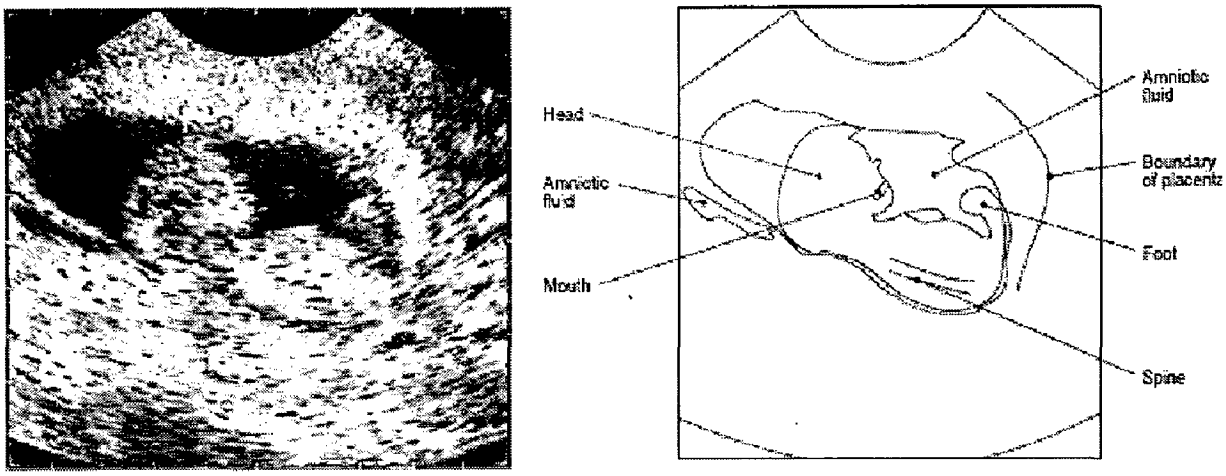

Fig. 5.1: Ultrasound image of a 13th week fetus. The markers at the border of the image indicate one centimeter

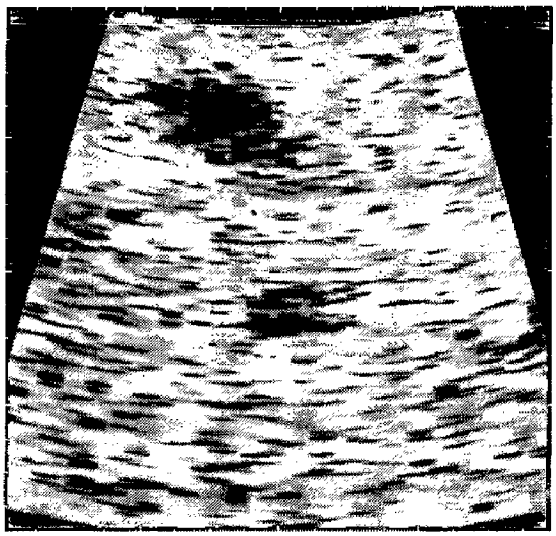

Fig. 5.2: 4 X 4 cm image of a human liver from a healthy 28-year-old man. The completely dark areas are blood vessels

An enlarged view of an image of a liver is seen in Fig 5.2. The image has a grainy appearance, and not a homogeneous gray or black level as might be expected from homogeneous liver tissue. This type of pattern is called speckle. The displayed signals are the backscatter from the liver tissue, and are due to connective tissue, cells, and fibrous tissue in the liver. These structures are much smaller than one wavelength of the

ultrasound, and the speckle pattern displayed does not directly reveal physical structure. It is rather the constructive and destructive interference of scattered signals from all the small structures. So it is not possible to visualize and diagnose microstructure, but the strength of the signal is an indication of pathology. A strong signal from liver tissue, making a bright image, is, *e.g.*, an indication of a fatty or cirrhotic liver.

As the scattered wave emanates from numerous contributors, it is appropriate to characterize it in statistical terms. The amplitude distribution follows a Gaussian distribution [34], and is, thus, fully characterized by its mean and variance. The mean value is zero since the scattered signal is generated by differences in the tissue from the mean acoustic properties.

Although the backscattered signal is characterized in statistical terms, one should be careful not to interpret the signal as random in the sense that a new set of values is generated for each measurement. The same signal will result, when a transducer is probing the same structure, if the structure is stationary. Even a slight shift in position will yield a backscattered signal correlated with that from the adjacent position. The shift over which the signals are correlated is essentially dependent on the extent of the ultrasound field. This can also be seen from the image in Fig. 5.2, as the laterally elongated white speckles in the image indicate transverse correlation. The extent of these speckle spots is a rough indication of the point spread function of the system.

The correlation between different measurements is what makes it possible to estimate blood velocities with ultrasound. As there is a strong correlation for small movements, it is possible to detect shifts in position by comparing or, more strictly, correlating successive measurements of moving structure, *e.g.*, blood cells.

Since the backscattered signal depends on the constructive and destructive interference of waves from numerous small tissue structures, it is not meaningful to talk about the reflection strength of the individual structures. Rather, it is the deviations within the tissue and the composition of the tissue that determine the strength of the returned signal. The

magnitude of the returned signal is, therefore, described in terms of the power of the scattered signal. Since the small structures reradiate waves in all directions and the scattering structures might be ordered in some direction, the returned power will, in general, be dependent on the relative position between the ultrasound emitter and receiver. Such a medium is called anisotropic, examples of which are muscle and kidney tissue. By comparison, liver tissue is a fairly isotropic scattering medium, when its major vessels are excluded, and so is blood. It is, thus, important that the simulation approach models the scattering mechanisms in the tissue. This is essentially what the model derived in Chapter 3 does. Here the received signal from the transducer is:

$$p_r(\vec{r},t) = v_{pe} \underset{t}{*} f_m(\vec{r}) \underset{r}{*} h_{pe}(\vec{r},t) \tag{5.1}$$

where $\underset{r}{*}$ denotes spatial convolution. v_{pe} is the pulse-echo impulse, which includes the transducer excitation and the electro-mechanical impulse response during emission and reception of the pulse. f_m accounts for the inhomogeneities in the tissue due to density and propagation velocity perturbations which give rise to the scattered signal. h_{pe} is the pulse-echo spatial impulse response that relates the transducer geometry to the spatial extent of the scattered field. Explicitly written out these terms are:

$$v_{pe}(t) = \frac{p}{2c^2} E_m(t) \underset{t}{*} \frac{\partial v^3 t}{\partial t^3} \tag{5.2}$$

$$f_m(\vec{r}) = \frac{\Delta\rho(\vec{r})}{\rho} - \frac{2\Delta c(\vec{r})}{c} \tag{5.3}$$

$$h_{pe}(\vec{r},t) = h_p(\vec{r},t) * h_e(\vec{r},t) \tag{5.4}$$

So the received response can be calculated by finding the spatial impulse response for the transmitting and receiving transducer and then convolving with the impulse response of the transducer. A single RF line in an image can be calculated by summing the response from a collection of scatterers in which the scattering strength is determined by the density and speed of sound perturbations in the tissue. Homogeneous tissue can thus be made from a collection of randomly placed scatterers with a scattering strength with a Gaussian

distribution, where the variance of the distribution is determined by the backscattering cross-section of the particular tissue. This is the approach taken in this dissertation work.

The simulation of ultrasound imaging using linear acoustics has been extensively used for studying focusing, image formation, and flow estimation, and it has become a standard tool in ultrasound research.

The main part of an ultrasound image consists of a speckle pattern, which emanates from the signal generated by tissue cells, connective tissue, and in general all small perturbations in speed of sound, density, and attenuation. The generation of this can be modeled as the signal from a large collection of randomly placed point scatterers with a Gaussian amplitude. Larger structures as vessel or organ boundaries can be modeled as a deterministically placed set of point scatterers with a deterministic amplitude. The relative amplitude between the different scatterers is then determined by a scatterer map of the structures to be scanned. Such maps can be based on either optical, CT or MR images, or on parametric models of the organs. Currently the most realistic images are based on optical images of the anatomy. Blood flow can also be modeled by this method. The red blood cells, mainly responsible for the scattering, can be modeled as point scatterers and the flow of the blood can be simulated using either a parametric flow model or through finite element modeling. The received signal is then calculated, and the scatterers are propagated between flow emissions. The simulation of all linear ultrasound systems can, thus, be done by finding the summed signal from a collection of point scatterers. The random selection of point scatterers should consist of atleast 10 scatterers per resolution cell to generate fully developed speckle, and for a normal ultrasound image this results in 200,000 to 1 million scatterers.

In imaging the same spatial impulse response is calculated for each of the image lines, and making 128 lines, thus, gives 128 calculations of the same impulse response delayed differently for the different lines. Doing the focusing after this point in the simulation can make the calculation faster. This corresponds to full synthetic aperture imaging. The received response from each element is calculated, when emitting with each of the

elements in the aperture, and then the responses are subsequently focused. This is the approach taken in this dissertation work using a modified version of the Field II program.

The computer phantoms typically consist of 100,000 or more discrete scatterers, and simulating 50 to 128 RF lines can take few hours depending on the computer used. It is therefore beneficial to split the simulation into concurrently run sessions. This can easily be done by first generating the scatterer's position and amplitude and then storing them in a file. This file can then the be used by a number of workstations to find the RF signal for different imaging directions, which are then stored in separate files; one for each RF line. These files are then used to assemble an image. This is the approach used for the simulations shown here in which Pentium 4; 2.5 MHz PC can generate one phantom image using Matlab 7 and the Field II program.

5.2 Anatomic phantoms

The anatomic phantoms are attempts to generate images as they will be seen from real human subjects. This is done by drawing a bitmap image of scattering strength of the region of interest. This map then determines the factor multiplied onto the scattering amplitude generated from the Gaussian distribution, and models the difference in the density and speed of sound perturbations in the tissue. Simulated boundaries were introduced by making lines in the scatterer map along which the strong scatterers were placed. This is marked by completely white lines shown in the scatterer maps. The model is currently two-dimensional, but can readily be expanded to three dimensions.

In this dissertation work two different phantoms have been made; a *fetus* in the third month of development and a left *kidney* in a longitudinal scan.

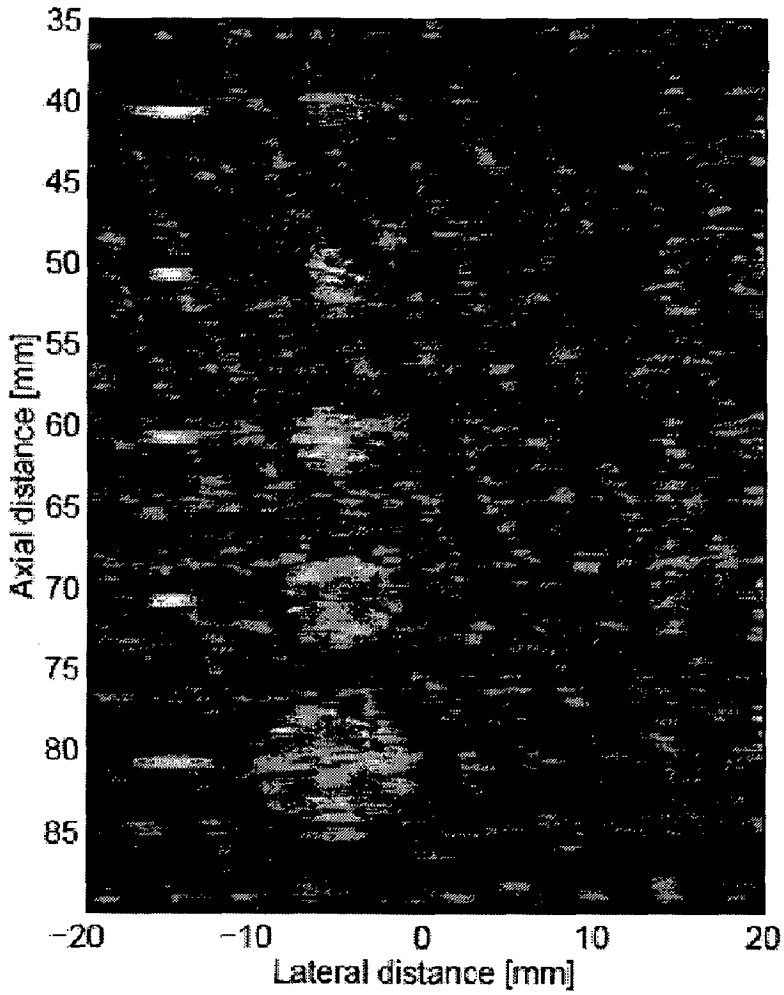

Fig. 5.3: Computer phantom with point targets, cyst regions, and strongly reflecting regions.

5.3 General Algorithm for generation of Images

1. Start up the Field simulation system.
2. Create the phantom for a fetus.
   I. Define image coordinates.
   II. Load input baby map.
   III. Find the white structures and generate data for them.
   IV. Calculate position data.
   V. Amplitudes with different variance are generated according to the input map. The amplitude of the fetus image is used to scale the variance.

VI. Include the strong scatterers.

3. Perform Simulation and store the data in mat files; one for each rf-line.
4. Make an image from simulated data
   I. Read the data for the scatteres from the mat file.
   II. Adjust the data in time and display it as a gray scale image.

5.4 Calculation of B-mode image of synthetic fetus

A phantom for a 3 month old fetus has been made. 200,000 scatterers were randomly distributed within the phantom, and with a Gaussian distributed scatter amplitude with a standard deviation determined by the scatter map. The phantom was scanned with a 5 MHz 64 element phased array transducer with lambda/2 spacing and Hanning apodization. A single transmit focus 70 mm from the transducer was used, and focusing during reception is at 40 to 140 mm in 10 mm increments. The images consists of 128 lines with 0.7 degrees between lines.

The fetus image is shown below. Note how the anatomy can be clearly seen at the level of detail of the scatterer map.

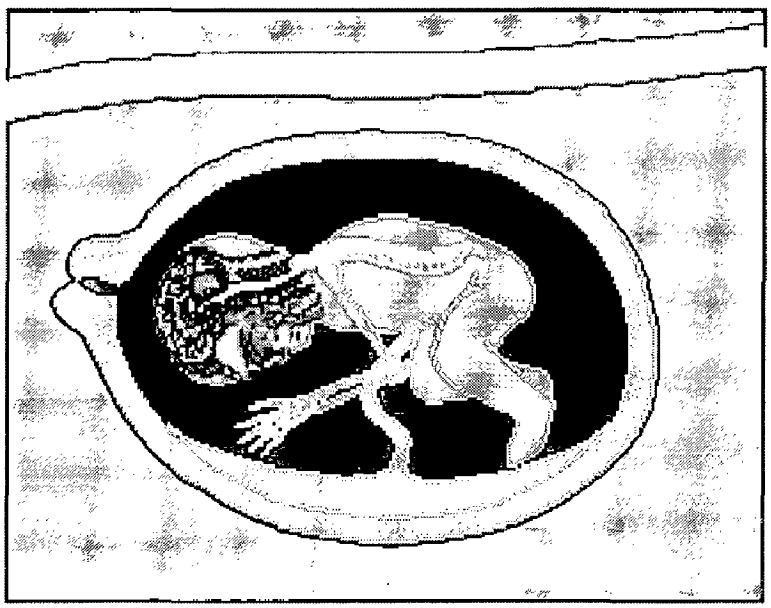

Fig 5.4 (a) Fetus Scatter Map

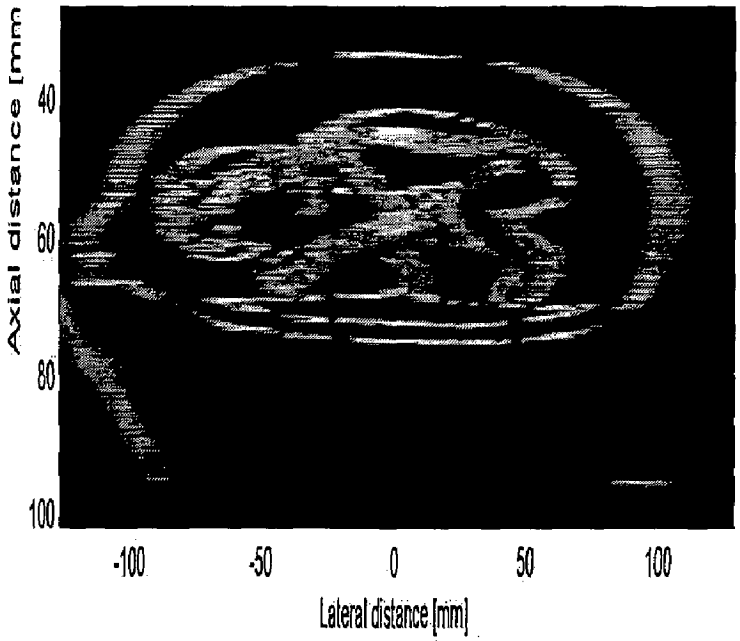

Fig 5.4(b) Simulated Fetus Image

The images have many of the features from real scan images, but still lack details. This can be ascribed to the low level of details in the bitmap images, and that only a 2D model is used. But the images do show great potential for making powerful fully synthetic phantoms that can be used for image quality evaluation.

5.5 Calculation of B-mode image of synthetic kidney

A phantom for a left kidney in a longitudinal scan has been made. 200,000 scatterers were randomly distributed within the phantom, and with a Gaussian distributed scatter amplitude with a standard deviation determined by the scatter map. The phantom was scanned with a 5 MHz 64 element phased array transducer with lambda/2 spacing and Hanning apodization. A single transmit focus 70 mm from the transducer was used, and focusing during reception is at 40 to 140 mm in 10 mm increments. The image consists of 128 lines with 0.7 degrees between lines.

Below is shown the artificial kidney scatterer map

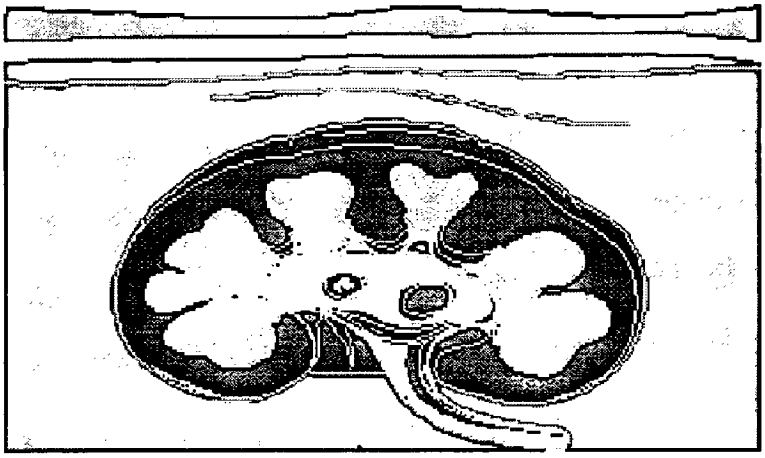

Fig 5.5 (a) Kidney Scatter Map

The simulated resulting image is shown below. Note the bright regions where the boundary of the kidney is orthogonal to the ultrasound, and thus a large signal is received. Note also the fuzziness of the boundary, where they are parallel with the ultrasound beam, which is also seen on actual ultrasound scans.

Results

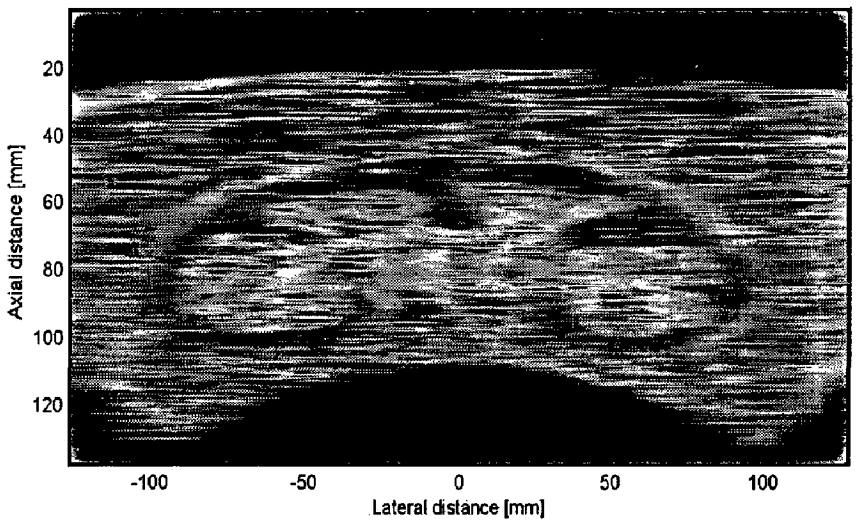

Fig 5.4(b) Simulated Kidney's Image

CHAPTER 6

ULTRASOUND SIMULATION FOR FLOW ESTIMATION

Medical ultrasound scanners can be used for both displaying gray-scale images of the anatomy and for visualizing the blood flow dynamically in the body. The systems can interrogate the flow at a single position in the body and there find the velocity distribution over time. They can also show a dynamic color image of velocity at up to 20 to 60 frames a second. Both measurements are performed by repeatedly pulsing in the same direction and then use the correlation from pulse to pulse to determine the velocity. This chapter gives a simple model for the interaction between the ultrasound and the moving blood. The calculation of the velocity distribution is then explained along with the different physical effects influencing the estimation. The estimation of mean velocities using auto- and cross-correlation for color flow mapping is also described. Finally the simulations of these flow systems using spatial impulse responses are described.

6.1 Introduction

It is possible with modern ultrasound scanners to visualize the blood flow at either one sample volume in the body or over a cross-sectional region. The first approach gives a display of the velocity distribution at the point as a function of time. The second method gives a color flow image superimposed on the gray-scale anatomic image. The color coding shows the velocity towards or away from the transducer, and this can be shown with up to 20 images a second. Thus, the dynamics of the blood flow in e.g. the vessel and heart and across heart valves can be diagnosed.

The history of ultrasound velocity measurement dates back to the mid 1950ties, where experiments by Satomura [36], [37] in Japan demonstrated that continuous wave (CW) ultrasound was capable of detecting motion. CW ultrasound cannot locate the depth of the motion and several pulsed wave solutions where therefore made by Baker [38], Peronneau

and Leger [39], and Wells [40] around 1970. These systems could detect the motion at a specific location. The Baker system could show the velocity distribution over time and across the vessel lumen. This was later extended by Kasai and co-workers [41], [42] to generate actual cross-sectional images of velocity in real time. They used an autocorrelation velocity estimator adapted from radar to find the mean velocity from only 8 to 16 pulse-echo lines. Color flow mapping systems using a cross-correlation estimator was also suggested by Bonnefous and co-workers [43]. From these early experimental systems the scanners have now evolved into systems for routine use in nearly all hospitals, and ultrasound is one of the most common means of diagnosing hemodynamic problems today.

This chapter will give a brief description of the main features of all these systems. The chapter starts by deriving a basic model for ultrasound's interaction with a point scatterer, which shows that the frequency of the received sampled signal is proportional to velocity. Systems for finding the velocity distribution in a vessel are then described and finally the newest color flow mapping method are explained. A more comprehensive treatment of the systems can be found in [4].

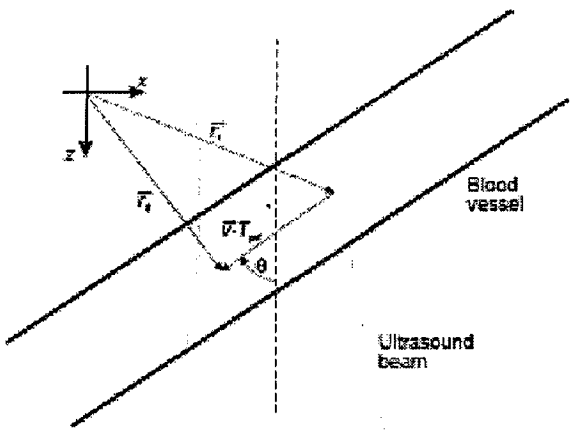

Fig. 6.1: Coordinate system for finding the movement of blood particles

6.2 Measurement of Flow Signals

The data for the velocity measurement is obtained by emitting a short ultrasound pulse with 4 to 8 cycles at a frequency of 2 to 10 MHz. The ultrasound is then scattered in all directions by the blood particles and part of the scattered signal is received by the transducer and converted to a voltage signal. The blood velocity is found through the repeated measurement at a particular location. The blood particles will then pass through the measurement gate and give rise to a signal with a frequency proportional to velocity.

A coordinate system for the measurement is show in Fig. 6.1 The vector $\vec{r}_1$ indicates the position for one scatterer, when the first ultrasound pulse interacts with the scatterer. The vector $\vec{r}_2$ indicates the position for interaction with the next ultrasound pulse emitted Tprf seconds later. The movement of the scatterer in the z-direction away from the transducer in the time interval between the two pulses is

$$D_z = |\vec{r}_2 - \vec{r}_1|\cos(\theta) = |\vec{v}|\cos(\theta)T_{prf} \tag{6.1}$$

where θ is the angle between the ultrasound beam and the particle's velocity vector v. The traveled distance gives rise to a delay in the second signal compared to the first. Denoting the first received signal as $\vec{r}_1$ (t) and the second as $\vec{r}_2$ (t) gives

$$r_1(t) = r_2(t - t_s),$$

$$t_s = \frac{2D_z}{c} = \frac{2|\vec{v}|\cos\theta}{c}T_{prf} = \frac{2v_z}{c}T_{prf} \tag{6.2}$$

where c is the speed of sound. Emitting a sinusoidal pulse p(t) with a frequency of f_0 gives a received signal of

$$p(t) = g(t)\sin(2\pi f_0 t)$$

$$r_1(t) = p(t - t_0)$$

$$t_0 = \frac{2d}{c} \tag{6.3}$$

where d is the depth of interrogation, and g(t) is the envelope of the pulse. Repeating the measurement a number of times gives a received, sampled signal for a fixed depth of

$$r_i(t) = p(t - t_0 - it_s)$$
$$= g(t - t_0 - it_s)\sin(2\pi f_0 t - t_0 - it_s) \qquad (6.4)$$

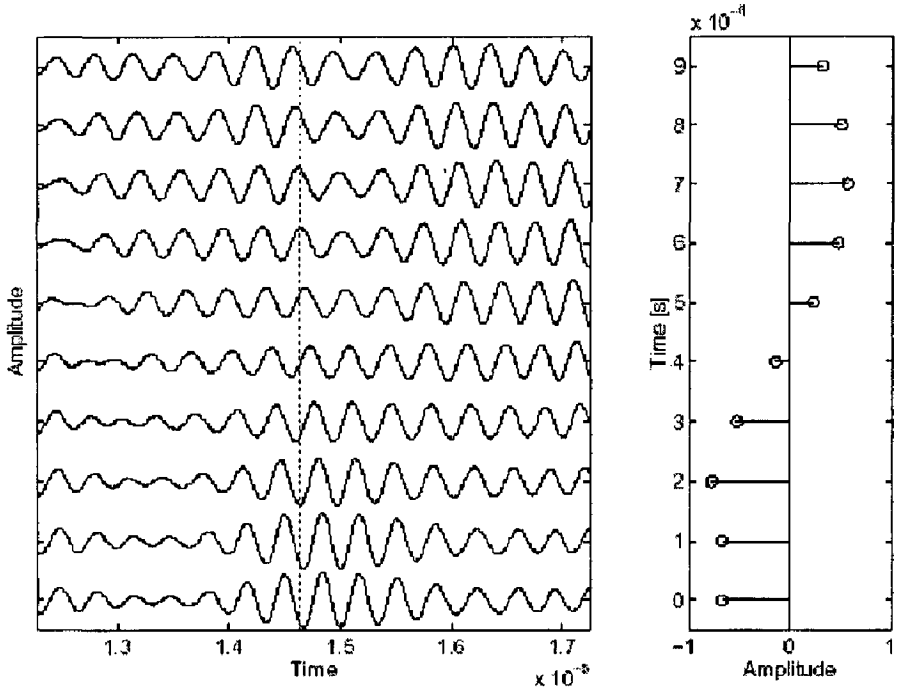

Fig. 6.2: RF sampling of simulated signal from blood vessel. The left graph shows the different received RF lines, and the right graph is the sampled signal. The dotted line indicates the time when samples are acquired

Here t is time relative to the pulse emission. Taking the measurement at the same time tx relative to the pulse emission corresponding to a fixed depth in tissue gives

$$r_i(t_x) = g(t_x - t_0 - it_s)\sin(2\pi f_0(t_x - t_0 - it_s))$$
$$= a\sin(-2\pi f_0 it_s + \Theta_x)$$
$$\Theta_x = 2\pi f_0(t_x - t_0) \qquad (6.5)$$

assuming the measurement is taken at times when the envelope g(t) of the pulse is constant. Such a measurement will yield one sample for each pulse-echo RF line, and thus samples the slow movement of the blood scatterers past the measurement position or range gate as shown in Fig.6.2 The sampled signal r(t) can be written as:

$$r(i) = \sin\left(-2\pi \frac{2v_z}{c} f_0 i T_{prf} + \Theta_x\right) \tag{6.6}$$

showing that the frequency of this signal is:

$$f_p = \frac{2v_z}{c} f_0 \tag{6.7}$$

which is proportional to the projected velocity of the blood in the direction of the ultrasound beam.

The received signal will not only consist of a single frequency, since an ultrasound pulse is emitted and received. This pulse will be sampled, when it moves past the range gate, and the corresponding digital signal will thus have a spectrum determined by the pulse shape. The frequency axis of the pulse spectrum will also be multiplied by the 2vz/c factor due to the sampling operation. An example is shown in Fig. 6.3. The spectrum of the RF pulse is shown on the top, and the resulting frequency axis for the received digital signal is shown on the bottom.

This simple model can also be used for determining the effect of velocity aliasing, limited observation time, attenuation, and non-linear propagation. The signal must be sampled according to the Nyquist limit, so that frequency components in the spectrum are below half the sampling frequency. Here it is $f_{prf} = 1/T_{prf}$, and the maximum velocity, that can be measured, is determined by:

$$f_{prf}/2 > 2\frac{v_{max}}{c} f_0 \tag{6.8}$$

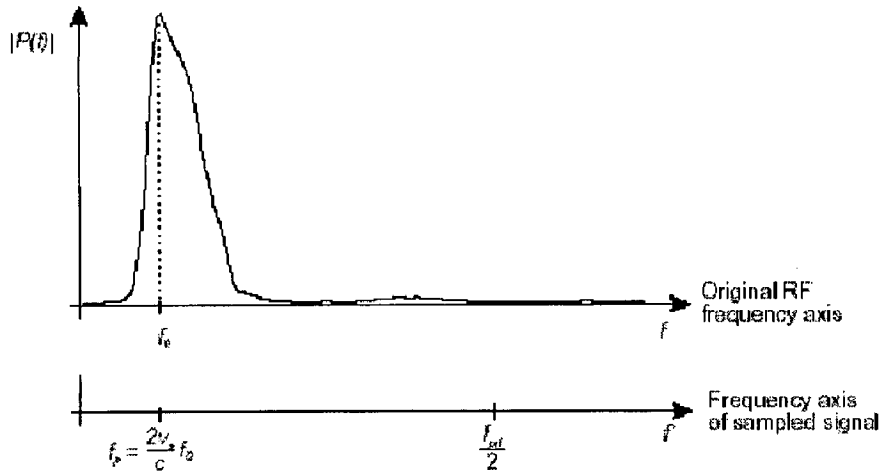

Fig. 6.3: Frequency scaling of the received RF signal from the sampling for a number of pulse-echo lines

Note here that the sampling frequency is in the kilohertz range, and that the ultrasound frequency is in the mega-hertz range, which does no seem to make sense. It should, however, be kept in mind, that it is not the RF information that is sampled, but rather the slow movement of the blood scatterers past the range gate.

Obtaining only a limited number of pulse-echo lines will truncate the digital version of the measurement pulse. This corresponds to multiplication with a rectangular window, and the resulting spectrum is convolved with the Fourier transform of the window leading to a broadening of the spectrum.

Ultrasound propagating in tissue is attenuated due to scattering and absorption. The attenuation is proportional to depth and frequency and is typically in the range from 0.5 to 1 dB/[MHz cm]. This will for a pulsed system lead to a loss of signal energy and to a decrease in center frequency of the pulse field. Often a shift in frequency of 100 - 200 kHz can be experienced on a 5 MHz pulse. The shift is relative to the pulse center frequency, and is, thus, multiplied with the scaling factor $2v_z/c$ giving rise to only a minor shift in the measured frequency for the sampled signal. This is also the case for non-linear propagation and scattering effects, which then also scale proportionally to the velocity. The multi pulse

measurement technique is, thus, very robust to the different physical effects encountered in medical ultrasound, and is therefore preferred to finding the Doppler shift of the pulse spectrum during the interaction with the moving scatterer.

The velocity can be both towards and away from the transducer, and this should also be included in the estimation of velocity. The sign can be found by using a pulse with a one-sided spectrum corresponding to a complex signal with a Hilbert transform relation between the imaginary and real part of the signal. The one sided spectrum is then scaled by $2v_z/c$ and has a unique peak in the spectrum from which the velocity can be found. The complex signal can be made by Hilbert transforming the received signal and using this for the imaginary part of the signal.

A Hilbert transform is difficult to make with analog electronics and two other implementations are shown in Fig. 6.4. The top graphs makes the demodulation by a complex multiplication with exp($j2\pi f0t$) and then lowpass filtration for removing the peak in the spectrum at 2f0. Matching the bandwidth of the low-pass filters to the bandwidth of the pulse also gives an improvement in signal-to-noise ratio. The second solution obtains the signal by quadrature sampling with a quarter wave delay between the two channels. Both implementations gives complex signals that can readily be used in the estimators for determining the velocity with a correct sign [4].

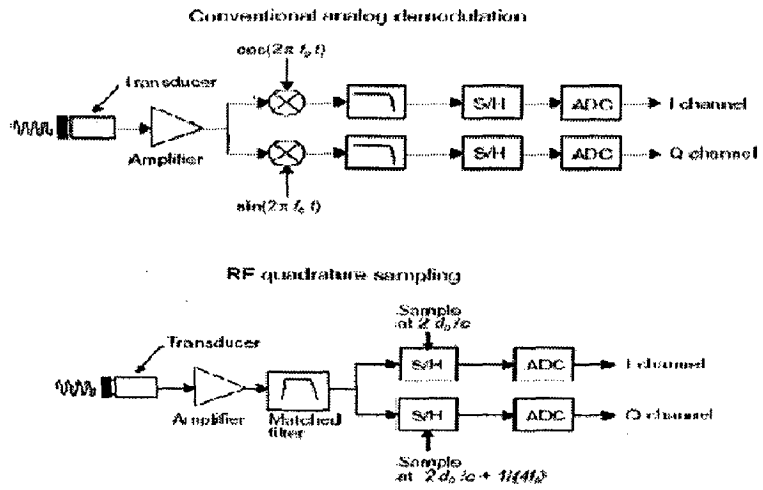

Figure 6.4: Demodulation schemes for obtaining a complex signal for determining the sign of the velocity

6.3 Calculation and Display of the Velocity Distribution

Using a number of pulse-echo lines and sampling at the depth of interest, thus, gives a digital signal with a frequency proportional to velocity. Having a movement of a collection of scatterers with different velocities then gives a superposition of the contribution from the individual scatterers and gives rise to a spectral density of the signal equal to the density of the velocities.

Typical profiles for a stationary laminar flow are given by:

$$v_r = v_0\left[1-\left(\frac{r}{R}\right)^{p_0}\right] \tag{6.9}$$

where r is radial distance, R is the radius of the vessel, v_0 is the maximum velocity at the center of the vessel and p_0 is an integer. Under uniform insonation of the vessel, the frequencies received are:

$$f_d(r) = \frac{2v_0 f_0}{c}\left[1-\left(\frac{r}{R}\right)^{p_0}\right]\cos(\theta) \tag{6.10}$$

and the normalized power density spectrum is [4]:

$$G(f_d) = \begin{cases} \dfrac{2}{p_0 \cdot f_{\max}\left(1-\dfrac{f_d}{f_{\max}}\right)^{1-\frac{2}{p_0}}} \\ \\ f_{\max} = \dfrac{2v_0 f_0}{c}\cos(\theta) \end{cases} \tag{6..11}$$

The profiles given in (6.9) are for a stationary flow in a rigid tube. More complicated flow patterns are found in the human body since the flow is pulsatile and the vessels curve and branch (see Section 6.5). The power density spectrum however still corresponds to the velocity distribution, and ultrasound measurements can be used for revealing the velocity distribution over time.

An example for the carotid artery supplying the brain is shown in Fig. 6.5. The left part shows the anatomic gray scale image of the artery with the placement of the range gate. The right side shows the spectrogram, which gives the velocity distribution over time. The spectrogram is found from the Fourier transform of the measured sampled signal. Usually a new spectral estimate is calculated every 5 to 10 ms and the estimates are presented in a rolling display with the gray level corresponding to the number of scatterers with the particular velocity. The non-stationary nature of the distribution is clearly seen as is the periodicity with the heart cycle.

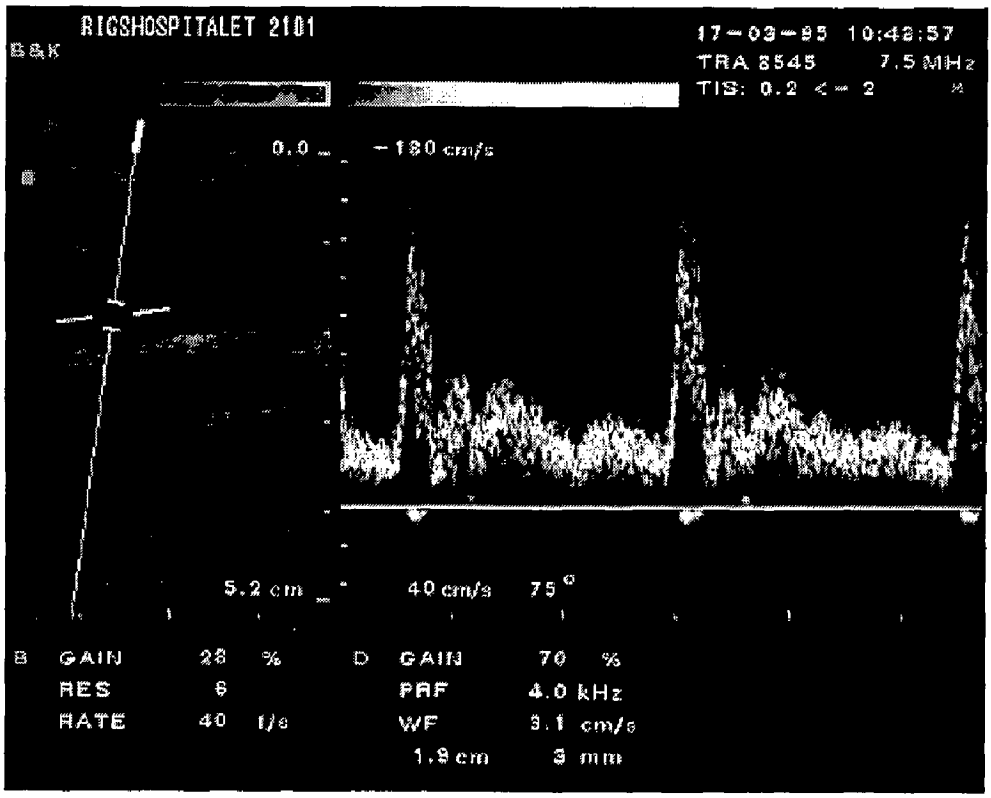

Fig. 6.5: Duplex scan showing both B-mode image and spectrogram of the carotid artery. The range gate is shown as the broken line in the gray-tone image. The square brackets indicate position and size of the range gate [4]

6.4 Making Images of Velocity

Images of velocity can also be made using ultrasound. This is done by acquiring 8 to 16 lines of data in one direction and then estimates the velocities along that direction. The

beam is then moved to another direction and the measurement is repeated. Doing this for all directions in an image gives a mapping of the velocity and that is displayed in color flow mapping (CFM) systems.

A system diagram for a CFM system is shown in Fig. 6.6. The RF signal from the transducer is demodulated to yield a complex signal, which is sampled by the ADC's at all the positions along the direction where the velocity must be found. The demodulation step also serves as a matched filter to suppress noise. The digital signal is then passed on to the filter for removing stationary signals. The delay line canceller (DLC) subtracts the samples from the previous line from the current line to remove the stationary signal. The tissue surrounding the vessels often generates a scattered signal that is 40 dB larger than the blood signals, and this will seriously deteriorate the velocity estimates. The tissue signal is, however, stationary and can therefore be removed by subtracting samples at the same depth in tissue for consecutive pulse-echo lines.

The sampled data for one direction is then divided into a number of segment, one for each pixel in the velocity image. Each segment holds 8 to 16 complex samples from which the velocity must be estimated. The mean velocity can be found from mean angular frequency determined by:

$$\bar{\omega} = \frac{\int_{-\infty}^{+\infty} \omega P(\omega) d\omega}{\int_{-\infty}^{+\infty} P(\omega) d\omega} \tag{6.12}$$

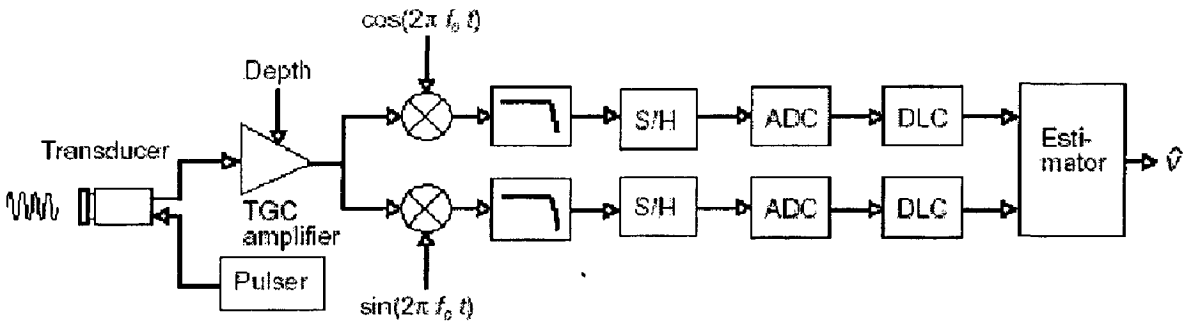

Fig. 6.6: Block diagram of color flow mapping system

$P(\omega)$ is the power density spectrum of the received, complex signal. The velocity is then given by:

$$v_z = \frac{\bar{\omega}}{4\pi f_0} c \tag{6.13}$$

The velocity can also be calculated from the phase shift between the pulse emissions. The complex digital signal can be written

$$r(i) = x(i) + jy(i) \tag{6.14}$$

where x is the real signal and y the imaginary signal. Using an autocorrelation estimator the velocity estimate is [42]

$$v_z = -\frac{c}{4\pi f_0 T_{prf}} \arctan\theta\left(\frac{\sum_{i=1}^{N-1} y(i)x(i-1) - x(i)y(i-1)}{\sum_{i=1}^{N-1} x(i)x(i-1) + y(i)y(i-1)}\right) \tag{6.15}$$

where N is the number of samples. This implementation is very efficient, since only few calculations are performed for each estimate, and this is the approach preferred in most scanners. The method is also robust in terms of noise, which is critical since the scattering from blood is quite weak compared to the surrounding tissue.

An example of a color flow image of the artery supplying the brain is shown in Fig. 6.7. Both positive and negative velocities can be seen. The jugular vein on the top has a blue color coding showing that the movement is towards the transducer, whereas the carotid artery below contains red colors for movement away from the transducer and to the brain.

6.4.1 Color Flow Mapping using Cross-Correlation

The estimation of velocity can also be done by finding the time-shift between two consecutive RF signals directly [43], [44], [45]. This is the approach taken in the cross-correlation system shown in Fig. 6.8.

The received RF signal is amplified and filtered with a matched filter to remove noise. An RF sampling at 20 to 30 MHz for a 5 MHz transducer is then performed and the removal of stationary signals is done by subtracting two consecutive RF lines.

The data is divided into segments as shown in Fig. 6.9. The velocity is found in each segment by cross-correlation with data from the previous pulse-echo line. The received signal can be written as:

$$r(t) = p(t) * s(t) \tag{6.16}$$

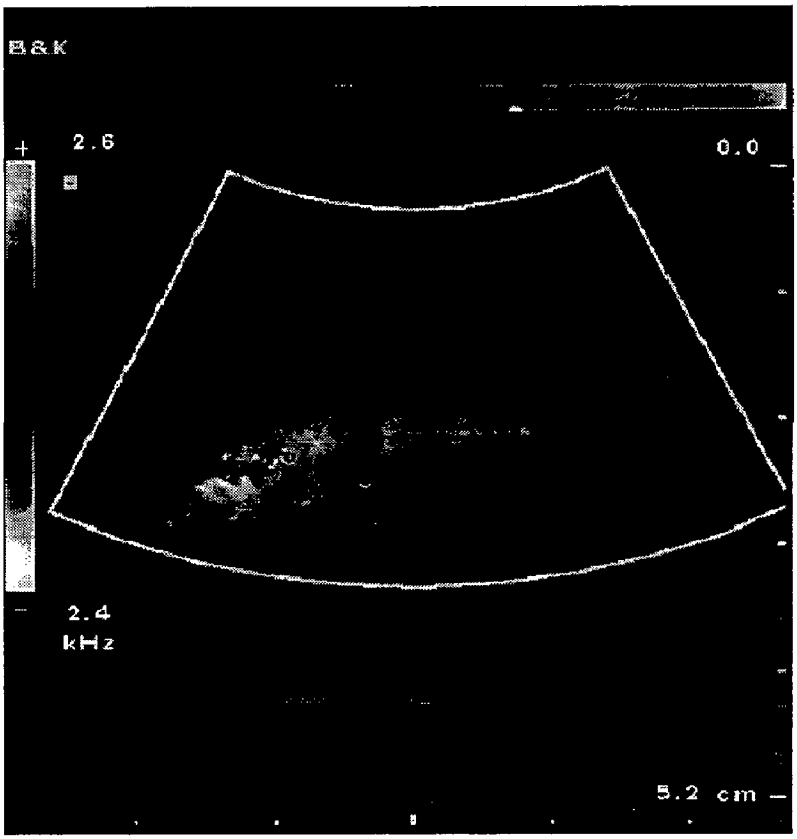

Fig. 6.7: Color flow mapping image of the carotid artery and jugular vein. Blue colors (top of the color bar) indicates velocities towards and red away from the transducer

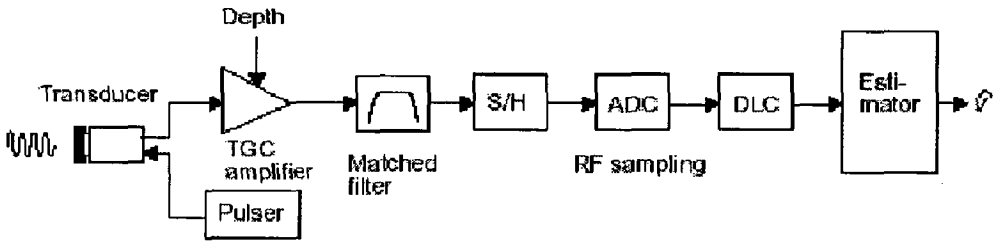

Fig. 6.8: System for cross-correlation flow estimation

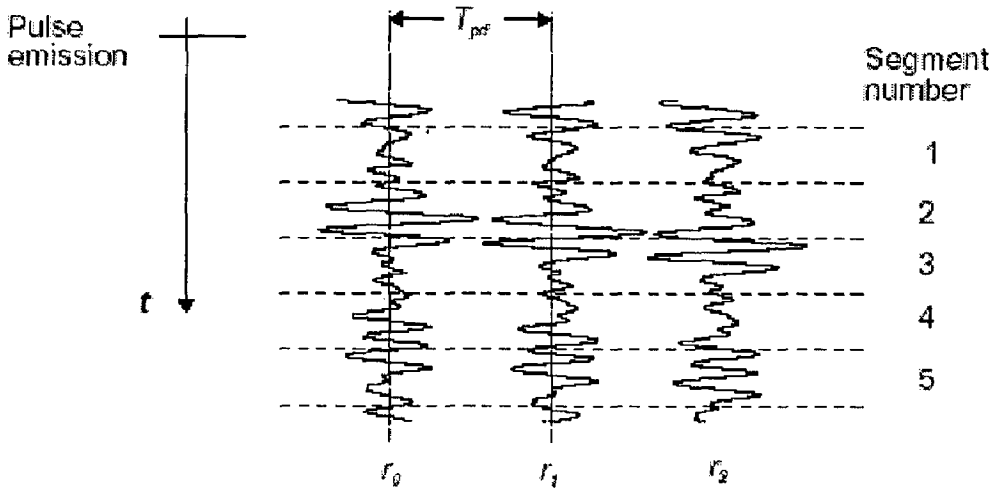

Fig. 6.9: Segmentation of RF data prior to cross-correlation

where $p(t)$ is the emitted pulse and $s(t)$ is the scattering signal from the blood. Cross-correlation two received signals then gives:

$$R_{12}(\tau) = E\{r_1(t)r_2(t+\tau)\} = E\{(p(t)*s(t))(p(t)*s(t-t_s+\tau))\}$$
$$= R_{pp}(\tau)*R_{ss}(\tau-t_s) \qquad (6.17)$$

where Rpp is the autocorrelation of the pulse and Rss is the autocorrelation of the blood scattering signal. s(t) can be assumed to be a white, Gaussian stochastic process, so that the cross-correlation can be written as:

$$R_{12}(\tau) = \sigma_s^2 R_{pp}(\tau-t_s) \qquad (6.18)$$

where s2s is the power of the blood signal. The autocorrelation of the pulse has a unique maximum at Rpp(0), and the time-shift can thus be found from the unique maximum in the cross-correlation function. The velocity is then given by:

$$v_z = \frac{c}{2}\frac{t_s}{T_{prf}} \tag{6.19}$$

The velocity estimates are then presented by the same method as mentioned for the autocorrelation approach.

The cross-correlation approach is optimized by sending out a narrow pulse, which also makes is easier to obtain a higher resolution in the color flow mapping images. The price is, however, that the peak intensities must be limited due to the safety limits imposed on the scanners. Therefore cross-correlation scanners can send out less energy and are often less sensitive than the scanners using the autocorrelation approach.

An other disadvantage of the cross-correlation approach is the large amount of calculations that must be performed per second. For a real time system it can approach one billion calculations per second making it necessary to use only the sign of the signals in the calculation of the cross-correlation [46].

6.5 Simulation of Flow Imaging Systems

The derivation given in this chapter generally assumes that the single scatterer stays within a region of uniform insonation. This is quite a crude assumption for realistic beams, as shown in Chapter 3. Both continuous and pulsed fields vary with position and this needs to be taken into account using the Tupholme–Stepanishen field model.
The received voltage trace was stated in Section 3.6.4 to be

$$p_r(\vec{r}_1,\vec{r}_2,t) = v_{pe}(t) *_t f_m h_{pe}(\vec{r}_1,\vec{r}_2,t) \tag{6.20}$$

where f_m accounts for the scattering by the medium, h_{pe} describes the spatial distribution of the ultrasound field, and v_{pe} is the one-dimensional pulse emanating from the pulse

excitation and conversion from voltage to pressure and back again. The model in Section 6.2 states that the scatterer will move during the interaction with the ultrasound giving rise to a Doppler shift. The most important feature is, however, the interpulse movement, because this is used by the pulsed scanners for detecting velocity. The approximation is then to include the small Doppler shift into the one-dimensional pulse v_{pe}, shifting its frequency content to f '= (1 +2v_z/c)f, and assuming that the field interacting with the scatterer stays constant. Usually the pulse duration is a few microseconds, so that the scatterers only move a fraction of a millimeter, even for high blood velocities, during the interaction, and the field can safely be assumed to be constant over this distance. The received voltage trace is then found directly from (6.20) with $\vec{r}_2$ indicating the position of the scatterers. Note that a spatial convolution takes place and that the received response is a summation of contributions from numerous scatterers. The scatterers move to the position

$$\vec{r}_2(i+1) = \vec{r}_2(i) + T_{prf}\vec{v}\left(\vec{r}_2(i), t\right) \tag{6.21}$$

when the next field from the subsequent pulse emission impinges on the scatterers. Here i denotes the pulse or line number and $\vec{v}\left(\vec{r}_2(i), t\right)$ is the velocity of the scatterer at the position indicated by $\vec{r}_2$(i) at time t. This assumes that the scatterers do not accelerate during the interaction. The movement between pulses, is $T_{prf}\vec{v}\left(\vec{r}_2(i), t\right)$ and the new position of the scatterers, $\vec{r}_2(i+1)$ can then be inserted in (6.20) and used for calculating the next voltage trace. The received signals for multiple pulse emissions can, thus, be found by these two equations. The actual calculation is rather complicated in three dimensions, but is easy to handle by a computer. The different velocities for the scatterers necessitate that separate Doppler shifts are included in v_{pe} for each scatterer. This can be done in a computer simulation of each scatterer before the contributions for all scatterers are summed, or a mean Doppler shift can be used. The effect of this Doppler shift is minor in pulsed systems and can, at least to a first approximation, be neglected. A fairly realistic simulation should, thus, be possible with this approach

6.7.1 Example of Flow Simulations

A Phantom is developed for evaluating color flow imaging. It generates data for flow in vessels with properties like the carotid artery, The velocity profile is close to parabolic, which is a fairly good approximation during most of the cardiac cycle [4] for a carotid artery. The phantom generates 10 files with positions of the scatterers at the corresponding time step. From file to file the scatterers are then propagated to the next position as a function of their velocity and the time between pulses. The ten files are then used for generating the RF lines for the different imaging directions and for ten different times. A linear scan of the phantom was made with a 192 element transducer using 64 active elements with a Hanning apodization in transmit and receive. The element height was 5 mm, the width was a wavelength and the kerf 0.05 mm. The pulses where the same as used for the point phantom mentioned Section 4.6. A single transmit focus was placed at 70 mm, and receive focusing was done at 20 mm intervals from 30 mm from the transducer surface. The resulting signals have then been used in a standard autocorrelation estimator [4] for finding the velocity image. The resulting color flow image is shown in Fig. 6.10. Note how the vessel is larger at the bottom than the top.

The simulation is made so multiple workstations can simultaneously work on the problem, as long as they have access to the same directory. This is done by looking at which RF files that have been generated. The first one not simulated is reserved by the program by writing a dummy file, and then doing the simulation. Multiple workstations can then work simultaneously on the problem and generate a result quickly.

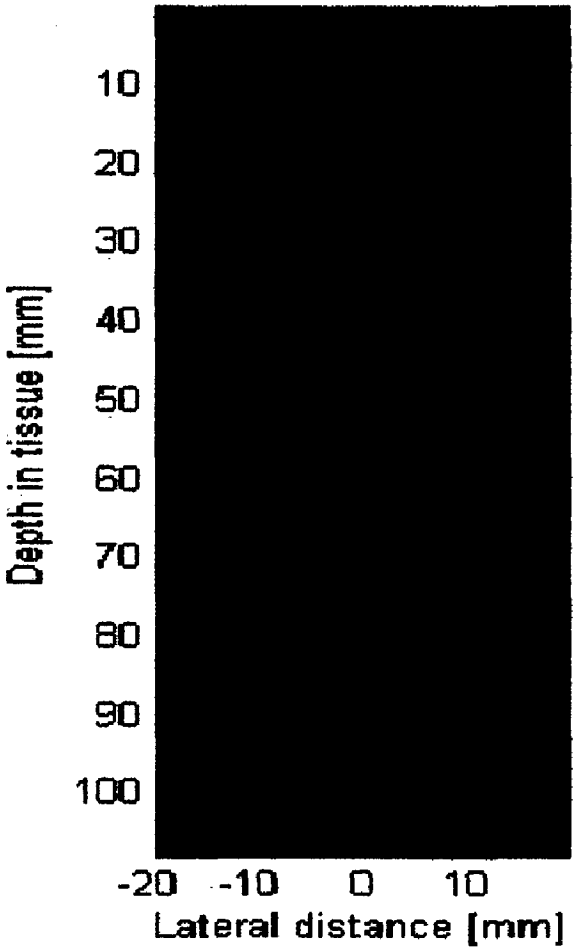

Fig. 6.10: Color flow image of vessel with a parabolic flow profile.

CHAPTER 7

CONCLUSIONS AND FUTURE SCOPE

7.1Conclusions

The simulation of ultrasound imaging using linear acoustics has been extensively used for studying focusing, image formation, and flow estimation, and it has become a standard tool in ultrasound research. The whole imaging process is simulated with time varying focusing and apodization. This has paved the way for doing realistic simulated imaging with multiple focal zones for transmission and reception and for using dynamic apodization. In this dissertation work, ultrasound imaging for different image types including flow images are simulated and some standard simulation phantoms are presented that can be used in designing and evaluating ultrasound transducers, beamformers and systems.

Artificial human phantoms of a fetus in the third month of development and an artificial kidney are shown. The simulation of flow and the associated phantoms is also discussed. All the phantoms can be used with any arbitrary transducer configuration like single element, linear, convex, or phased array transducers, with any apodization and focusing scheme.

This dissertation work presents a new fast simulation method based on the Field II program. In imaging the same spatial impulse response is calculated for each of the image lines, and making 128 lines, thus, gives 128 calculations of the same impulse response delayed differently for the different lines. Doing the focusing after this point in the simulation can make the calculation faster. This corresponds to full synthetic aperture imaging. The received response from each element is calculated, when emitting with each of the elements in the aperture, and then the responses are subsequently focused. The program simulates the signals received by all 128 transducer elements, and a matrix with signals results for each pulse-echo simulation. The separation of the received signal from

each of the virtual sources is done by applying a matched filter for each band on all the received signals. The result is the received signal on a specific element for one of the bands. The matched filter also equalizes the phase of the signals, so they all become zero phase signals. The signals are then focused by adding them for all elements, all bands and both emissions with a compensation for the travel time from the virtual source to the receiving element. The flow is simulated for a random collection of point scatterers in a tube with a laminar, parabolic flow. This is the approach taken in this dissertation work using a modified version of the Field II program.

The background for the doing ultrasound imaging simulation has been described along with advanced examples of its use. A fast program for the simulation of ultrasound imaging has been made. It can realistically simulate all kinds of ultrasound systems including color flow mapping. A full simulation can be performed in few hours on a Pentium PC, and fast prototyping is, thus, possible in software.

7.2 Future Scope

Many fruitful areas exist in ultrasonic imaging for further mathematical and physics research. The following is a list of areas of research that could produce a large impact on the field.

- Development of effective wideband models that include the physical acoustical properties of the tissues in which the beam is propagating, such as absorption and aberration-inducing effects. This is effectively the forward wave propagation problem.

- Development of 3Dand 4D finite-element models of single transducer elements and multi-element arrays.

- Development of super broadband transducers, array modeling, and effective modeling for multimode vibrations of transducer elements.

- Investigation of theories and development of faster beam-forming algorithms that will be flexible enough to allow adaptive corrections for phase and amplitude distortions attributable to both tissue and system effects.

- Development of algorithms that ensure that diagnostic information can be obtained from any one patient regardless of intervening tissue components.

Although the primary contemporary role of ultrasonic imaging is in diagnosis, the method also has important applications in monitoring the progression and regression of disease, in some areas of screening, and in interventional procedures, both for localization and for guidance. Ultrasonic imaging is likely to become one of the preferred visualization techniques in minimally invasive surgery, because of its high speed and ease of use. The safety record of ultrasonic imaging is impeccable. There is no reason to suppose that contemporary techniques employ levels of exposure that could cause biological damage, but it is prudent to be cautious and further research is justified.

The future of ultrasound in medicine depends upon talented people from medicine and the physical sciences working in close collaboration and upon the emergence of a new breed of research scientist trained in both medicine and engineering and dedicated not to the technology of destruction but rather to the preservation of life and humanity so that *"man will not merely endure; he will prevail."*

Refrences

[1] J. A. Jensen. A model for the propagation and scattering of ultrasound in tissue. J. Acoust. Soc. Am., 89:182– 191, 1991a.
[2] J. A. Jensen. A new calculation procedure for spatial impulse responses in ultrasound, J. Acoust. Soc. Am, 1999.
[3] J. A. Jensen, D. Gandhi, and W. D. O'Brien. Ultrasound fields in an attenuating medium. In Proc. IEEE Ultrason. Symp., pages 943–946, 1993.
[4] J. A. Jensen. Estimation of Blood Velocities Using Ultrasound: A Signal Processing Approach. Cambridge University Press, New York, 1996.
[5] A. D. Pierce. Acoustics, An Introduction to Physical Principles and Applications. Acoustical Society of America, New York, 1989.
[6] P. M. Morse and K. U. Ingard. Theoretical Acoustics. McGraw-Hill, New York, 1968.
[7] P. R. Stepanishen. Pulsed transmit/receive response of ultrasonic piezoelectric transducers. J. Acoust. Soc. Am., 69:1815–1827, 1981.
[8] L. E. Kinsler, A. R. Frey, A. B. Coppens, and J. V. Sanders. Fundamentals of Acoustics. John Wiley & Sons, New York, third edition, 1982.
[9] P. R. Stepanishen. Wide bandwidth near and far field transients from baffled pistons. In Proc. IEEE Ultrason. Symp., pages 113–118, 1977.
[10] L. Raade and B. Westergreen. b Mathematics handbook. Charwell-Bratt, Ltd., Kent, England, 1990.
[11] M. R. Spiegel. Mathematical handbook of formulas and tables. McGraw-Hill, New York, 1968.
[12] M. Arditi, F. S. Forster, and J. Hunt. Transient fields of concave annular arrays. Ultrason. Imaging, 3:37–61, 1981.
[13] A. Penttinen and M. Luukkala. The impulse response and nearfield of a curved ultrasonic radiator. J. Phys. D: Appl. Phys., 9:1547–1557, 1976.
[14] J. C. Lockwood and J. G. Willette. High-speed method for computing the exact solution for the pressure variations in the nearfield of a baffled piston. J. Acoust. Soc. Am., 53:735–741, 1973.
[15] J. L. S. Emeterio and L. G. Ullate. Diffraction impulse response of rectangular transducers. J. Acoust. Soc. Am., 92:651–662, 1992.
[16] J. A. Jensen. Ultrasound fields from triangular apertures. J. Acoust. Soc. Am., 100(4):2049–2056, 1996a.
[17] W. H. Press, B. P. Flannery, S. A. Teukolsky, and W. T. Vetterling. Numerical receipes in C. The art of scientific computing. Cambridge University Press, Cambridge, 1988.
[18] G. R. Harris. Transient field of a baffled planar piston having an arbitrary vibration amplitude distribution. J. Acoust. Soc. Am., 70:186–204, 1981.
[19] P. R. Stepanishen. Acoustic transients from planar axisymmetric vibrators using the impulse response ap-proach. J. Acoust. Soc. Am., 70:1176–1181, 1981.
[20] J. Naze Tjøtta and S. Tjøtta. Nearfield and farfield of pulsed acoustic radiators. J. Acoust. Soc. Am., 71:824– 834, 1982.

[21] Joon-Hyun Leo and Sang-Woo Choi: *A Parametric Study of Ultrasonic Beam Profiles for a Linear Phased Array Transducer*, IEEE TRANSACTIONS ON ULTRASONICS, FERROELECTRICS , AND FREQUENCY CONTROL, volume,. 47 no.3 MAY 2000
[22] J.C. Gore and S. Leeman. Ultrasonic backscattering from human tissue: A realistic model. Phys. Med. Biol., 22:317–326, 1977.
[23] M. Fatemi and A.C. Kak. Ultrasonic b-scan imaging: Theory of image formation and a technique for restora-tion. Ultrason. Imaging, 2:1–47, 1980.
[24] L.A. Chernov. Wave propagation in a random medium. Academic Press, 1960.
[25] P.E. Chandler S. Leeman, V.C. Roberts and L.A. Ferrari. Inverse imaging with strong multiple scattering. In M.A.Viergever and A. Todd-Pokropek, editors, Mathematics and computer science in medical imaging, pages 279–289. Springer-Verlag, 1988.
[26] G. E. Tupholme. Generation of acoustic pulses by baffled plane pistons. Mathematika, 16:209–224, 1969.
[27] P. R. Stepanishen. The time-dependent force and radiation impedance on a piston in a rigid infinite planar baffle. J. Acoust. Soc. Am., 49:841–849, 1971.
[28] P. M. Morse and K. U. Ingard. Methods of theoretical physics, part I. McGraw-Hill, New York, 1953.
[29] P. R. Stepanishen. Transient radiation from pistons in an infinte planar baffle. J. Acoust. Soc. Am., 49:1629– 1638, 1971.
[30] A. C. Kak and K. A. Dines. Signal processing of broadband pulse ultrasound: measurement of attenuation of soft biological tissues. IEEE Trans. Biomed. Eng., BME-25:321–344, 1978.
[31] K. V. Gurumurthy and R. M. Arthur. A dispersive model for the propagation of ultrasound in soft tissue. Ultrason. Imaging, 4:355–377, 1982.
[32] J. A. Jensen and P. Munk. Computer phantoms for simulating ultrasound b-mode and cfm images. In S. Lees and L. A. Ferrari, editors, Acoustical Imaging, volume 23, pages 75–80, 1997.
[33] J. A. Jensen. Field: A program for simulating ultrasound systems. Med. Biol. Eng. Comp., 10th Nordic-Baltic Conference on Biomedical Imaging, Vol. 4, Supplement 1, Part 1:351–353, 1996b.
[34] R. F. Wagner, S. W. Smith, J. M. Sandrick, and H. Lopez. Statistics of speckle in ultrasound B-scans. IEEE Trans. Son. Ultrason., 30:156–163, 1983.
[35] J. A. Jensen. Ultrasound systems for blood velocity estimation. In MMAR 98 Conference proceedings, pages 815–820, 1998.
[36] Shigeo Satomura. Ultrasonic Doppler method for the inspection of cardiac functions. J. Acoust. Soc. Am., 29:1181–1185, 1957.
[37] Shigeo Satomura. Study of the flow patterns in peripheral arteries by ultrasonics. J. Acoust. Soc. Jap., 15:151–158, 1959.
[38] D. W. Baker. Pulsed ultrasonic Doppler blood-flow sensing. IEEE Trans. Son. Ultrason., SU-17:170–185, 1970.
[39] Pierre A. Peronneau and Frenand Leger. Doppler ultrasonic pulsed blood flowmeter. In Proc. 8th Int. Conf. Med. Biol. Eng., pages 10–11, 1969.
[40] Peter N. T. Wells. A range gated ultrasonic Doppler system. Med. Biol. Eng., 7:641–652, 1969.

[41] K. Namekawa, C. Kasai, M. Tsukamoto, and A. Koyano. Realtime bloodflow imaging system utilizing autocorrelation techniques. In R.A Lerski and P. Morley, editors, Ultrasound '82, pages 203–208, New York, 1982. Pergamon Press.
[42] C. Kasai, K. Namekawa, A. Koyano, and R. Omoto. Real-time two-dimensional blood flow imaging using an autocorrelation technique. IEEE Trans. Son. Ultrason., 32:458–463, 1985.
[43] O. Bonnefous and P. Pesque´. Time domain formulation of pulse-Doppler ultrasound and blood velocity estimation by cross correlation. Ultrason. Imaging, 8:73–85, 1986.
[44] D. Dotti, E. Gatti, V. Svelto, A. Ugge`, and P. Vidali. Blood flow measurements by ultrasound correlation techniques. Energia Nucleare, 23:571–575, 1976.
[45] P. M. Embree and W. D. O'Brien. The accurate ultrasonic measurement of volume flow of blood by time-domain correlation. In Proc. IEEE Ultrason. Symp., pages 963–966, 1985.
[46] J. A. Jensen. Implementation of ultrasound time-domain cross-correlation blood velocity estimators. IEEE Trans. Biomed. Eng., 40:468–474, 1993a.
[47] W. W. Nichols and M. F. O'Rourke. McDonald's Blood Flow in Arteries, Theoretical, Experimental and Clinical Principles. Lea & Febiger, Philadelphia, 1990.
[48] J. R. Womersley. Oscillatory motion of a viscous liquid in a thin-walled elastic tube. I: The linear approxi-mation for long waves. Phil. Mag., 46:199–221, 1955.
[49] David H. Evans. Some aspects of the relationship between instantaneous volumetric blood flow and continu-ous wave Doppler ultrasound recordings III. Ultrasound Med. Biol., 9:617–623, 1982b.
[50] D. H. Evans, W. N. McDicken, R. Skidmore, and J. P. Woodcock. Doppler Ultrasound, Physics, Instrumen-tation, and Clinical Applications. John Wiley & Sons, New York, 1989.
[51] Ferride Severcan, Dana Dorohoi, Dorina Creanga. Ultrasound Propagation through Biological Tissues. Physica, Special Issue 2001.
[52] Pedersen, M. H., Vass, M., Ultrasound Scanning in General Practice, 2004.
[53] An Approach for Measuring Ultrasonic Backscattering from Biological Tissues with Focused Transducers Shyh-Hau Wang and K. Kirk Shung,* *Fellow, IEEE.*
IEEE TRANSACTIONS ON BIOMEDICAL ENGINEERING, VOL. 44, NO. 7, July 1997
[54] H. Ng, R. W. Prager, N. G. Kingsburj, G. M. Treece and A. H. Gee; Modelling Ultrasound Imaging as a linear, shift-variant system 21 January 2005. Department of Engineering, University of Cambridge.
[54] P.N.T.Wells, Current Status and future technical advances of ultrasound imaging, IEEE Eng. Med Biol. Mag. 2000; 19: 14-20.
[55] S. Bjaerum, D. Martens, K. Kristoffersen, and H. Torp,"Blood Motion Imaging - A New Technique to Visualize 2D Blood Flow", in *Proceedings of the IEEE Ultrasonics Symposium*, 2002.